

ABSTRACT

Title of dissertation: TOPOLOGICAL DISPERSION RELATIONS IN SPIN-ORBIT COUPLED BOSE GASES

Ana Valdés-Curiel,
Doctor of Philosophy, 2019

Dissertation directed by: Professor Ian Spielman
Joint Quantum Institute,
National Institute of Standards and Technology and
University of Maryland College Park

This thesis describes some of the work I did. It doesn't include work I didn't do. It mentions some of the work I had others do for me and finally some of the work others had me do for them.

TOPOLOGICAL DISPERSION RELATIONS IN
SPIN-ORBIT COUPLED BOSE GASES

by

Ana Valdés Curiel

Dissertation submitted to the Faculty of the Graduate School of the
University of Maryland, College Park in partial fulfillment
of the requirements for the degree of
Doctor of Philosophy
2019

Advisory Committee:

Professor Alicia Kollar, Chair

Professor Ian Spielman, Advisor

Professor Mohammad Hafezi, Dean's representative

Professor Trey Porto

Professor Norbert Linke

Professor Gretchen Campbell

© Copyright by
Ana Valdés Curiel
2019

Preface

Lapras

Foreword

Farfetch'd

*For my parents and in the
memory of Dr. Ernesto Valdés Krieg*

Acknowledgments

Charmander

Table of Contents

List of Tables	ix
List of Figures	x
List of Abbreviations	xiii
1 Introduction	1
1.1 Thesis overview	2
2 Basic theory of Bose-Einstein condensation	3
2.1 Bose-Einstein condensation of an ideal gas	4
2.1.1 Critical temperature	5
2.1.2 Condensate fraction	7
2.1.3 Bose gas in a harmonic trapping potential	8
2.2 Bose-Einstein condensation with atomic interactions	9
2.2.1 Gross-Pitaevskii equation	11
2.2.2 Multiple component BECs	13
2.2.3 Thomas-Fermi approximation	15
2.3 Density profiles	17
3 Manipulation and detection of ultra-cold atoms	21
3.1 Electronic structure of ^{87}Rb	21
3.2 Interaction between atoms and magnetic fields	24
3.2.1 Magnetic trapping	27
3.3 Interaction between atoms and electric fields	28
3.3.1 Scalar polarizability	31
3.3.1.1 Optical trapping	33
3.3.2 Vector polarizability and effective magnetic fields	34
3.3.2.1 Raman coupling	35
3.3.2.2 Spin-orbit coupling	38
3.4 Coherent manipulation	39
3.4.1 Rabi oscillations	40
3.4.2 Ramsey interferometer	42

3.4.3	Floquet theory	43
3.5	Detection: Resonant absorption imaging	46
3.5.1	High intensity absorption imaging	50
4	Making BECs in the Rubidium Lithium apparatus	53
4.1	Overview of the RbLi apparatus	54
4.1.1	Laser systems	55
4.1.2	Magnetic field control	56
4.2	Experimental sequence to make BECs	58
4.2.1	Adiabatic rapid passage	61
4.2.2	Magnetic field stabilization with microwave assisted partial transfer absorption imaging	63
4.3	Upgrades to the RbLi Machine	65
4.3.1	Master laser system	65
4.3.2	Raman laser system	66
4.3.3	High power RF system	68
4.3.4	6.8 GHz microwave system	71
4.4	Computer control and data acquisition	73
5	Fourier Transform Spectroscopy	77
5.1	Operating principle of Fourier spectroscopy	79
5.2	Measuring the SOC dispersion with Fourier transform spectroscopy	81
5.2.1	System	81
5.2.2	Tunable SOC	83
5.2.3	Application of Fourier spectroscopy	86
5.2.4	Effective mass	87
5.2.5	Measured dispersion	90
6	Synthetic clock transitions through continuous dynamical decoupling	97
6.1	Basic principles of CDD	98
6.2	CDD of a spin-1 system	99
6.3	The $ xyz\rangle$ states	100
6.3.1	State decomposition	100
6.3.2	Energies	102
6.3.3	Transition matrix elements	103
6.4	$ xyz\rangle$ state preparation	105
6.5	Initial characterization of Ω	106
6.6	Spectroscopy	108
6.7	Robustness	109
6.7.1	Optimal response to noise	111
6.8	Driving dressed state transitions	112
6.9	Concatenated CDD	115
6.10	Conclusions	118

7	Topological order in quantum systems	121
7.1	Topology in mathematics	122
7.2	Topological order in condensed matter	124
7.3	Berry phase and Berry curvature	126
7.3.1	Aharonov-Bohm phase as an example of a Berry's phase	129
7.3.2	Chern number	130
7.4	The bulk-edge correspondence principle	132
7.5	Example: two-level model	133
7.6	Monopoles and Dirac strings	134
7.7	Conclusions	136
8	Unconventional topology with a Rashba SOC quantum gas	138
8.1	Rashba spin-orbit coupling	139
8.2	Rashba SOC for neutral atoms	141
8.3	Experimental implementation of Rashba SOC	144
8.3.1	Raman coupling the $ xyz\rangle$ states	146
8.3.1.1	Floquet and off resonant coupling effects	148
8.3.1.2	Lifetime	149
8.3.2	Measuring quasimomentum distributions	150
8.3.2.1	Correcting shears from Stern-Gerlach gradient	152
8.4	Fourier spectroscopy of the Rashba dispersion	154
8.5	Quantum state tomography with Ramsey interferometer	156
8.5.1	Wave function evolution in Ramsey interferometer	159
8.5.2	Combining phases from different measurements	163
8.5.3	Measuring the topological index	164
8.6	Conclusion	166
9	Conclusions and outlook	168
9	Realization of a fractional period adiabatic superlattice	169
A	RbLi: the good, the bad and the ugly	170
B	New apparatus	171
B.1	Water cooling stuff	171
B.2	Electrical installation	171
B.3	New Rb ‘oven’	171
C	Full derivation of the Raman coupled $ xyz\rangle$ states	172
C.0.0.1	Going into rotating frame	176
	Bibliography	182

List of Tables

4.1	List of AOM driver components	68
4.2	6.8 GHz microwave system components	72
6.1	Summary of CDD energies	116

List of Figures

1	The Bose-Einstein distribution	5
2	The Thomas-Fermi density distribution	16
3	Momentum distribution of atoms near T_c	20
1	^{87}Rb level structure	22
2	Zeeman splitting of the $5^2S_{1/2}$ manifold of ^{87}Rb	26
3	Raman coupling with two-photon transitions	36
4	Electric realizabilities and scattering rates as a function of wavelength	37
5	The Rabi cycle	41
6	A Ramsey interferometer	43
7	Magnetic phases of a spin-1 SOC system	47
8	The Beer-Lambert law	49
9	Resonant absorption imaging	50
10	High intensity absorption image	51
1	The RbLi vacuum system	54
2	Laser cooling frequencies	57
3	Diagram of the RbLi apparatus	58
4	Magnetic coil geometry in the RbLi apparatus	59
5	Adiabatic rapid passage	63
6	Magnetic field stabilization using microwave assisted PTAI	64
7	Master laser system	66
8	Ti:Sapphire laser output as a function of pump power	67
9	Optical layout of Raman and optical lattice lasers	69
10	AOM driving electronics	70
11	High power RF system	71
12	Impedance matching of high power RF antenna	72
13	74
14	76
1	Operating principle of Fourier spectroscopy	79
2	Experimental setup for engineering a tunable system with equal contributions of Rashba and Dresselhaus-type spin-orbit coupling	82

3	Floquet quasi-energy spectrum of a three-level system with spin-orbit coupling and periodic coupling strength	84
4	Dipole oscillations of a spin-orbit coupled BEC in a dipole trap	89
5	Time evolution and Fourier transforms of a SOC system	93
6	Power spectral density of the time dependent occupation probability for each state in the measurement basis for three coupling regimes	94
7	Spin-dependent SOC dispersion for three different coupling regimes	95
8	Converting energy differences into absolute energies	96
1	Implementing CCD.	100
2	State decomposition of the $ xyz\rangle$ states	101
3	Experimental CCD protocol	106
4	Calibration of Ω	107
5	Spectroscopy of the $ xyz\rangle$ states	109
6	The $ z\rangle \rightarrow x\rangle$ transition as a function of Ω_{RF}	110
7	Optimal response of the zx transition	112
8	Coherent driving of dressed state transitions	113
9	Loss of contrast of coherent oscillations	114
10	Concatenated CDD protocol	117
11	Concatenated CCD	120
1	The quantum Hall effect	125
2	The Aharonov-Bohm experiment	129
3	Graphical representation of Chern number	134
4	Graphical representation of Chern number	135
5	Different topological invariants	137
1	Rashba dispersion relation	140
2	The Rashba ring coupling	142
3	Rashba ring coupling eigenenergies	143
4	Rashba ring coupling ground state dispersion	145
5	Experimental setup for implementing Rashba spin-orbit coupling	146
6	Effect of neighboring Floquet manifolds on Rashba dispersion	149
7	Lifetime of Raman dressed states	150
8	Mapping momentum into quasimomentum	152
9	Correcting shears in momentum distribution from magnetic field gradients	153
10	Fourier spectroscopy of a Rashba SOC syste: Experimental protocol and representative data	155
11	Sample power spectral densities for all states used in the measurement of the Fourier spectrum	157
12	Predicted dispersion relation and Fourier spectrum	158
13	Experimental protocol for three-arm Ramsey interferometer (not to scale)	159
14	Dragging the Dirac point through the atoms	161

15	Representative data of the probabilities measured after the three output ports of Ramsey interferometer	163
16	Weight arrays used for combination of interferometer phases	164
17	Topological invariants obtained from quantum state tomography	165
1	Laser layout: We use a strong RF field and three linearly polarized Raman beams propagating in the xy plane couple the $ xyz\rangle$ states and engineer the Rashba Hamiltonian.	180
2	Laser frequencies: We have two frequency choices that allow us to address the three transitions between the $ xyz\rangle$ states. a) The blue detuned case. There are 2 frequencies smaller by about ω_{RF} and one larger frequency. b) The red detuned case. There are 2 frequencies that are larger by about ω_{RF} and one smaller frequency. Nice!	180
3	a Probabilities as a function of quasimomentum for the three output ports of the interferometer at $t_{\text{free}} = 160 \mu\text{s}$ b Probabilities as a function of free evolution time t_{free} for an input state with quasimomentum $(q_1, q_2) = (0.55, -0.92) k_L$ indicated by the blue star on a and in the topological ground branch ($n = 1$)	181
4	a Probabilities as a function of quasimomentum for the three output ports of the interferometer at $t_{\text{free}} = 160 \mu\text{s}$ b Probabilities as a function of free evolution time t_{free} for an input state with quasimomentum $(q_1, q_2) = (0.55, -0.92) k_L$ indicated by the blue star on a and in the topological ground branch ($n = 1$)	181

List of Abbreviations

Abbreviation	Full meaning
BEC	Bose-Einstein condensate
SOC	spin-orbit coupling
CDD	continuous dynamical decoupling
TOF	time of flight
OD	optical depth
TF	Thomas-Fermi
MOT	magneto optical trap
RF	radio frequency
ARP	adiabatic rapid passage
RWA	rotating wave approximation
PTAI	partial transfer absorption imaging
PSD	power spectral density
TTL	transistor-transistor logic
CCD	charge-coupled device
AOM	acousto-optic modulator
SG	Stern-Gerlach
DDS	direct digital synthesizer
1D	one-dimensional
2D	two-dimensional
3D	three-dimensional
DC	direct current
VNA	vector network analyzer
NIST	National Institute of Standards and Technology
JQI	Joint Quantum Institute

Chapter 1: Introduction

Why is quantum simulation important:

- Can help understand problems that are not easy to solve numerically or analytically. High temperature superconductors, frustrated systems, as good examples.
- Create analogues to systems that would otherwise not be possible to study.

Example: the expanding universe, Hofstadter at large magnetic fields.

- Create new exotic systems that do not exist in nature but can help us learn or understand something... or are just fun!

Don't forget to talk about topology! It starts with condensed matter but has been relevant to many other systems. Many Nobel prizes awarded, many applications and potential applications found.

Start with topology and move into quantum simulation? Or the other way around?

1.1 Thesis overview

In Chapters 2 and 3 I will describe the basic theory of Bose-Einstein condensation and the technical details of our experimental apparatus that produces ^{87}Rb BECs. In Chapter 4 I will describe our quantum simulation toolkit, the standard techniques that we use to manipulate and detect ensembles of ultracold atoms that are necessary for all of our experiments. Chapter 5 describes a Fourier transform spectroscopy technique that exploits the relation between quantum coherent evolution and the underlying spectrum of a system and that was used to characterize experiments described later in the thesis. Chapter 6 describes an implementation of continuous dynamical decoupling that helped to both make our system more robust against environmental noise and also allowed us to couple the internal states of the atoms in new ways that were not possible before, opening the path for new kinds of quantum simulations described in Chapters 7 and 8. In Chapter 8 I describe the experimental realization of Rashba spin-orbit coupling for a quantum system without a crystalline structure and has unconventional topology characterized by non-integer topological invariants. Finally, Chapter 8 describes the experimental implementation of a fractional period adiabatic superlattice, an intermediate step necessary for us to generate Hofstadter cylinders with non-zero magnetic flux in the future.

Appendix are experiments that I contributed to but are not included in the thesis. Also things related to new apparatus?

Chapter 2: Basic theory of Bose-Einstein condensation

Bose-Einstein condensation (BEC) is a quantum state of matter in which particles with integer valued spin all tend to occupy or ‘condense’ into the ground state. In dilute gases, condensation occurs when the temperature of the system goes below a critical temperature where the bosons become indistinguishable particles and quantum statistics become relevant.

BECs enable the observation of macroscopic quantum phenomena and there have been a number of fascinating experiments studying the properties of this systems, from measuring interference fringes of a macroscopic wave function to studying collective effects such as the propagation of sound [1], as well as extensive theoretical developments [2]. In our experiments however BECs are not the primary object of study, instead they are used as a platform enabling the simulation of analogue physical systems.

In this Chapter I give an overview of Bose-Einstein condensation in dilute atomic gases and I describe the properties most relevant to our experiments. I start by describing the case of an ideal gas and then consider the effects of interactions and trapping potentials as are present in our case. A reader interested in learning about this subject in more depth is advised to read [3] and [4].

2.1 Bose-Einstein condensation of an ideal gas

At low temperatures and in thermodynamic equilibrium, the mean occupation number of non-interacting identical bosons in the state with energy E is given by the Bose-Einstein distribution

$$n(E_j) = \frac{1}{e^{(E_j - \mu)/k_B T} - 1} \quad (2.1)$$

where T is the temperature, μ is the chemical potential (the energy cost of adding or removing a particle) and k_B is the Boltzmann constant. In the limit of large temperatures the Bose distribution can be approximated by the Maxwell-Boltzmann distribution

$$n(E_j) \approx e^{-(E_j - \mu)/kT} \quad (2.2)$$

which applies to classical, distinguishable particles. The chemical potential is determined by the condition that the total number of particles N is equal to the sum over all states in the distribution $N = \sum_j n(E_j)$ and is therefore a function of N and T . Additionally, in order for $n(E_j)$ to be positive definite we must have $\mu \leq E_0$ where E_0 is the energy of the ground state. From the Bose distribution we can see that the occupation number of the ground state is unbounded when $\mu \rightarrow 0$ as is shown in Figure 2.1. The number of particles occupying the excited states is bounded and when that number is reached, the remaining particles can occupy the ground state and thus Bose-Einstein condensation occurs.

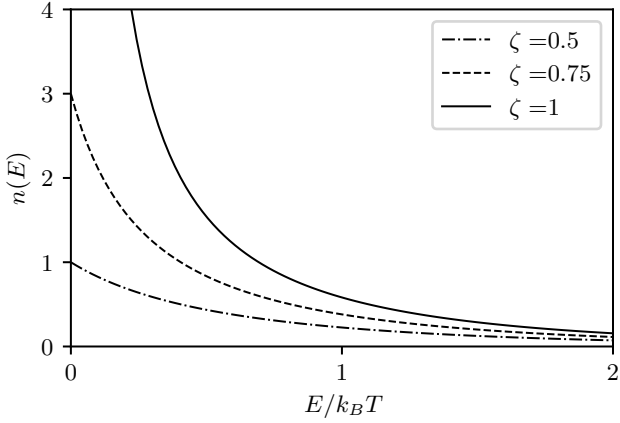


Figure 1: The Bose-Einstein distribution. Occupation number as a function of energy for different values of fugacity $\zeta = \exp(\mu/k_B T)$. Condensation occurs when $\mu = 0$ ($\zeta = 1$) and the occupation number in the ground state diverges.

2.1.1 Critical temperature

Bose-Einstein condensation can be understood in terms of the de Broglie waves associated to particles. The thermal de Broglie wavelength is defined as

$$\lambda_{\text{th}} = \left(\frac{2\pi\hbar^2}{mk_B T} \right)^{1/2} \quad (2.3)$$

and it characterized the spatial extension of the wave packet an individual particle at temperature T . Condensation occurs when λ_{th} becomes comparable with the inter-particle separation $n^{-1/3}$, where $n = N/V$. The quantity $n\lambda_{\text{th}}^3$ is known as the phase space density which describes the number of particles contained in a box with volume λ_{th}^3 .

An analytical expression for the critical temperature at which atoms condense can be derived using the Bose-Einstein distribution. For closely spaced energy lev-

els (compared to $k_B T$) the sum representing the total number of particles can be replaced by the integral

$$N = \int_0^\infty n(E)g(E)dE \quad (2.4)$$

where $g(E)$ is the density of states and $g(E)dE$ corresponds to the number of available states with energy between E and $E+dE$. For a free particle in three dimensions the density of states is

$$g(E) = \frac{Vm^{3/2}}{\sqrt{2\pi^2\hbar^2}} E^{1/2}, \quad (2.5)$$

and in general the density of states can be expressed as a power of energy $g(E) = C_\alpha E^{\alpha-1}$.

The integral in Equation 2.4 is not analytically solvable, however we can make the simplifying assumption $\mu = 0$. The critical temperature T_c is determined by the condition that all particles are in the excited states

$$\begin{aligned} N &= N_{\text{ex}}(T_c, \mu = 0) \\ &= \int_0^\infty \frac{g(E)dE}{e^{E/k_B T_c} - 1} \\ &= C_\alpha (k_B T_c)^\alpha \int_0^\infty \frac{x^{\alpha-1}}{e^x - 1} \\ &= c_\alpha (k_B T_c)^\alpha \Gamma(\alpha) \zeta(\alpha) \end{aligned} \quad (2.6)$$

where I made the substitution $x = E/k_B T_c$, $\Gamma(\alpha) = \int_0^\infty x^{\alpha-1} e^{-x} dx$ is the Gamma function and $\zeta(\alpha) = \sum_{n=1}^\infty n^{-\alpha}$ is the Riemann zeta function. From Equation 2.6 we

find that the critical temperature for Bose-Einstein condensation is

$$k_B T_c = \left(\frac{N}{C_\alpha \Gamma(\alpha) \zeta(\alpha)} \right)^{1/\alpha}. \quad (2.7)$$

If we compute the phase space density for free particles in 3D with density of states given by Equation 2.5 in combination with the expression for the critical temperature (Equation 2.6) we find that indeed when $T = T_c$

$$n\lambda_{\text{th}}^3 = \zeta\left(\frac{3}{2}\right) \approx 2.612, \quad (2.8)$$

the inter particle spacing and the thermal wavelength are comparable. In order to experimentally produce BECs, a combination of laser and evaporative cooling techniques are deployed such that we can increase the density while minimizing the temperature and therefore maximize the phase space density. The densities for BECs of Alkali atoms typically range in of order 10^{13} to 10^{15} atoms/cm⁻³.

2.1.2 Condensate fraction

Now we look at the fraction of particles occupying the ground state at temperatures below T_c . The total number of particles is given by $N = N_0 + N_{\text{ex}}$. The number of particles in the excited state will be given by the integral in Equation 2.4. For $g(E) = C_\alpha E^{\alpha-1}$ and $\alpha > 0$ the integral converges, we can then evaluate the integral

in Equation 2.6 for $T < T_c$ and get

$$\begin{aligned} N_{\text{ex}} &= c_\alpha (k_B T)^\alpha \Gamma(\alpha) \zeta(\alpha) \\ &= N \left(\frac{T}{T_c} \right)^\alpha, \end{aligned} \quad (2.9)$$

where I used the fact that when $T = T_c$ the total number $N = N_{\text{ex}}$. The number of particles in the ground state is therefore

$$\begin{aligned} N_0 &= N - N_{\text{ex}} \\ &= N \left[1 - \left(\frac{T}{T_c} \right)^\alpha \right] \end{aligned} \quad (2.10)$$

2.1.3 Bose gas in a harmonic trapping potential

I consider the particular case of particles confined in a three dimensional harmonic potential

$$V(\mathbf{r}) = \frac{m}{2} (\omega_x^2 x^2 + \omega_y^2 y^2 + \omega_z^2 z^2) \quad (2.11)$$

as it is the most relevant to our experiments that are performed in optical dipole traps that can be described as harmonic potentials. The density of states for is

$$g(E) = \frac{E^2}{2\hbar^2 \omega_x \omega_y \omega_z}, \quad (2.12)$$

which corresponds to $\alpha = 3$ and $C_3 = (2\hbar^3\omega_x\omega_y\omega_z)^{-1}$. Using Equation 2.6, we find that the transition temperature is

$$k_B T_c = \frac{\hbar\bar{\omega}N^{1/3}}{\zeta(3)^{1/3}} \approx 0.94\hbar\bar{\omega}N^{1/3} \quad (2.13)$$

where $\bar{\omega} = (\omega_x\omega_y\omega_z)^{1/3}$ is the geometric mean of the oscillation frequencies. Similarly we find that the condensed fraction is

$$N_0 = N \left[1 - \left(\frac{T}{T_c} \right)^3 \right] \quad (2.14)$$

Condensates in harmonic traps have some striking features that will be further explored in more detail in the following sections. The confining potential makes the BECs both finite sized and inhomogeneous which means that the BEC can be observed both in momentum space and in coordinate space. Another consequence of the inhomogeneity of these systems is the role of two-body interactions, which gets enhanced and leads to noticeable effects in measurable quantities [2, 5] such as interaction driven expansion when they are released from the confining potential. Some of these features will be discussed in more detail in the following sections.

2.2 Bose-Einstein condensation with atomic interactions

Even though atomic BECs are made from very dilute gases, the system is far from being an ideal gas and interactions need to be taken into account for a complete treatment.

The collisional properties of particles at low energies, such as cold atoms in a condensate, are dominated by *s*-wave scattering which can be described in terms of a single parameter the scattering length a that determines both the scattering cross section $\sigma = 4\pi a^2$ and the phase shift of the scattered wave function.

The magnitude of the scattering length is determined by the interatomic interaction potentials. For Alkali atoms at large distances, the two-body interactions are dominated by an attractive Van der walls interaction $U(r) = -C_6/r^6$ that arises from dipole-dipole interactions. At smaller distances the attractive potential is replaced by a strong repulsive electron-exchange interaction $U(r) \rightarrow \infty$. This minimal model captures the most important properties of the inter-atomic potential and can be solved analytically [6].

If the range of the interaction is much shorter than the mean inter-atomic distance the interaction can be approximated by an effective pseudo-potential $U_{\text{eff}}(\mathbf{r} - \mathbf{r}')$ such that

$$a = \frac{m}{4\pi\hbar^2} \int U_{\text{eff}}(\mathbf{r} - \mathbf{r}') d\mathbf{r} \quad (2.15)$$

which determines

$$U_{\text{eff}}(\mathbf{r} - \mathbf{r}') = \frac{4\pi\hbar^2 a}{m} \delta(\mathbf{r} - \mathbf{r}') = g\delta(\mathbf{r} - \mathbf{r}'). \quad (2.16)$$

This is a nice approximation as it allows us to model the scattering between atoms as a hard sphere scattering process instead of considering the more complicated inter-atomic potentials. The sign of the scattering length determines the attractive or

repulsive nature of the interactions and it plays an important role in the experimental production of BECs as it determines the rate at which atoms thermalize during evaporative cooling.

2.2.1 Gross-Pitaevskii equation

The full Hamiltonian describing N identical bosons with contact interactions can be written as

$$\hat{H} = \sum_{i=1}^N \left[\frac{\mathbf{p}_i^2}{2m} + V(\mathbf{r}_i) \right] + g \sum_{i < j} \delta(\mathbf{r}_i - \mathbf{r}_j), \quad (2.17)$$

where $V(\mathbf{r})$ is an external potential and $\mathbf{p}_i = -i\hbar\nabla_i$ is the momentum. We now consider a normalized eigenstate of the Hamiltonian $\Psi(\mathbf{r}_1, \mathbf{r}_2, \dots, \mathbf{r}_N)$ that satisfies the Schrödinger equation. We can simplify this state by taking a mean field approach; we assume that the system has undergone condensation so that the majority of the particles share the same single particle ground state $\phi(\mathbf{r})$ the wavefunction can be approximated by a symmetrized product

$$\Psi(\mathbf{r}_1, \mathbf{r}_2, \dots, \mathbf{r}_N) = \prod_{i=1}^N \phi(\mathbf{r}_i), \quad (2.18)$$

where ϕ is normalized to unity. The energy of the state from Equation 2.18 is given by the expectation value

$$\begin{aligned} E &= \int \Psi^* \hat{H} \Psi d\mathbf{r} \\ &= N \int \phi^*(\mathbf{r}) \left[-\frac{\hbar^2}{2m} \nabla^2 + V(\mathbf{r}) + \frac{(N-1)}{2} g |\phi(\mathbf{r})|^2 \right] \phi(\mathbf{r}) d\mathbf{r}, \end{aligned} \quad (2.19)$$

where $N(N-1)/2 \approx N^2/2$ counts the number of terms in the interaction energy.

Now we introduce the wave function of the condensate $\psi(\mathbf{r}) = N^{1/2} \phi(\mathbf{r})$, which when inserted in Equation 2.19 makes the N factors cancel out. The optimal form of ψ should minimize the energy subject to the normalization condition $N = \int |\psi(\mathbf{r})|^2 d\mathbf{r}$. This can be done by introducing a Lagrange multiplier μ so that

$$\frac{\delta}{\delta \psi^*(\mathbf{r})} \left(E - \mu \int |\psi|^2 d\mathbf{r} \right) = \left[-\frac{\hbar^2}{2m} \nabla^2 + V(\mathbf{r}) + g |\psi(\mathbf{r})|^2 - \mu \right] \psi(\mathbf{r}) = 0, \quad (2.20)$$

and we thus find that the condensate wave function obeys a non-linear Schrödinger equation known as the Gross-Pitaevskii (GP) equation.

$$\left[-\frac{\hbar^2}{2m} \nabla^2 + V(\mathbf{r}) + g |\psi(\mathbf{r})|^2 \right] \psi(\mathbf{r}) = \mu \psi(\mathbf{r}) \quad (2.21)$$

where μ plays the role of the chemical potential. The dynamics of the condensate will similarly be described by the time-dependent GP equation

$$i\hbar \frac{\partial}{\partial t} \psi(\mathbf{r}, t) = \left[-\frac{\hbar^2}{2m} + V(\mathbf{r}) + g |\psi(\mathbf{r}, t)|^2 \right] \psi(\mathbf{r}, t) \quad (2.22)$$

The GP equation is useful for describing the relevant phenomena associated with BECs, for example the propagation of collective excitations and the expansion of the condensate when released from a trap. The crucial assumption when deriving these equations was the mean field approximation which should be valid for dilute BECs in which the condensate fraction is close to unity. The excitations of the system can be described by a set of equations similar to those of classical hydrodynamics derived from the GP equation or alternatively using Bogoliubov theory for weakly interacting bosons [3].

2.2.2 Multiple component BECs

So far the discussion has been limited to single component BECs but most of our experiments are performed using a combination of multiple atomic internal states. In general, for a multiple component condensate the scattering lengths characterizing the interactions depend on the internal states of the incoming and outgoing scattering channels. Two spin- f^1 particles colliding particles will be characterized by $2f$ scattering lengths a_F . For bosons the total spin F takes even values and in particular for ^{87}Rb atoms in the $f = 1$ hyperfine ground state there are two scattering lengths a_0 and a_2 corresponding to the two-particle total angular momentum states of $F = 0$ and $F = 2$ respectively. The values of scattering lengths are $a_0 = 101.8a_0$ and $a_2 = 100.4a_0$ [7] where $a_0 = 5.29 \times 10^{-11}$ is the Bohr radius. From

¹Here I use the symbol f to denote the angular momentum of the individual particles and F to denote the total angular momentum of the two particles.

the scattering lengths we can calculate two interaction coefficients

$$\begin{aligned} c_0 &= \frac{4\pi\hbar^2}{m} \frac{a_0 + 2a_2}{3} = 100.84a_0 \frac{4\pi\hbar^2}{m} \\ c_2 &= \frac{4\pi\hbar^2}{m} \frac{a_0 - a_2}{3} \approx -4.7 \times 10^{-3}c_0. \end{aligned} \quad (2.23)$$

Here c_0 represents a spin-independent interaction strength that depends only on the total density while c_2 is a spin-dependent energy that is relevant only where there is non-zero density of both atoms in $m_F = \pm 1$ and is much smaller than the spin-independent energy. Similar to the case of single component BECs, the dynamics of multiple component BECs is governed by a spinor GP equation (see [3, 7]). The spin-dependent interaction strength gives rise to processes like coherent spin-mixing oscillations and domain formation and coarsening which was previously studied in the our lab [8].

The time scale at which interactions become relevant is set by the interaction energies $n|c_i|$. The most noticeable effect of interactions in our system is the density profile of the condensate and its anisotropic expansion after it is released from a trap which I will describe in the following sections. For the typical densities and timescales of our experiments as well as the relatively high magnetic fields that we operate at, we do not observe noticeable effects from interactions in the dynamics of the system and in the remaining chapters I will describe the dynamics of the BEC using single particle physics (i.e. the regular time-dependent Schrödinger equation).

2.2.3 Thomas-Fermi approximation

For systems with large N , the interaction term in the GP equation is very large compared to the kinetic energy². As the kinetic energy becomes less important we enter the Thomas-Fermi (TF) regime where the energy of the system is given only by the external potential and the mean field energy and the GP equation is considerably simplified

$$[V(\mathbf{r}) + g|\psi(\mathbf{r})|\psi(\mathbf{r})|^2] \psi(\mathbf{r}) = \mu\psi(\mathbf{r}). \quad (2.24)$$

In the TF regime the density distribution of the condensate $n(\mathbf{r}) = |\psi(\mathbf{r})|^2$ reflects the shape of the external potential

$$n(\mathbf{r}) = g^{-1}[\mu - V(\mathbf{r})], \quad (2.25)$$

when $\mu - V(\mathbf{r}) > 0$ and is otherwise zero. For a harmonic confining potential (Equation 2.11) as is typical in our experiments we find that the length scale that characterizes the size of the condensate is the Thomas-Fermi radius

$$R_j = \sqrt{\frac{2\mu}{m\omega_j^2}}, \quad j = x, y, z. \quad (2.26)$$

The density of the condensate is described by an inverted parabola

$$n(\mathbf{r}) = \frac{\mu}{g} \left(1 - \frac{x^2}{R_x^2} - \frac{y^2}{R_y^2} - \frac{z^2}{R_z^2} \right). \quad (2.27)$$

²It can be shown that the ratio of kinetic energy to interactions scales like $N^{-4/5}$

as is shown in Figure 2a. By integrating over Equation 2.27 we find that

$$N = \frac{8\pi}{15} \frac{\mu}{g} R_x R_y R_z, \quad (2.28)$$

which allows to determine the number of atoms in the condensate based on the density profile. In practice, in-situ BECs are very dense which can lead to some technical difficulties when trying to image directly their density profiles (see Section 3.5) so instead our images are taken after the atoms are released from the trap and allowed to expand for some time. In the next section I will discuss how the density profiles of atomic clouds are modified after they are released from a confining potential.

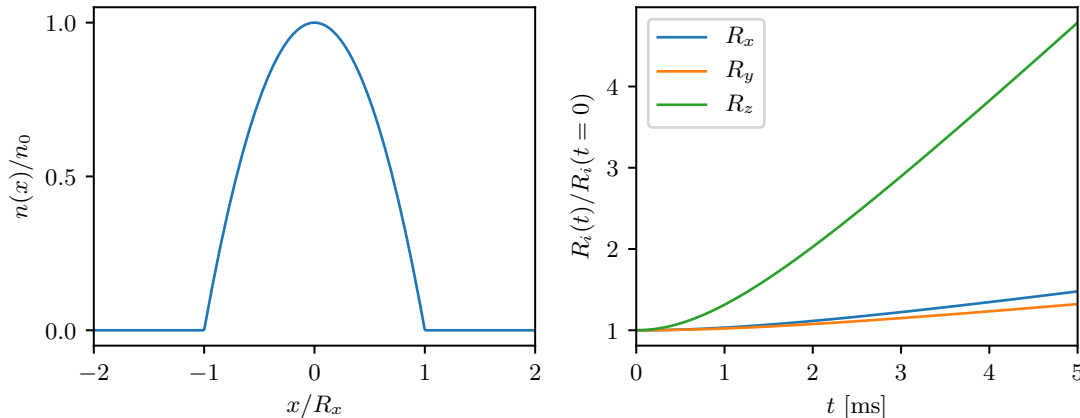


Figure 2: In the Thomas-Fermi regime where interactions are large compared to kinetic energy the density profile is determined by the external potential. **a.** Density profile along \mathbf{e}_x of a BEC in a harmonic potential. **b.** Interaction driven expansion of a BEC in time-of-flight for a trap with trapping frequencies $(\omega_x, \omega_y, \omega_z) = 2\pi(42, 34, 133)$ Hz obtained by numerically integrating Equation 2.30.

2.3 Density profiles

Most ultracold atoms experiments are probed by directly imaging the atoms (e.g. with absorption imaging, Section 3.5). If the atoms are imaged in-situ we gain access to their spatial density profiles. If the atoms are released from the trap and allowed to expand in time of flight (TOF) we gain access to their momentum distribution. In this section I summarize the signatures in the density distributions of BECs and thermal atoms confined in a harmonic potential both in-situ and after TOF.

For the case of a BEC confined in a harmonic potential at zero temperature (no thermal fraction) and in the Thomas-Fermi regime discussed in Section 2.2.3, the in-situ density distribution is described by

$$\begin{aligned} n(\mathbf{r}) &= n_0 \left(1 - \frac{x^2}{R_x^2} - \frac{y^2}{R_y^2} - \frac{z^2}{R_z^2} \right) \\ &= \frac{15N}{8\pi R_x R_y R_z} \left(1 - \frac{x^2}{R_x^2} - \frac{y^2}{R_y^2} - \frac{z^2}{R_z^2} \right). \end{aligned} \quad (2.29)$$

Even though the BEC is in the motional ground state, it will expand during TOF as a consequence of interactions. The expansion can be determined using the time dependent GP equation. A detail account of the procedure can be found in [5], the procedure relies on using the ansatz that the TF radii expand as

$$R_i(t) = \lambda_i(t) R_i(t=0), \quad (2.30)$$

where I assumed that the condensate is in the trap at $t = 0$ which implies that $\lambda_i(0) = 1$. The trap is then suddenly turned off at $t > 0$. If we insert the condensate wave function with TF radii given by Equation 2.30 into the time-dependent GP equation we find a series differential equations

$$\frac{d^2\lambda_i}{dt^2} = \frac{\omega_i^2}{\lambda_i \lambda_x \lambda_y \lambda_z} \quad (2.31)$$

which can be used to determine the density profile of the BEC in TOF. Alternatively if the density profile of the BEC is known from an image, these relations can be used to back-propagate what the original TF radii of the confined condensate was. This is helpful for example to calculate the atom number in the condensate using Equation 2.28. Figure 2b shows the scaling factors λ_i as a function of TOF that were obtained by numerically integrating Equation 2.30 for a harmonic potential with frequencies close to those characterizing the optical dipole trap used in the lab.

For a thermal gas in a harmonic potential at temperatures higher than the level spacing $k_B T > \hbar\omega_{x,y,z}$ the density is given by [1]

$$n_{\text{th}}(\mathbf{r}) = \frac{1}{\lambda_{\text{th}}^3} g_{3/2}(z(\mathbf{r})) \quad (2.32)$$

where $z(\mathbf{r}) = \exp(\mu - V(\mathbf{r})/\mathbf{k}_B T)$, $V(\mathbf{r})$ is given by Equation 2.11, μ is the chemical potential and $g_j(z) = \sum_i z^i / i^j$ is the Bose function. The Bose function introduces effects of quantum statistics and compared to the Maxwell-Boltzmann distribution of distinguishable particles, the peak density of a Bose gas is increased by $g_{3/2}(z)/z$,

a phenomenon known as Bose-enhancement.

The distribution after TOF can be calculated considering that the trapped atoms fly ballistically from their position in the trap. An atom starting initially at the point \mathbf{r}_0 moves to the point \mathbf{r} after a time t if its momentum is given by $\mathbf{p} = m(\mathbf{r} - \mathbf{r}_0)/t$, and it can be shown that

$$\begin{aligned} n_{\text{tof}} &= \frac{1}{\lambda_{\text{th}}} \prod_{i=1}^3 g_{3/2} \left(\exp \left[\mu - \frac{m}{2} \sum_{i=1}^3 x_i^2 \left(\frac{\omega_i^2}{1 + \omega_i^2 t^2} \right) \right] \right) \\ &\approx \frac{1}{\lambda_{\text{th}}} g_{3/2} \left(\exp \left[(\mu - \frac{mr^2}{2t^2})/k_B T \right] \right) \end{aligned} \quad (2.33)$$

where the approximation in the second line is valid for $t \gg \omega_i^{-1}$. The temperature of the atoms can be estimated by looking at the wings of the density distribution after TOF. Even with the case of Bose enhancement, the density of the wings still decays exponentially as $\exp(-x_i^2/2\sigma_i^2)$. The temperature of the cloud can be determined using

$$\begin{aligned} k_B T &= \frac{m}{2} \left(\frac{\omega_i^2}{1 + \omega_i^2 t^2} \sigma_i^2 \right) \\ &\approx \frac{m}{2} \left(\frac{\sigma_i}{t} \right)^2 \end{aligned} \quad (2.34)$$

For partially condensed clouds the density profiles will be given by a combination of the thermal density profiles and the Thomas-Fermi density profile. Figure 3 shows the density distributions of atoms extracted from images taken after a 21 ms TOF and therefore position is mapped to momentum. The images also nicely summarize some of the main features discussed in this Chapter. Above T_c the density

profile of the atoms is described by the thermal distribution (Equation 2.33). When $T < T_c$ a small peak in the center of the thermal distribution appears indicating condensation and as temperature is decreased the fraction of atoms in the condensed state (and therefore the height of the peak) increases. The density distribution of the condensed atoms is given by Equation 2.29, where the TF radius increases due to interactions and the scaling factors can be found using Equation 2.30.

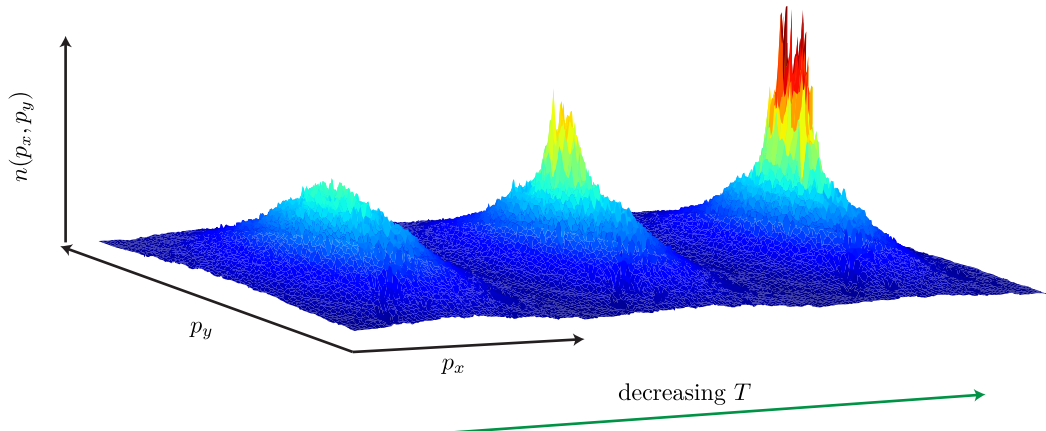


Figure 3: Momentum distribution of atoms near T_c after a 21 ms TOF. As the atoms are cooled below T_c a sharp peak in the momentum distribution appears indicating condensation.

Chapter 3: Manipulation and detection of ultra-cold atoms

All of the experiments described in this thesis were performed using ultracold clouds of ^{87}Rb . In this Chapter I describe the techniques and interactions that make our experiments possible. This Chapter is not an extensive survey of atomic physics but rather covers the topics that are most relevant to my experiments. The references I included are helpful if the reader is interested in learning the details of the derivations or wants to expand on a given topic. I start by describing the electronic structure of ^{87}Rb . Then I review the interactions of atoms with magnetic fields and its application to magnetic trapping. I describe the foundations of atom-light interactions that make possible both laser cooling and trapping of atoms and give rise to Raman induced transitions. Finally I discuss coherent processes that use the magnetic and electric dipole interaction and are relevant to the experiments presented in Chapters 5, 6 and 8. Finally, I discuss resonant absorption imaging which is used to detect atoms after all our experiments are performed.

3.1 Electronic structure of ^{87}Rb

Rb is an Alkali metal (also Li, which exists in our vacuum chamber but was never used). Alkali metals correspond to the first group (leftmost column) of the

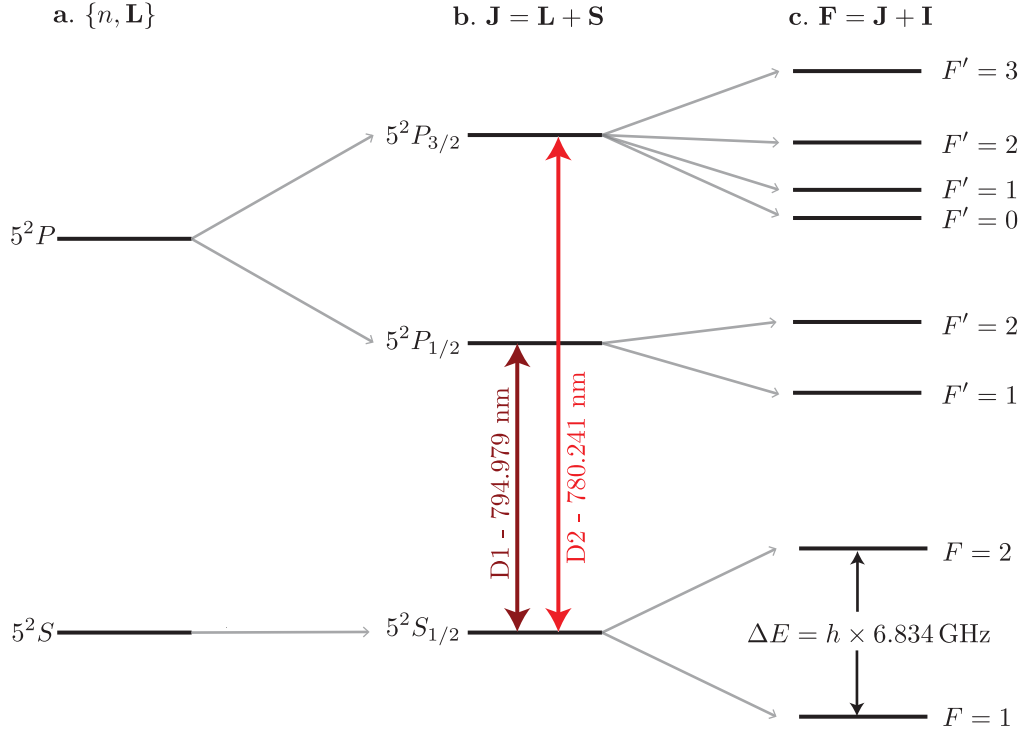


Figure 1: ^{87}Rb level structure (not to scale). **a.** Ground and first excited state electronic configuration of ^{87}Rb given by the $\{n, \mathbf{L}\}$ quantum numbers. **b.** The interaction between the orbital angular momentum and the spin of the electron leads to the fine structure splitting of orbitals with $L > 0$. The splitting of the 5^2P line gives rise to the D1 and D2 lines. **c.** The interaction between the total angular momentum and the nuclear spin causes the fine structure levels to split further into states characterized by the quantum number F .

periodic table and are characterized by having a single valence electron, which makes the description of their internal structure much simpler than that of other elements. We can describe the state of an electron in an atom by its angular momentum $\hat{\mathbf{L}}$ and its spin $\hat{\mathbf{S}}$. Because of Pauli's exclusion principle there can not be two electrons with the same quantum numbers and in multi-electron atoms they tend to fill ‘shells’ of different angular momentum values, historically labeled by the letters

S , P , D , F , ...¹ (corresponding to $L = 0, 1, 2, 3, \dots$). In particular Rb has 4 filled shells and one electron in the $5S$ shell, where the number 5 corresponds to the principal quantum number n . Figure 1 shows the energy levels of the ground state $5S$ and its closest $5P$ orbital.

The atomic level structure is modified by relativistic effects. In particular the relativistic treatment of the electron's motion gives rise to an interaction between the electron's intrinsic magnetic moment (the spin) $\hat{\mathbf{S}}$ and the orbital angular momentum $\hat{\mathbf{L}}$. This spin-orbit coupling interaction $\hat{H}_{\text{fs}} = A_{\text{fs}} \mathbf{L} \cdot \mathbf{S}$ causes the fine structure splitting of the electronic orbitals into levels with different total electronic angular momentum $\hat{\mathbf{J}} = \hat{\mathbf{L}} + \hat{\mathbf{S}}$. Figure 1b show the $5^2S_{1/2}$, $5^2P_{1/2}$ and $5^2P_{3/2}$ electronic configurations that arise from this splitting, where I introduced the spectroscopic notation $n^{2S+1}L_J$ that indicates the values of the relevant quantum numbers. For S ($L = 0$) orbitals $J = 1/2$ is the only possible value and the levels are not split. For the P orbital ($L = 1$) J and a single electron with $S = 1/2$, J can be $1/2$ or $3/2$ and the P orbital splits into two levels. The $5^2S_{1/2} \rightarrow 5^2P_{1/2}$ is known as the D1 line and has wavelength $\lambda = 794.979 \text{ nm}$ and $5S_{1/2} \rightarrow 5P_{3/2}$ transition is known as the D2 line and has $\lambda = 790.241 \text{ nm}$ [9].

The atomic level structure gets further modified by the magnetic interaction of the electron with the nuclear spin \mathbf{I} . This is another kind of spin-orbit interaction that gives rise to the hyperfine splitting of the atomic levels which can be described by the Hamiltonian $\hat{H}_{\text{hfs}} = A_{\text{hfs}} \mathbf{I} \cdot \mathbf{J}$. A complete derivation of \hat{H}_{hfs} can be found

¹This terms were used to describe the lines in the emission spectra when they were first discovered. S stands for sharp, P for principal D for diffuse and F for further noted

in [10]. The hyperfine levels correspond to different values of the total angular momentum $\hat{\mathbf{F}} = \hat{\mathbf{J}} + \hat{\mathbf{I}}$. For ^{87}Rb $I = 3/2$ [9] which results in the level structure shown in Figure 1c.

3.2 Interaction between atoms and magnetic fields

Atoms have an intrinsic magnetic moment that is given by the sum of nuclear and electronic moments

$$\hat{\boldsymbol{\mu}} = -\frac{\mu_B}{\hbar}(g_S \hat{\mathbf{S}} + g_L \hat{\mathbf{L}} + g_I \hat{\mathbf{I}}) \quad (3.1)$$

where μ_B is the Bohr magneton and g_S , g_L and g_I are the ‘ g -factors’ corresponding to the spin, orbital and nuclear angular momentum. In the presence of an external magnetic field \mathbf{B} , the internal levels of an atom get modified due to the Zeeman [11] interaction

$$\hat{H}_{\text{Zeeman}} = -\hat{\boldsymbol{\mu}} \cdot \mathbf{B}. \quad (3.2)$$

If the energy shift due to the Zeeman interaction is small compared to the hyperfine splitting so that F is a good quantum number we can write

$$\hat{H}_{\text{Zeeman}} = \frac{\mu_B g_F}{\hbar} \hat{\mathbf{F}} \cdot \mathbf{B} \quad (3.3)$$

where is the hyperfine Landé g -factor

$$g_F = g_J \frac{F(F+1) - I(I+1) + J(J+1)}{2F(F+1)} + g_I \frac{F(F+1) + I(I+1) - J(J+1)}{2F(F+1)} \quad (3.4)$$

and

$$g_J \approx 1 + \frac{J(J+1) + S(S+1) - L(L+1)}{2J(J+1)}. \quad (3.5)$$

is the Landé g -factor associated to the total electronic angular momentum J . The total energy shifts can be calculated by diagonalizing the full atomic Hamiltonian including the fine and hyperfine structure terms. Figure 2 shows the energies of the m_F levels in the $F = 1$ and $F = 2$ manifolds of the $5^2S_{1/2}$ electronic ground state of ^{87}Rb as a function of magnetic field. If the magnetic field is small then the Zeeman term can be treated as a perturbation to the atomic Hamiltonian and the energy split is linear with the magnitude of the field $E_{m_F} = g_F \mu_B m_F B$, what is known as the ‘linear Zeeman regime’ where F and m_F are good quantum numbers. In contrast, in the ‘Pachen-Back regime’ at large magnetic fields² the Zeeman term dominates over the fine and hyperfine terms and therefore the good quantum numbers of the system are J and m_J . Our experiments typically operate in an intermediate regime ($B \sim 10 - 30$ G, the gray box in Figure^o 2) where the energy of $m_F = 0$ gets a small shift in energy that is quadratic in B . For atoms in $F = 1$ we define this quadratic Zeeman shift as $\epsilon = E_0 - (E_{+1} - E_{-1})/2$, where E_{m_F} is the Zeeman shift for state m_F .

²A couple orders of magnitude larger than the fields we operate at.

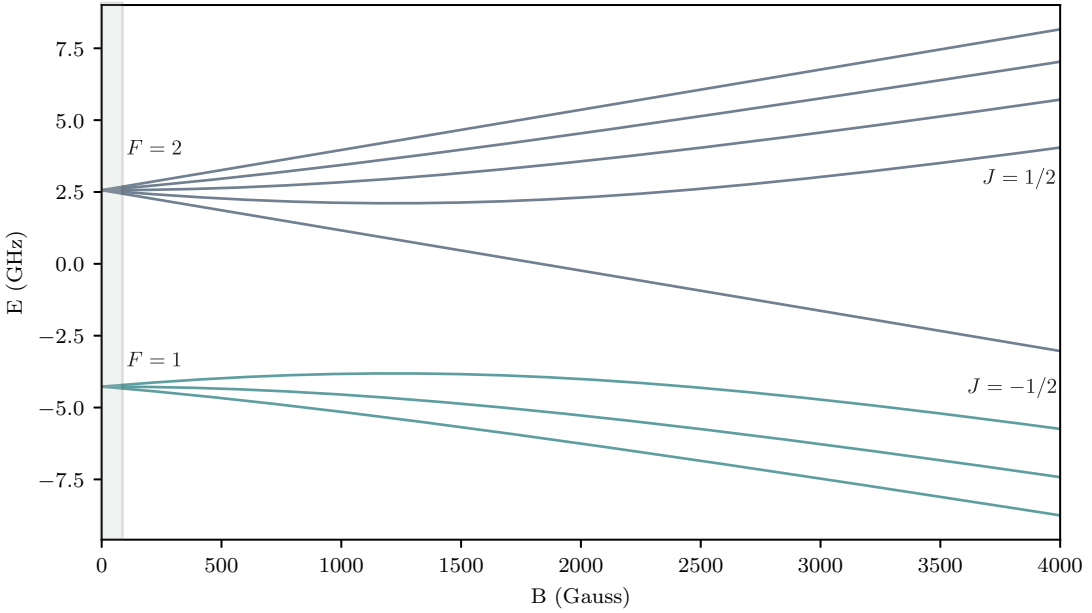


Figure 2: Zeeman splitting of the $5^2S_{1/2}$ manifold of ^{87}Rb . At small magnetic fields F and m_F are good quantum numbers describing the system and at large magnetic fields (Pachen-Back regime) the states are described by the J and m_J . Our experiments operate in the regime marked by the small gray box ($B < 35$ G).

For the particular case of $J = 1/2$ (like the ground state of Alkalies) the Zeeman energies can be found analytically using the Breit-Rabi formula [12]

$$E_{m_F} = -\frac{1}{2(2I+1)} + \frac{\mu_B g_I m_F B}{\Delta E_{\text{hf}}} + \frac{1}{2} \sqrt{1 + \frac{4m_F}{2I+1}x + x^2}, \quad (3.6)$$

where $\Delta E_{\text{hf}} = A_{\text{hf}}(J + 1/2)$ and $x = (g_J - g_I)\mu_B B_z / \Delta E_{\text{hf}}$. Figure 2 shows the energies of the m_F levels for the $F = 1$ and $F = 2$ manifolds of ^{87}Rb .

3.2.1 Magnetic trapping

The sign of the Zeeman energy for different m_F state can be used to create state dependent traps for atoms. In the lab we implement magnetic traps using quadrupole magnetic fields produced by a pair of anti-Helmholtz coils. The magnetic field near the center of the coils can be written as

$$\mathbf{B} = B'(x\mathbf{e}_x + y\mathbf{e}_y - 2z\mathbf{e}_z) + \mathbf{B}_0 \quad (3.7)$$

where \mathbf{B}_0 is a constant magnetic field, for simplicity I will assume that $\mathbf{B}_0 = B_0\mathbf{e}_z$.

The Zeeman Hamiltonian gives a trapping potential

$$\begin{aligned} U(\mathbf{r}) &= g_F\mu_B m_F B \\ &= g_F\mu_B m_F B' \sqrt{x^2 + y^2 + 4 \left(z - \frac{B_0}{2B'} \right)^2} \\ &\approx g_F\mu_B m_F B' \left(\rho + 2 \left| z - \frac{B_0}{2B'} \right| \right) \end{aligned} \quad (3.8)$$

where $\rho^2 = x^2 + y^2$ and the approximation on the second line is valid for small displacements from the trap center.

The sign of the magnetic moment determines which states can be trapped. For ^{87}Rb the $|F = 1, m_F = -1\rangle$, $|F = 2, m_F = 2, 1\rangle$ are magnetically trappable. The state $|F = 2, m_F = 0\rangle$ is also weakly magnetically trappable due to the quadratic Zeeman shift.

In addition to generating trapping potentials. We use quadrupole fields in the

lab before imaging the atoms to generate state dependent forces that allow us to separate the different m_F states.

3.3 Interaction between atoms and electric fields

In this section I will discuss the interaction between atoms and electric fields. After laying the foundations I will discuss applications using off-resonant electro-magnetic radiation such as optical dipole traps and Raman transitions. I will not cover laser cooling which has been covered extensively in the literature [13, 14] and PhD theses from previous group members [15, 16].

In the presence of an electric field \mathbf{E} an atom can become polarized and therefore its energy levels get modified by the Stark effect [17]. If the electric field is spatially uniform with respect to the atom's size we consider the electric field as a classical object and its effect on the atom can be described by the Hamiltonian [18]

$$\hat{H}_{\text{dip}} = -\hat{\mathbf{d}} \cdot \mathbf{E}, \quad (3.9)$$

where $\hat{\mathbf{d}} = -e \sum_j \hat{r}_j$ is the atomic dipole operator, e is the electron charge and \hat{r}_j are the position operators of the atom's electrons relative to the center of mass of the atom. This approximation, known as the dipole approximation, is valid for electromagnetic radiation when the wavelength is much larger than the size of an atom $\lambda \gg r_{\text{atom}}$ [19].

First I consider the simplified case a two-level system interacting with a coherent electromagnetic field $\mathbf{E} = \mathbf{E}^{(+)} e^{-i\omega t} + \mathbf{E}^{(-)} e^{i\omega t}$, where $\mathbf{E}^{(\pm)} = \hat{\epsilon} E^{(\pm)}$ are the

positive/negative frequency components of the field, $\hat{\epsilon}$ the polarization, and ω is the angular frequency. Using second order perturbation theory it can be shown that Stark shift of the ground state is

$$\begin{aligned}\Delta E_g &= -\frac{2\omega_{eg}|\langle g| \hat{\epsilon} \cdot \mathbf{d} |e\rangle|^2 |E^{(+)}|^2}{\hbar(\omega_{eg}^2 - \omega^2)} \\ &= -\frac{1}{2}\alpha(\omega)E^2\end{aligned}\quad (3.10)$$

where $\omega_{eg} = (E_e - E_g)/\hbar$ is the angular frequency associated to the energy splitting of the two states and $\alpha(\omega)$ is a dynamic polarizability. Things are a bit more complicated with real atoms though, and we need to take into account all the atomic levels. Furthermore, there are degeneracies associated to the different angular momentum states so we have to be more careful with the orientation of the atom and the field. To take these effects into account one can introduce a generalization of the polarizability [19, 20] which takes the form

$$\begin{aligned}\alpha_{\mu\nu}(\omega) &= \sum_j \frac{2\omega_{jg} \langle g| d_\mu |e_j\rangle \langle e_j| d_\nu |g_j\rangle}{\hbar(\omega_{jg}^2 - \omega^2)} \\ &= \sum_{F', m_{F'}} \frac{2\omega_{F'F} \langle F, m_F| d_\mu |F', m_{F'}\rangle \langle F', m_{F'}| d_\nu |F, m_F\rangle}{\hbar(\omega_{F'F}^2 - \omega^2)}.\end{aligned}\quad (3.11)$$

Here $|e_j\rangle$ represent the excited states and $\omega_{jg} = (E_j - E_g)/\hbar$ and the expression in the second line corresponds the polarizability for the hyperfine levels of an atom in the ground state $|F, m_F\rangle$. We can therefore write an effective Hamiltonian for the

Stark shift as

$$\hat{H}_{\text{Stark}} = -\alpha_{\mu\nu}(\omega) E_\mu^{(+)} E_\nu^{(-)}. \quad (3.12)$$

The polarizability is a rank-2 tensor operator and can be represented by 3 irreducible tensor operators (see [19] for a complete derivation). In the limit of small magnetic fields so that F and m_F are good quantum numbers describing the state of the atom $|n, F, m_F\rangle$ the dipole Hamiltonian in this representation takes a convenient form

$$\begin{aligned} \hat{H}_{\text{Stark}} = & \alpha^{(0)} (\mathbf{E}^{(-)} \cdot \mathbf{E}^{(+)}) + i\alpha^{(1)} (\mathbf{E}^{(-)} \times \mathbf{E}^{(+)}) \cdot \hat{\mathbf{F}} \\ & + \alpha^{(2)} E_i^{(-)} E_j^{(+)} \left(\frac{1}{2}(F_i F_j + F_j F_i) - \frac{1}{3} \hat{\mathbf{F}}^2 \delta_{i,j} \right), \end{aligned} \quad (3.13)$$

where $\alpha^{(0)}$, $\alpha^{(1)}$ and $\alpha^{(2)}$ are the scalar, vector and tensor polarizabilities respectively and $\hat{\mathbf{F}}$ is the total angular momentum operator. For all our experiments $\alpha^{(2)}$ is very small so I will limit the discussion to the effect of the first two terms. The scalar term is responsible for the dipole force that allow us to trap atoms using off-resonant light and the vector component is necessary for engineering spin-orbit coupling and other spin-dependent potentials through two-photon processes.

3.3.1 Scalar polarizability

The scalar polarizability takes the form

$$\alpha^{(0)} = \sum_j \frac{2\omega_{jg} |\langle g | \mathbf{d} \cdot \hat{\epsilon} | e_j \rangle|^2}{\hbar(\omega_{jg}^2 - \omega^2)}, \quad (3.14)$$

where the matrix element can be expressed in terms of the Clebsch-Gordan coefficients and the reduced matrix element using the Wigner-Eckart theorem [21]. For the ground state of an Alkali atom ($J = 1/2$) and if the detuning is large compared to the hyperfine splitting the expression above gets simplified to

$$\alpha^{(0)} \approx \sum_{J'} \frac{2\omega_{JJ'} |\langle J = 1/2 | \mathbf{d} | J' \rangle|^2}{3\hbar(\omega_{JJ'}^2 - \omega^2)}. \quad (3.15)$$

Due to the second order perturbation theory treatment, the scalar polarizability can be interpreted as arising from a two-photon process where the atom absorbs an off-resonant photon and then returns to its initial state by emitting a photon.

The dipole matrix elements needed to compute the polarizability are related to the transition scattering rate via Fermi's golden rule [19, 21]

$$\Gamma_{JJ'} = \frac{\omega_{JJ'}^2}{3\pi\epsilon_0\hbar c^3} \frac{2J+1}{2J'+1} |\langle J | \mathbf{d} | J' \rangle|^2, \quad (3.16)$$

and combining this with the expression for the intensity of the electric field $I(\mathbf{r}) = 2\epsilon_0 c |\mathbf{E}(\mathbf{r})|^2$ it can be shown that for linearly polarized light the energy of the ground

state manifold is shifted by

$$U(\omega, \mathbf{r}) = -\frac{\pi c^2 I(\mathbf{r})}{2} \left[\frac{\Gamma_{D1}}{\omega_{D1}^3} \left(\frac{1}{\omega + \omega_{D1}} - \frac{1}{\omega - \omega_{D1}} \right) + \frac{2\Gamma_{D2}}{\omega_{D2}^3} \left(\frac{1}{\omega + \omega_{D2}} - \frac{1}{\omega - \omega_{D2}} \right) \right], \quad (3.17)$$

where only the most significant contribution from the closest transitions (the D1 and D2 lines) are included. Here $U(\mathbf{r})$ is related to the real part of the polarizability which is in fact a complex valued number. So far I have only considered a real valued polarizability by assuming the excited states have an infinitely long lifetime. However, in reality the atom can spontaneously emit photons and decay. This exponential decay can be accounted for by adding an imaginary contribution to the energies $\omega_D \rightarrow \omega_D + i\Gamma_D \omega^3 / \omega_D^3$ of the D1 and D2 transitions [22]. The scattering rate is related to the imaginary part of the polarizability and is given by

$$\Gamma(\omega, \mathbf{r}) = \frac{\pi c^2 I(\mathbf{r})}{2\hbar} \left[\frac{\Gamma_{D1}\omega^3}{\omega_{D1}^6} \left(\frac{1}{\omega + \omega_{D1}} - \frac{1}{\omega - \omega_{D1}} \right)^2 + \frac{2\Gamma_{D2}\omega^3}{\omega_{D2}^6} \left(\frac{1}{\omega + \omega_{D2}} - \frac{1}{\omega - \omega_{D2}} \right)^2 \right] \quad (3.18)$$

The energy shift $U(\omega, \mathbf{r})$ is a conservative term and is related to dipole trapping, while the scattering term $\Gamma(\omega, \mathbf{r})$ is dissipative and is important for laser cooling. In the context of engineering potentials for ultracold atoms with off-resonant light, the scattering is translated into heating because every time an atom emits a photon with angular frequency ω_L it gets a recoil momentum $\hbar\mathbf{k}_L$. If the frequency ω satisfies the relation $\omega + \omega_D \gg \omega - \omega_D$, as is often the case, we can neglect the terms proportional to $1/(\omega + \omega_D)$, an approximation typically known as the rotating wave approximation (RWA). If the RWA is valid then the frequency dependence of

both the energy shifts and the scattering rates will be given by the detuning from the D1 and D2 transitions.

3.3.1.1 Optical trapping

One important application of the scalar light-shift is to create optical traps for clouds of ultracold atoms. An optical field with non-uniform spatial intensity generates traps (and anti-traps) for the atoms which experience a force proportional to the intensity gradient $F_{\text{dip}} = -\nabla U(\mathbf{r})$. The attractive or repulsive nature of the trap depends on the sign of $U(\mathbf{r})$ which is determined by the sign of the detuning (blue-detuned traps are repulsive and red-detuned traps are attractive)[**TODO: make nice figure of dipole trap if I have time**]. The production of BECs in our lab relies on the use of focused Gaussian laser beams with $\lambda = 1064 \text{ nm}$. The intensity profile of a focused Gaussian beam propagating along \mathbf{e}_z is given by

$$I(x, y, z) = \frac{2P}{\pi\omega^2(z)} e^{-\frac{x^2+y^2}{\omega^2(z)}} \quad (3.19)$$

where P is the total power of the beam and the $1/e^2$ radius is given by $w(z) = w_0\sqrt{1+z^2/z_R^2}$ where the minimum radius w_0 is known as the waist and $z_R = \pi\omega_0^2/\lambda$ is the Rayleigh range. If the extent of an atomic cloud is small compared to the size of the beam we can perform a Taylor expansion around $\mathbf{r} = 0$ to obtain the trapping potential

$$U(\mathbf{r}) = -U_0 \left(1 - 2\frac{x^2 + y^2}{\omega_0^2} - \frac{z^2}{z_R^2} \right). \quad (3.20)$$

The oscillation frequencies of the trap along the radial direction are $\omega_r = (4U_0/m\omega_0^2)^{1/2}$ and along the axial direction $\omega_z = (2U_0/mz_R)^{1/2}$. The beam waist is usually much smaller than the Rayleigh range ($\omega_0 \sim 50 - 150 \mu\text{m}$ for my experiments) and therefore the trap is much stronger along the axial direction. To get around this we use a ‘crossed dipole trap’ which is formed by a combination of two cross-polarized³ and frequency shifted focused Gaussian beams propagating along perpendicular axes, ensuring that we get good confinement of atoms along all spatial directions.

3.3.2 Vector polarizability and effective magnetic fields

In general the expressions for the vector polarizability are quite complicated and depend both on reduced matrix elements and Wigner $6 - j$ symbols (see [19] for example for the complete expressions). For the particular case of Alkali atoms in the large detuning regime the vector polarizability takes a simplified form [23]

$$\alpha^{(1)} = \frac{2\Delta_{\text{fs}}\alpha^{(0)}}{3(\tilde{E} - \hbar\omega)} \quad (3.21)$$

where $\Delta_{\text{fs}} = 3A_{\text{fs}}/2$ and $\tilde{E} = (2E_{\text{D}_1} + E_{\text{D}_2})$.

If we recall the Zeeman Hamiltonian introduced in Section 3.2, the term proportional to the vector polarizability in Equation 3.13 looks very similar to Equation 3.2 for an effective magnetic field

$$\mathbf{B}_{\text{eff}} = -\frac{i\hbar}{\mu_B g_J} \alpha^{(1)} (\mathbf{E}^* \times \mathbf{E}). \quad (3.22)$$

³The beams are cross-polarized to avoid interference between them

For the intensities that we typically operate at, the vector light shift is small and can be treated as a perturbation. The Hamiltonian resulting from this effective magnetic field can be written as

$$\hat{H}_{\text{eff}} = \frac{\mu_B g_F}{\hbar} \mathbf{B}_{\text{eff}} \cdot \hat{\mathbf{F}} \quad (3.23)$$

3.3.2.1 Raman coupling

The vector light shift enables the realization of various spin dependent potentials in the lab. In the experiments presented in Chapters 5 and 8 I used combinations of cross polarized laser beams such that the total electric field $\mathbf{E}^* \times \mathbf{E} \neq 0$ and we induced two-photon Raman transitions. A Raman transition is also a two-photon process, but instead we consider two ground states and an intermediate state that is off-resonantly coupled as is shown in Figure 3a. Due to the large detuning, the population transferred into the intermediate state is negligible and the state can be adiabatically eliminated [24]. In our experiments we typically couple the m_F levels of the $F = 1$ manifold after applying a bias magnetic field such that ϵ is non-negligible.

Consider two laser beams counter propagating along \mathbf{e}_x and with polarizations along \mathbf{e}_y and \mathbf{e}_z as is shown in Figure 3b. The electric field from the Raman beams is given by

$$\mathbf{E}(x, t) = E_a \cos(k_a x - \omega_a t) \mathbf{e}_y + E_b \cos(k_b x + \omega_b t) \mathbf{e}_z, \quad (3.24)$$

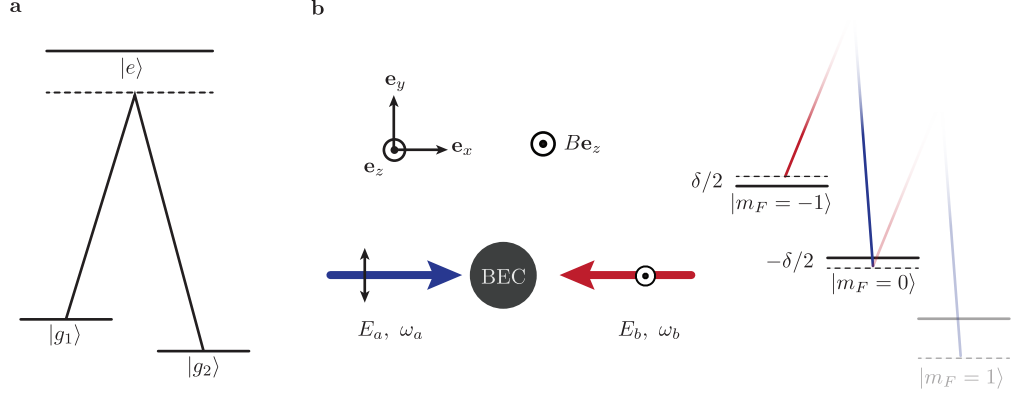


Figure 3: **a.** A Raman transition is a two photon process that couples two ground state through and intermediate far detuned state. **b.** We induce Raman transitions using a pair of cross-polarized laser beams whose and we set the difference in their angular frequencies close to the Zeeman splitting between two consecutive m_F states.

and consequently

$$\mathbf{E}^* \times \mathbf{E} = 2iE_aE_b \cos(2k_Lx - \omega_{a,b}t)\mathbf{e}_x, \quad (3.25)$$

where $\omega_{a,b} = \omega_a - \omega_b$. The Raman Hamiltonian is given by

$$\hat{H}_R = \Omega \cos(2k_Lx - \omega_{a,b}t) \hat{F}_x \quad (3.26)$$

where $\Omega = \alpha^{(1)} g_F E_a E_b / g_J \propto \sqrt{I_a I_b}$ is the Raman coupling strength. The geometry and wavelength of the Raman fields determine the natural units of the system: the single photon recoil momentum $k_L = 2\pi/\lambda_R$ and its associated recoil energy $E_L = \hbar^2 k_L^2 / 2m$, as well as the direction of the recoil momentum $\mathbf{k}_L = k_L \mathbf{e}_x$. For most experiments we tune to what is known as the ‘magic wavelength’ or tune-out wavelength [25] $\lambda_R = 790.034$ nm, at which the ground-state scalar polarizability vanishes and the scattering rate is reduced (Figure 4a,c). We occasionally had to tune away from the magic wavelength, for example when we were starving for

laser power and wanted to increase our Raman coupling strength. An important metric for us is Raman coupling strength and Figure 4b shows its dependence on wavelength; tuning closer to resonance allows us to decrease the laser intensity for the same experiment but comes with increased scattering rates and reduced lifetime as can be seen in Figure 4d which shows the decay in number of Raman dressed atoms as a function of time for different wavelengths.

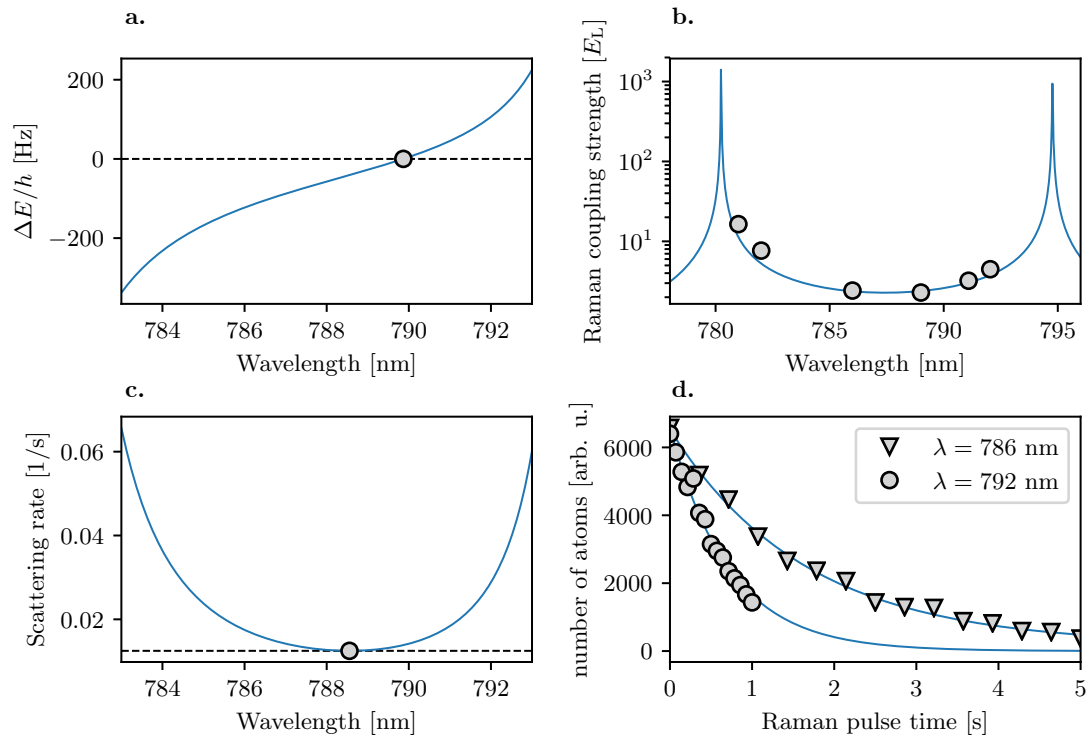


Figure 4: **a.** Scalar polarizability as a function of wavelength near the D1 and D2 lines of ^{87}Rb . We typically tune our Raman laser beams near the magic wavelength $\lambda = 790.034 \text{ nm}$. **b.** Raman coupling strength as a function of wavelength measured for a pair of Raman beams with waist $w_0 \sim 150 \mu\text{m}$ and powers of 50, 10 mW. **c.** Scattering rate as a function of wavelength, while it is not minimized at 790 nm its value is kept relatively low. **d.** Decay in number of Raman dressed atoms as a function of hold time for the same beam parameters as in **b.**. At $\lambda = 786 \text{ nm}$ the $1/e$ lifetime is $\tau = 1.64 \text{ s}$ and for $\lambda = 792 \text{ nm}$ it is reduced to $\tau = 0.72 \text{ s}$.

In a frame rotating with angular frequency $\omega_{a,b}$ corresponding to applying the unitary transformation $\hat{U}(t) = \exp(-i\omega_{a,b}t\hat{F}_z)$ and neglecting the fast terms rotating at frequency $2\omega_{a,b}$ (applying a RWA) the transformed Hamiltonian is

$$\hat{U}^\dagger \hat{H}_R \hat{U} - i\hbar \hat{U}^\dagger \partial_t \hat{U} = \omega_{a,b} \hat{F}_z + \frac{\Omega}{2} \cos(2k_L x) \hat{F}_x - \frac{\Omega}{2} \sin(2k_L x) \hat{F}_y, \quad (3.27)$$

which describes a helically precessing magnetic field with period $\lambda_R/2$.

3.3.2.2 Spin-orbit coupling

The Raman Hamiltonian from Equation 3.27 can be massaged a bit more to make it look like a spin-orbit coupled (SOC)⁴ Hamiltonian that is familiar to condensed matter physicists. If we apply a spin-dependent momentum boost which is described by the unitary operator $\hat{U}(k_L) = \exp(i2k_L x \hat{F}_z)$ the full Hamiltonian including the Raman coupling and the free particle energies is transformed to

$$\hat{H}_{\text{SOC}} = \frac{\hbar^2}{2m} (\hat{q}_x - 2k_L \hat{F}_z)^2 + \frac{\Omega}{2} \hat{F}_x + \delta \hat{F}_z + \hbar \epsilon \left(\mathbb{1} - \frac{\hat{F}_z^2}{\hbar^2} \right), \quad (3.28)$$

where $\delta = E_{-1} - \omega_{a,b}$. We can go from a 3 level system to an effective spin-1/2 system if we set $\Delta\omega = E_{-1} - E_0$ and consider a sizable quadratic Zeeman shift ϵ , the $m_F = 1$ state can be adiabatically eliminated [26] and the Hamiltonian becomes

$$\hat{H}_{\text{SOC}} = \frac{\hbar^2}{2m} (q_x - k_L \hat{\sigma}_y)^2 + \frac{\hbar}{2} \Omega \hat{\sigma}_z + \frac{\hbar}{2} \delta \hat{\sigma}_y \quad (3.29)$$

⁴Not to be confused with the spin-orbit coupling giving rise to the fine and hyperfine structure mentioned earlier, perhaps a better name could be spin-momentum coupling

where $\sigma_{x,y,z}$ are the Pauli matrices. The Hamiltonian above corresponds to an equal superposition of Rashba-type [27] ($\propto \hat{\sigma}_x k_y - \hat{\sigma}_y k_x$) and Dresselhaus-type [28] ($\propto -\sigma_x k_y - \sigma_y k_x$) SOC with an effective magnetic field $\propto \Omega$ in the $\mathbf{e}_y - \mathbf{e}_z$ plane [26, 29].

In Chapter 8 I discuss the Rashba term in more detail and introduce a way of engineering a system with only Rashba-type SOC using multiple internal levels and Raman transitions.

3.4 Coherent manipulation

In this section I describe quantum coherent processes that are driven within the electronic grounds state using the magnetic and electric dipole interactions described in previous sections. We rely on this techniques both for state preparation and characterization of our system. In all of the cases I consider a system described by the Hamiltonian

$$\hat{H} = \hat{H}_0 + \hat{H}_I(t) \quad (3.30)$$

where \hat{H}_0 describes unperturbed atomic levels and $\hat{H}_I(t)$ is a time dependent interaction. For simplicity I consider only a two-level system

$$\hat{H}_0 = \hbar \begin{pmatrix} \omega_g & 0 \\ 0 & \omega_e \end{pmatrix} \quad (3.31)$$

where with $|g\rangle$ and $|e\rangle$ are the unperturbed ground and excited states with energy $\hbar\omega_i$ are the energies of the unperturbed states.

3.4.1 Rabi oscillations

First I consider an interaction term that oscillates with frequency ω close to the transition energy $\omega_{ge} = \omega_g - \omega_e$

$$\hat{H}_I = \hbar \begin{pmatrix} 0 & \Omega \cos(\omega t) \\ \Omega^* \cos(\omega t) & 0 \end{pmatrix} \quad (3.32)$$

the coupling strength Ω here could be related to an electric dipole transition $\Omega \propto \langle g | \mathbf{d} \cdot \mathbf{E} | e \rangle$ ⁵ or magnetic dipole $\Omega \propto \langle g | \boldsymbol{\mu} \cdot \mathbf{B} | e \rangle$ transition matrix element. The state of the system at any given time is given by

$$|\Psi\rangle = c_g(t)e^{-i\omega_g t} |g\rangle + c_e(t)e^{-i\omega_e t} |e\rangle, \quad (3.33)$$

and substituting this expression into the time dependent Schrödinger equation we find that

$$\begin{aligned} \dot{c}_g(t) &= \frac{\Omega}{2} \left(e^{i(\omega-\omega_{ge})t} + e^{-i(\omega+\omega_{ge})t} \right) c_e \\ \dot{c}_e(t) &= \frac{\Omega^*}{2} \left(e^{i(\omega-\omega_{ge})t} + e^{-i(\omega+\omega_{ge})t} \right) c_g. \end{aligned} \quad (3.34)$$

We can apply a RWA if the term $\omega + \omega_{ge}$ is large compared to $\omega - \omega_{ge}$. The resulting coupled differential equations can be solved in a standard way by differentiating \dot{c}_e one more time and substituting \dot{c}_g . If we assume that at $t = 0$ the system is prepared

⁵For our system intensities $\Gamma \gg \Omega$ and we don't observe Rab oscillations from (single photon) electric dipole transitions.

in $|g\rangle$ the population in $|e\rangle$ describes what is known as a Rabi oscillation [30]

$$|c_e(t)|^2 = \frac{\Omega^2}{\Omega^2 + \delta^2} \sin^2 \left(\frac{\sqrt{\Omega^2 + \delta^2}}{2} t \right) \quad (3.35)$$

where $\delta = \omega - \omega_{ge}$ is a detuning and $\tilde{\Omega} = \sqrt{\Omega^2 + \delta^2}$ is known as the generalized Rabi frequency. The Hamiltonian after applying the RWA can be written as

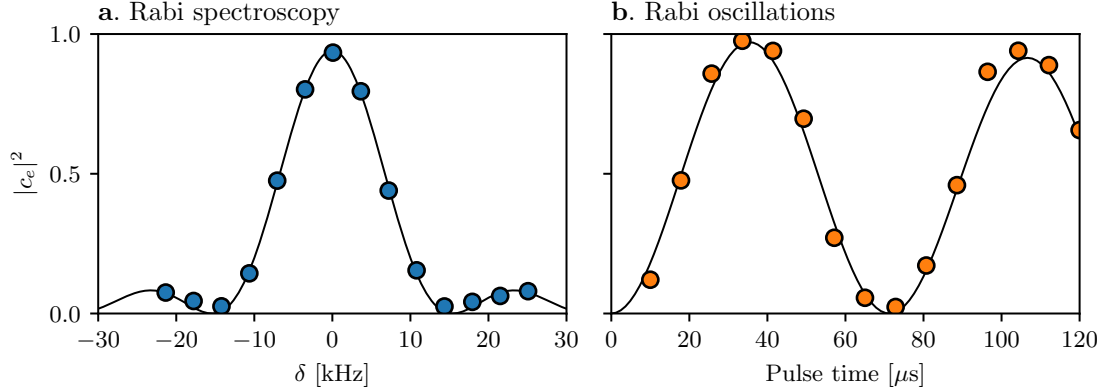


Figure 5: The Rabi cycle. Population transferred from $|F = 1, m_F = -1\rangle$ into $|F = 1, m_F = 0\rangle$ using an RF magnetic field with $\Omega = 7.1$ kHz. The markers indicate experimental data points and the lines correspond to fits to the model in Equation 3.35a. Population transferred for a $60 \mu s$ pulse as a function of detuning δ . b. Population transferred as a function of time close to resonance.

$$\hat{H}_0 = \hbar \begin{pmatrix} -\delta/2 & \Omega/2 \\ \Omega^*/2 & \delta/2 \end{pmatrix}, \quad (3.36)$$

and its eigenenergies correspond to $E_{\pm} = \pm \tilde{\Omega}/2$. Notice that the difference between the eigenenergies $E_+ - E_-$ is exactly equal to the frequency at which the populations in $|g, e\rangle$ oscillate, this will come up again in Chapter 5. Figure 5 shows an example of this process where we coupled an initial state $|g\rangle = |F = 1, m_F = -1\rangle$ to $|e\rangle =$

$|F = 1, m_F = 0\rangle$ using a radio-frequency (RF) magnetic field with $\Omega = 7.1 \text{ kHz}$.

Figure 5a shows the population in $|e\rangle$ as a function of δ for a π pulse ($\delta = 0, \Omega t = \pi$). The location of the peak in this curve is as a way to find the transition frequency (we use this method in Chapter 6). Figure 5b shows the population transferred into $m_F = 0$ from $m_F = -1$ as a function of time; we typically look at the frequency of these Rabi oscillations to calibrate the coupling strength of an effective two-level system.

3.4.2 Ramsey interferometer

Now I consider a Ramsey interferometer [31], a setup that is relevant to Chapters 6 and 8. The interaction Hamiltonian is the same as in the previous section but rather than being on continuously it is pulsed on for a time $\tau = \pi/2\Omega$ (a $\pi/2$ pulse), then the system is let to evolve only under \hat{H}_0 for a variable time t_{dark} and finally a second $\pi/2$ pulse is applied. Figure 6a illustrates this protocol: the $\pi/2$ pulses can be thought of as $\pi/2$ rotations on the Bloch sphere along \mathbf{e}_x transforming the initial state $|g\rangle \rightarrow (|g\rangle + |e\rangle)/\sqrt{2}$. During the dark time the system precesses on the equator of the Bloch sphere by an angle δt_{dark} and finally the second pulse rotates the state along the \mathbf{e}_x axis again. The probability of measuring the excited state is related to the phase accumulated during the dark time is given by

$$|c_e(2\tau + t_{\text{dark}})|^2 = \left| \frac{\Omega\tau}{2} \left[\frac{\sin(\delta\tau/2)}{\delta\tau/2} \right]^2 \cos^2 \left(\frac{\delta t_{\text{dark}}}{2} \right) \right|^2, \quad (3.37)$$

where the oscillation frequency is only determined by the detuning. In contrast, for a Rabi oscillation the detuning adds in quadrature with Ω , which suppresses the effect of the detuning when it is large as $\tilde{\Omega} \approx \Omega + \delta^2/2\Omega$. This will be important in Chapter 6 and additionally in Chapter 8 I rely on a variation of the Ramsey interferometer to perform quantum state tomography. Figure 6b shows an example of a Ramsey fringe as a function of detuning δ that we measured using two states coupled with $\Omega = 1$ kHz.

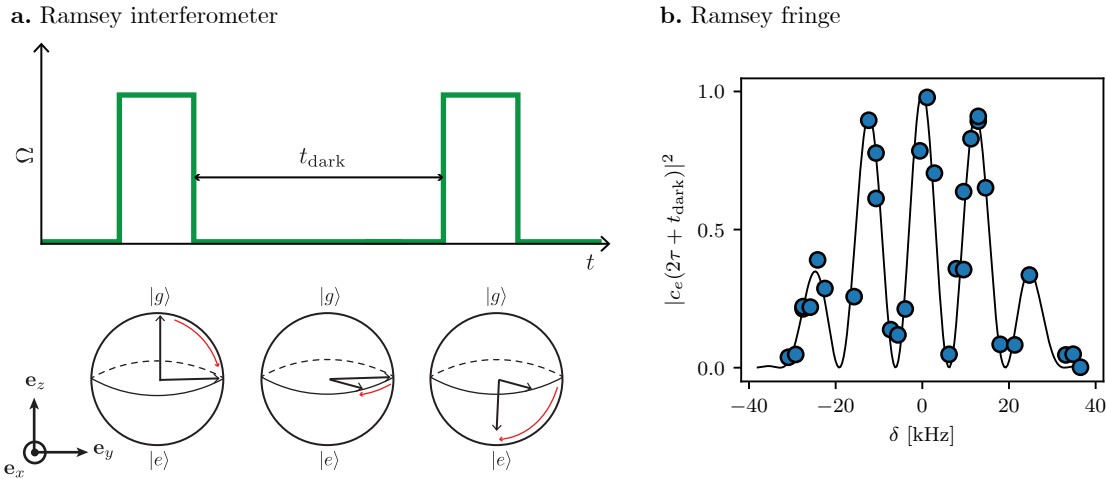


Figure 6: **a.** A Ramsey interferometer: Two $\pi/2$ pulses are separated by a time t_{dark} . The phase accumulated in the interferometer is equal to the detuning multiplied by the dark time. **b.** A Ramsey interference fringe obtained from coupling two levels using an RF field with $\Omega = 1$ kHz. We applied a pair of $\tau = 25\ \mu\text{s}$ pulses separated by a $50\ \mu\text{s}$ wait and varied the detuning by changing the bias magnetic field.

3.4.3 Floquet theory

The RWA has been used multiple times throughout this Chapter so that the Hamiltonian describing a driven systems can effectively be viewed as time independent. This approximation is valid most of the time for our experiments, however, if

we want to give a complete description of a time periodic system Floquet theory can be helpful. I will give a brief overview of Floquet theory using a matrix approach that is particularly useful for numerical computations.

Consider a time periodic Hamiltonian $\hat{H}(t) = \hat{H}(t+T)$. We can write in terms of its Fourier components

$$\hat{H}(t) = \sum_{j=-\infty}^{\infty} \exp[ij\omega t] \hat{H}_j, \quad (3.38)$$

where $\omega = 2\pi/T$ and because \hat{H} is Hermitian the operators must satisfy $\hat{H}_j = \hat{H}_{-j}^\dagger$.

The eigenstates of the Hamiltonian can be written in terms of quasi periodic functions⁶

$$|\psi_\epsilon(t)\rangle = \exp(-i\epsilon t/\hbar) \sum_{k=-\infty}^{\infty} \exp[-ik\omega t] |\psi_{\epsilon,k}\rangle \quad (3.39)$$

where the term ϵ is known as the quasi-energy. Inserting this expression into the time-dependent Schrödinger equation gives

$$\sum_k (\epsilon + \hbar\omega k) \exp[-k\omega t] |\psi_{\epsilon,k}\rangle = \sum_{j,j'} \exp[i(j-j')\omega t] \hat{H}_{j'} |\psi_{\epsilon,j}\rangle. \quad (3.40)$$

In order for the equality to be true we must have $j' - j = -k$ because the complex exponentials form an orthonormal basis and we can write

$$\epsilon |\psi_{\epsilon,k}\rangle = \sum_j \left(\hat{H}_{j-l} - \hbar\omega k \delta_{j,k} \times \hat{\mathbb{1}} \right), \quad (3.41)$$

⁶Very much like Bloch wave functions

where $\hat{\mathbb{1}}$ is the identity matrix. The expression can be recast into a matrix form

$$\epsilon \begin{pmatrix} \dots \\ |\psi_{\epsilon,-1}\rangle \\ |\psi_{\epsilon,0}\rangle \\ |\psi_{\epsilon,1}\rangle \\ \dots \end{pmatrix} = \begin{pmatrix} \hat{H}_0 + 2\hbar\omega & \hat{H}_1 & \hat{H}_2 & \dots & \dots \\ \hat{H}_{-1} & \hat{H}_0 + \hbar\omega & \hat{H}_1 & \hat{H}_2 & \dots \\ \hat{H}_{-2} & \hat{H}_{-1} & \hat{H}_0 & \hat{H}_1 & \dots \\ \dots & \hat{H}_{-2} & \hat{H}_{-1} & \hat{H}_0 - \hbar\omega & \hat{H}_1 \\ \dots & \dots & \hat{H}_{-2} & \hat{H}_{-1} & \hat{H}_0 - 2\hbar\omega \\ \vdots & & & & \end{pmatrix} \quad (3.42)$$

The quasienergies ϵ can be computed by truncating and then diagonalizing the matrix, and they are grouped into repeating manifolds separated in energy by $\hbar\omega$. The quasienergies within a manifold can be interpreted as the eigenenergies of an effective time-independent Hamiltonian \hat{H}_{Fl} that describes the evolution of the system sampled stroboscopically at an integer number of driving periods, with the time evolution operator $\hat{U}(t_0, t_0 + T) = e^{-iT\hat{H}_{Fl}}$.

Floquet theory played an important role in the engineering of different dispersion relations for atoms in Chapters 5 and 8. I will give an example based on [32], where we considered a pair of Raman beams driving transitions between the m_F states with two different frequencies $\omega_{-1,0}$ and $\omega_{0,+1}$ set to the $m_F = -1 \rightarrow m_F = 0$ and $m_F = 0 \rightarrow m_F = 1$ transitions. By performing independent RWAs with respect to each of these transitions we found that the system could be described by a

magnetic Hamiltonian

$$\hat{H} = \frac{\hbar k^2}{2m} + \boldsymbol{\Omega}(x) \cdot \hat{\mathbf{F}} + \Omega_2 \hat{F}_{zz}^{(2)} \quad (3.43)$$

with $\boldsymbol{\Omega}_1(x)/\Omega_1 = \cos(2k_R x)\mathbf{e}_x - \sin(2k_R x)\mathbf{e}_y$, $\hat{F}_{zz}^{(2)}\hbar = \hat{F}_z^2/\hbar^2 - 2/3$ is an element of the quadrupole tensor and $\Omega_2 = (\omega_{-1,0} - \omega_{0,1})/2$ can be interpreted as an effective quadratic Zeeman shift. The competing contributions between kinetic and magnetic ordering energies gave rise to different magnetic phases. Figure 7a. shows the ground branch of the dispersion relation for small $\Omega_1 < 4E_L$ (top) and large $\Omega_1 > 4E_L$ (bottom). As the value of Ω_2 is decreased the magnetization in the system changes as the location of the global minima in the dispersion changes. The experimental parameters Ω_1 and Ω_2 spanned a two-dimensional phase diagram shown in Figure 3.43b that we experimentally mapped. The eigenenergies of Equation 7 are plotted in Figure 7c. However in order to get a good agreement between the experiment and the phase diagram we had use the full Floquet Hamiltonian which results in having modified parameters in Equation 3.43 $\Omega_2^{(\text{eff})} = \Omega_2 + \mathcal{O}(\Omega_1^2/\epsilon)$ (red dotted line in Figure 7b). Figure 7d shows three manifolds of Floquet quasienergies for this system, illustrating their periodic nature.

3.5 Detection: Resonant absorption imaging

Ultracold atom experiments rely on optical imaging as the main method to probe and characterize the system. In our lab we use resonant absorption imaging which uses a resonant probing laser that is shone at the atomic cloud and then im-

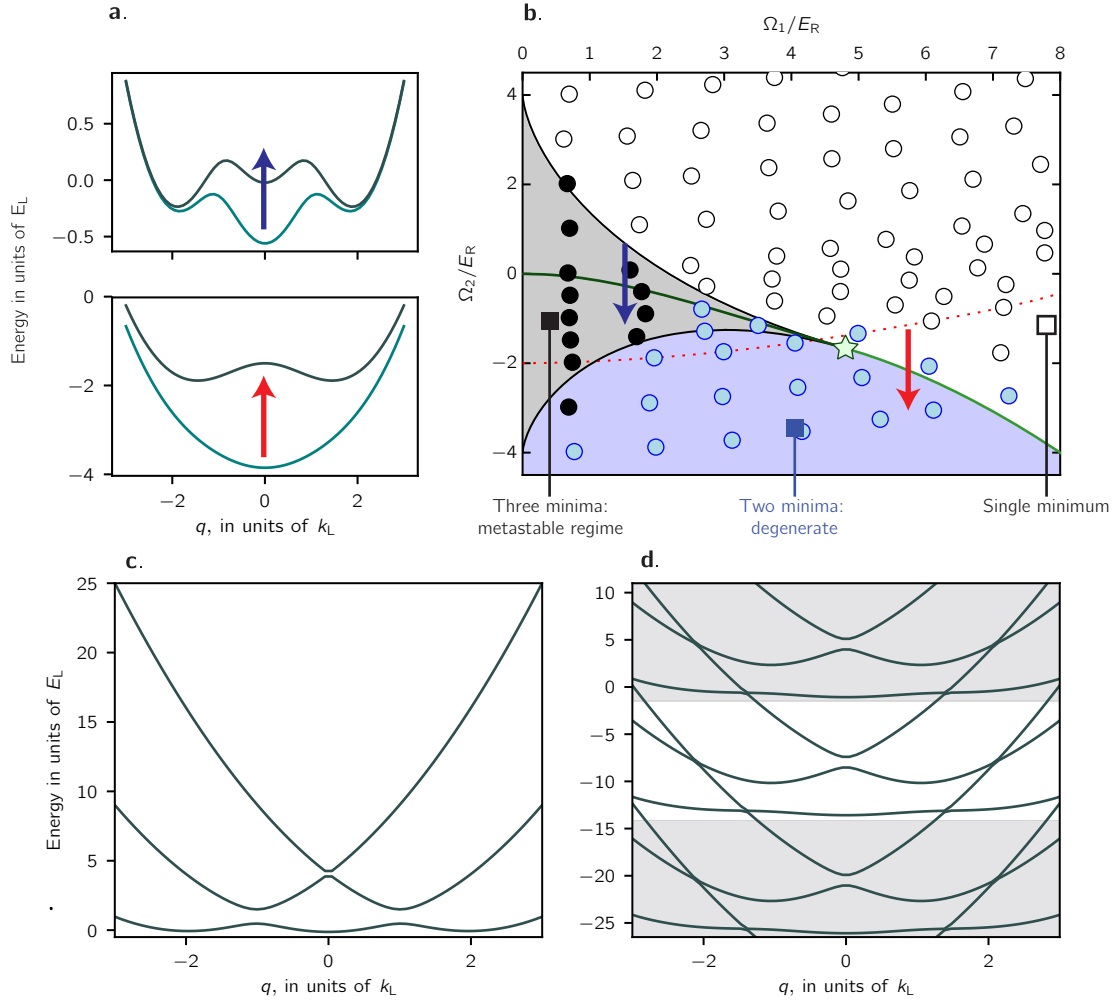


Figure 7: Magnetic phases of a spin-1 SOC system. **a.** Ground state energies of a spin-1 SOC system for $\Omega_1 = 1.5 E_L$ (top) and $\Omega_2 = 1.5 E_L$ (bottom). By changing Ω_2 we moved the location of the central minima. **b.** Phase diagram of a spin-1 SOC system. They green line corresponds to a line of phase transitions where the system goes from magnetized to unmagnetized. **c.** Dispersion relation computed for $\Omega_1 = 2 E_L$, $\Omega_2 = 0$. **d.** Floquet quasienergy dispersion relation for the same parameters. The magnitude of Ω_1 effectively modifies Ω_2 in the RWA Hamiltonian.

aged into a charged-coupled device (CCD) camera. From the absorption of the light we can then infer properties about the atoms such as number of atoms, temperature, integrated column density and momentum distribution if we allow the clouds to expand.

Consider a laser beam with intensity $I(x, y, z)$ and angular frequency ω propagating along \mathbf{e}_z through a cloud of atoms with density $n(x, y, z)$ as is shown in Figure 8a. We define a (frequency dependent) scattering cross section $\sigma(\omega)$ which characterized the probability of an atom absorbing a probe photon and is given by the Lorentzian function

$$\sigma(\omega) = 3A_{eg} \frac{\pi^2 c^2}{\omega_0^2} \frac{1}{2\pi} \frac{\Gamma}{\delta^2 + \Gamma^2/4} \quad (3.44)$$

plotted in Figure 8b, where Γ is the scattering rate, ω_0 is the transition frequency, $\delta = \omega - \omega_0$ is the detuning and A_{eg} is the Einstein coefficient associated to spontaneous emission. As the beam travels through the cloud it will be absorbed and its intensity is reduced at a rate given by

$$\frac{dI}{dz}(x, y, z) = -n(x, y, z)\sigma(\omega)I(x, y, z). \quad (3.45)$$

In the limit of small intensities we can integrate this expression over the thickness of the cloud and find that the intensity decays exponentially with the density and the scattering cross section

$$I(x, y, z) = I(x, y, 0)e^{-\int_0^z n(x, y, z')\sigma(\omega)dz'}, \quad (3.46)$$

where $\text{OD} = \int_0^z n(x, y, z')\sigma(\omega)dz'$ is the optical depth (OD) of the medium. If we measure the OD of the cloud it is then straightforward to obtain the integrated

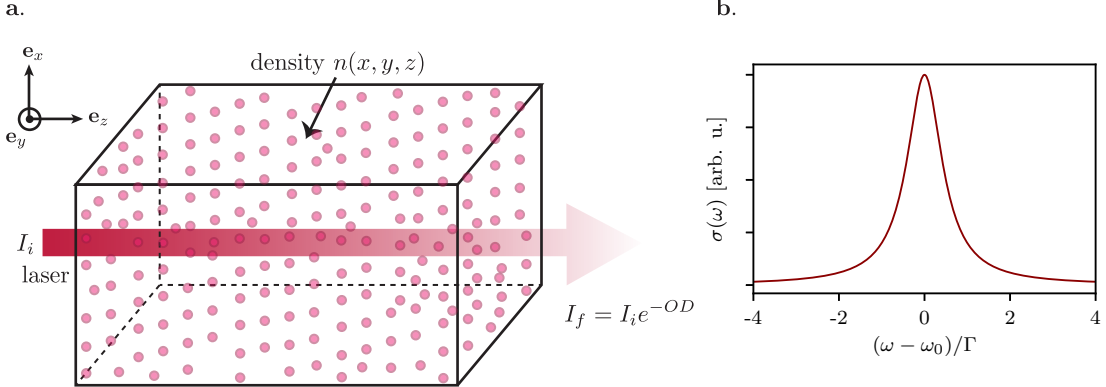


Figure 8: **a.** A laser beam traveling along e_z through a medium with density $n(x, y, z)$. The intensity decays exponentially with the integrated column density and the scattering cross section $\sigma\omega$. **b.** The scattering cross section has a Lorentzian line shape with a full width half maximum equal to Γ . [TODO: add real data on panel b if I have time.]

column density $n(x, y)$. This result, known as the Beer-Lambert law, works well when using low intensity beams.

In the experiment we measure the optical depth of a cloud by imaging the probe into a CCD camera under two different conditions: first in the presence of atoms to measure the attenuated intensity $I_f = I(x, y, z)$ and then without any atoms to get a measure of the initial intensity $I_i = I(x, y, 0)$. The optical depth can then be computed as

$$OD = \ln \left(\frac{I_f}{I_i} \right). \quad (3.47)$$

Figure 9 show the different images used to compute the OD. In practice we take a third image of the background intensity I_{bg} and subtract it from the other two images.

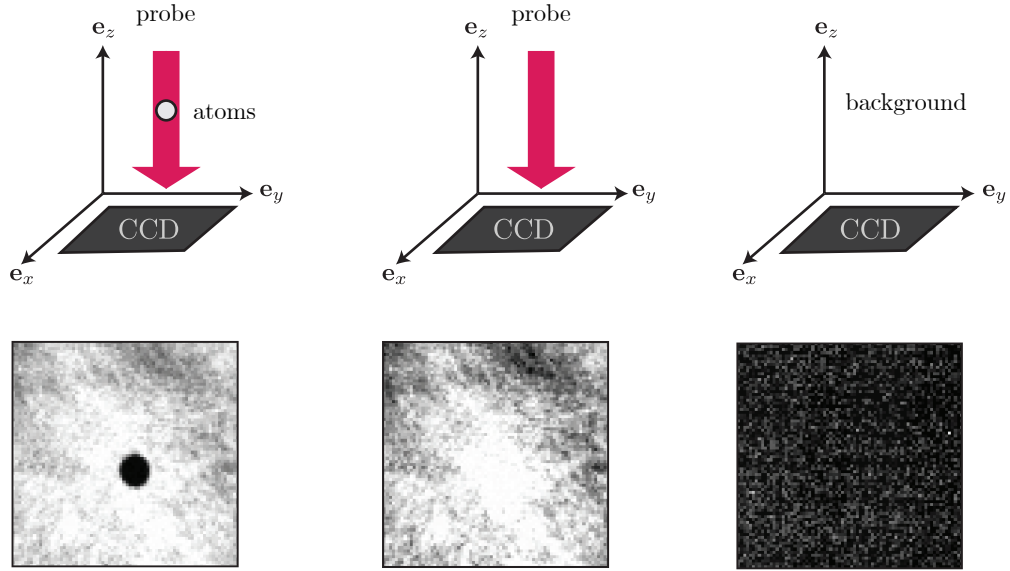


Figure 9: Resonant absorption imaging. An atomic sample is illuminated with a resonant probe whose intensity is later recorded on a CCD camera. Two additional images of the unabsorbed probe intensity and the background intensity are captured in order to reconstruct the optical density of the atoms.

3.5.1 High intensity absorption imaging

The use of the OD to infer the atomic density works well if we assume that the intensity of the probing laser is low such that the atoms mostly stay in the ground state. However at high intensities a significant fraction of the atoms can become excited and effects such as stimulated emission of light have to be taken into account. As a result of this the scattering cross section gets an additional dependence on intensity (see [33] for a complete derivation)

$$\sigma(\omega, I) = \sigma(\omega) \frac{1}{1 + I/I_{\text{sat}}}, \quad (3.48)$$

where $I_{\text{sat}} = \pi hc\Gamma/3\lambda_0^3$ is the saturation intensity, and when $I = I_{\text{sat}}$ the population in the ground and excited state are equal. Integrating Equation 3.45 using the modified expression for $\sigma(\omega, I)$ gives

$$n(x, y)\sigma(\omega) = -\alpha^* \ln(I_f/I_i) + \frac{I_i - I_f}{I_{\text{sat}}}, \quad (3.49)$$

where I have also added an additional dimensionless parameter α^* which can account for imperfections in the imaging process (see [34]).

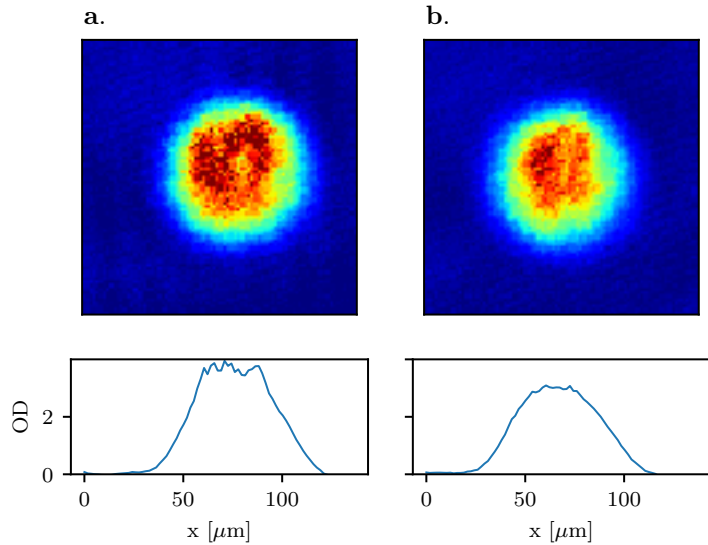


Figure 10: **a.** A BEC imaged at low intensity shows a ‘flat-top’ density profile. **b.** In order to recover the Thomas-Fermi profile it is necessary to image high density BECs with intensities larger than I_{sat} .

It is hard reliably measure atomic clouds at low intensity when the OD is of the order of 3 or 4 (such as our BECs) and a significant fraction of the imaging light is absorbed. Due to the limited dynamic range of CCD cameras the measured OD saturates, resulting for example in imaging ‘flat-top’ BECs rather than the

usual Thomas-Fermi distribution as shown in Figure 10. To get around this issue we typically image with using intensities $I > I_{\text{sat}}$. In order to correctly compute the column density including saturation effects we need a conversion of I_{sat} from mW/cm² to counts per pixel on the CCD camera. We follow the procedure described in [34] find the values of α^* and I_{sat} in counts per pixel. To learn about other effects such as the recoil momentum from the imaging light that could affect absorption images see [35].

Chapter 4: Making BECs in the Rubidium Lithium apparatus

All the experiments presented in this thesis were performed at the Rubidium-Lithium (RbLi) apparatus at the University of Maryland. The apparatus was designed to produce mixtures of quantum degenerate gases of bosons and fermions. The original plan was abandoned because the cross-species scattering length was found to be repulsive and small ($a_s \approx 20 a_B$) [36] and the nearest Feshbach resonance was measured to occur at the unexpectedly large magnetic field of 1066 G [37]. All our experiments were performed using only ^{87}Rb instead.

The RbLi apparatus is scheduled to be shut down and the construction of a new dual-species apparatus for ^{87}Rb and K^{39} is underway. The RbLi apparatus has been thoroughly described in [15, 16]. Here I only give a brief overview of the apparatus. Additionally I discuss in detail new elements that have been added to the setup and changes that have been implemented and were not previously reported. In Appendix A I discuss the best and the worst aspects of the apparatus.

This Chapter is divided into three sections. In Section 4.1 I give a brief overview of the RbLi apparatus and describe its basic capabilities. In Section 4.2 I describe the experimental sequence used to produce BECs. Finally in Section 4.3 I describe changes and to the RbLi apparatus that have not been reported on previous

theses.

4.1 Overview of the RbLi apparatus

The RbLi apparatus is divided into two optical tables. One table contains laser systems that fiber coupled into the main optical table, shown in Figure 1, containing a vacuum system where atoms are cooled to degeneracy. The vacuum system can be divided into three regions: an oven Region where Rb and Li atoms are heated up, a Zeeman slower that acts as a differential pumping stage and an ultra-high vacuum (UHV) region with a glass cell where all the experiments are performed.

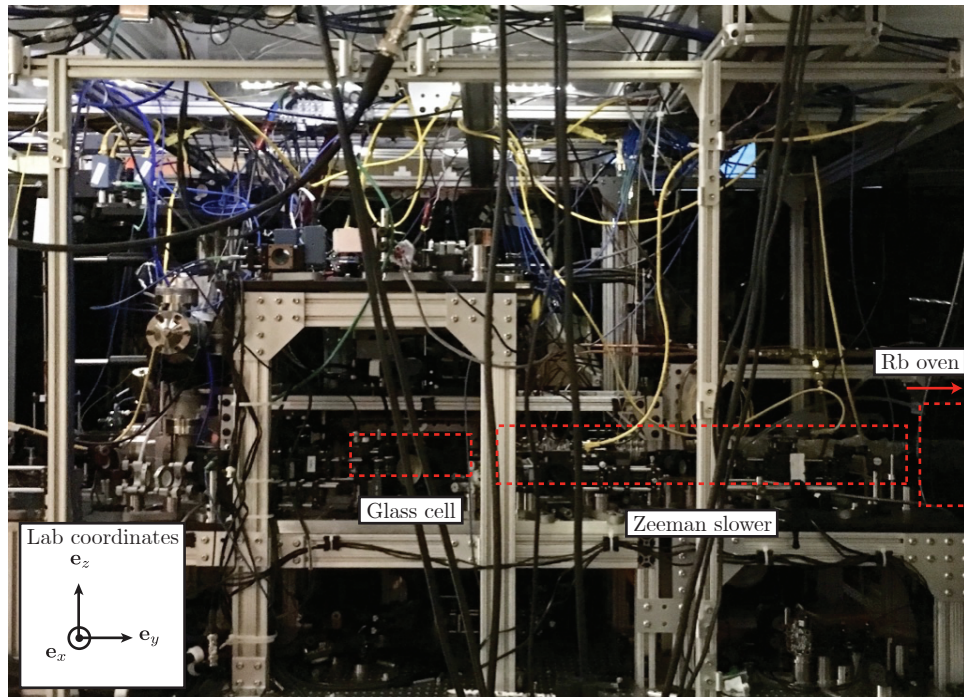


Figure 1: The vacuum system of the RbLi apparatus is divided into an oven, a Zeeman slower and an UHV region containing a glass-cell where all experiments are performed.

4.1.1 Laser systems

We use a total of three lasers to perform laser cooling and imaging of atoms: a cooling laser that addresses the $F = 2 \rightarrow F' = 3$ transition, a repump laser that takes atoms that have decayed into the $F = 1$ state back to $F = 2$ via the $F' = 1$ state and a master laser that provides a frequency reference for both lasers. The frequency of master laser is locked using saturation absorption spectroscopy to the $F = 3 \rightarrow F' = 3$ and $F = 3 \rightarrow F' = 4$ crossover of the D2 line of ^{85}Rb . The repump and coolong light is split into a beam used for laser cooling in the Zeeman slower and six beams used to create a magneto-optical trap (MOT). The frequencies of each laser with respect to the master laser frequency as well as the frequencies with respect to the transitions in ^{87}Rb can be visualized in Figure 2.

We have two additional lasers that are used to generate potentials for the atoms. The first one is a 30 W 1064 nm IPG Photonics laser located at the main experiment table and that we use to make a cross dipole trap for the atoms. The two dipole beams come from the zeroth and first order of an acusto optic modulator (AOM) and the beams propagate along the $\mathbf{e}_x + \mathbf{e}_y$ and $\mathbf{e}_x - \mathbf{e}_y$ direction (thee lab coordinate system is shown in Figure 1. The other laser system is a Ti:Sapphire laser used to generate Raman transitions and will be described in more detail in Section 4.3.2. Figure 3 shows a simplified diagram with a bird's-eye view and a side view of the apparatus that show all the lasers that are used for cooling, trapping, Raman coupling and imaging.

We can detect atoms using two different imaging systems. The first one is

used primarily for diagnostics and it images the yz plane of the atoms from the $+e_x$ side of the glass cell. The second system looks at the xy plane from below the glass cell and is the main system used for data acquisition.

4.1.2 Magnetic field control

The precise control of magnetic fields is essential during the multiple stages in our experimental sequence. We use multiple coils in our experiment as is illustrated in Figure 4. Three pairs of Helmholtz coils in the vicinity of the glass cell generate bias magnetic fields $\mathbf{B} = (B_x, B_y, B_z)$ along e_x , e_y and e_z . Once BECs are produced we typically use bias fields along e_z to change the Zeeman energy of the different m_F states. One pair of anti-Helmholtz coils generates a strong quadrupole magnetic field along e_z that is used in the MOT, for magnetic trapping and to separate the different m_F states in time of flight (Stern-Gerlach). An additional set of coils arranged in a ‘clover leaf’ pattern generates small gradients along e_z , $e_x + e_y$ and $e_z - e_y$ which allow us to cancel stray magnetic gradients in B_z near the atoms.

The experiment also has the capability of producing oscillatory magnetic fields. A set of coils on a printed circuit board (PCB) produce linearly polarized radio-frequency (RF) magnetic fields either in the e_y or e_z direction that are used for RF induced evaporation and to drive transitions between m_F states. There is an additional setup for producing high-power RF fields with will be described in more detail in Section 4.3.3.

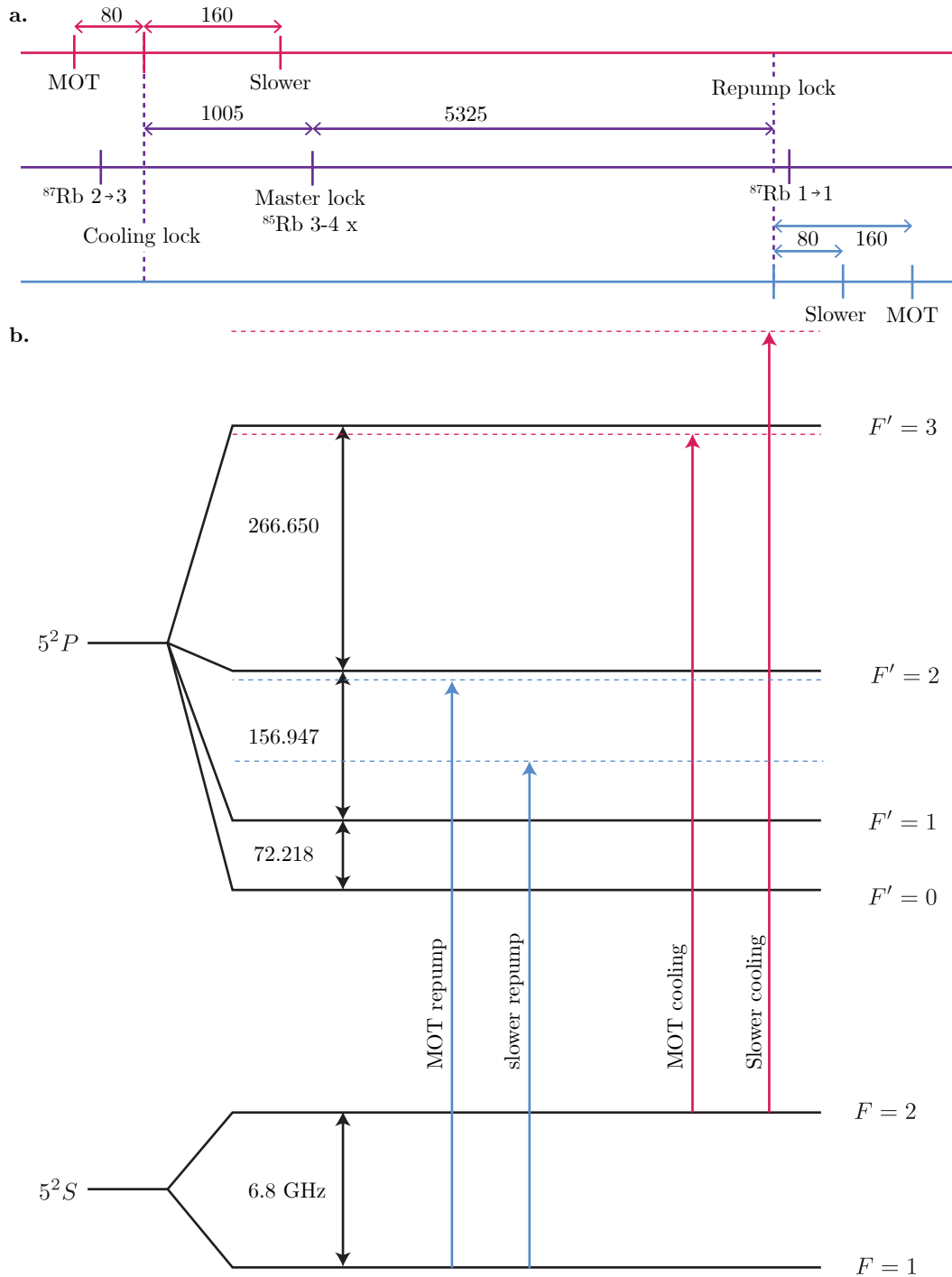


Figure 2: **a.** Cooling and repump frequencies relative to the master laser lock. **b.** Cooling and repump frequencies relative to the ^{87}Rb D2 line transitions.

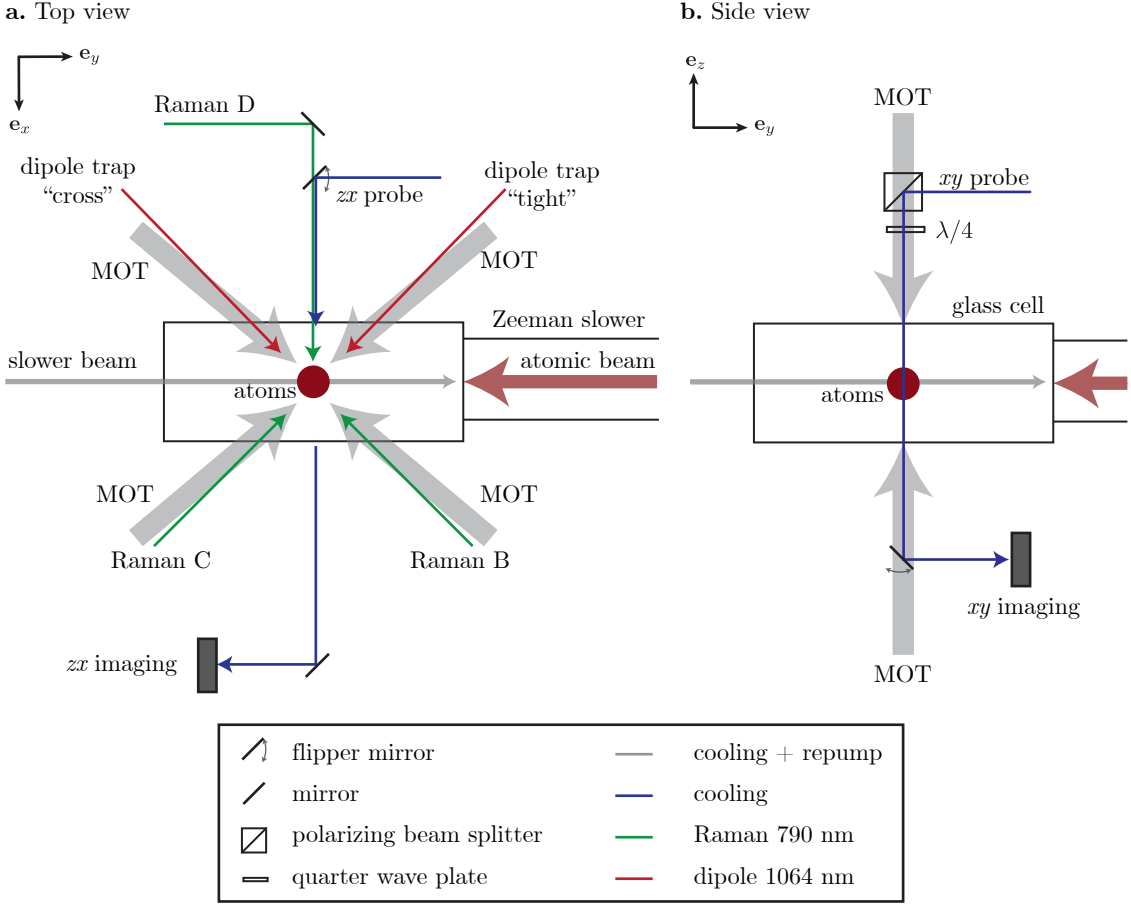


Figure 3: Diagram of the RbLi apparatus as seen from **a.** the top and **b.** the side.

4.2 Experimental sequence to make BECs

The production of BECs starts in an oven where Rb atoms are heated to 120 C to produce an atomic beam. The Rb atoms come from the same 5 g ampule that was installed when the apparatus was first built almost 10 years ago. The atoms then travel down a Zeeman slower [38] where they are laser cooled and then captured in a MOT. For the MOT we apply a 5.5 A current to the quadrupole coils corresponding to a 15.62 G/cm gradient. The cooling light is blue detuned by 18 MHz $\sim -3\Gamma$ from

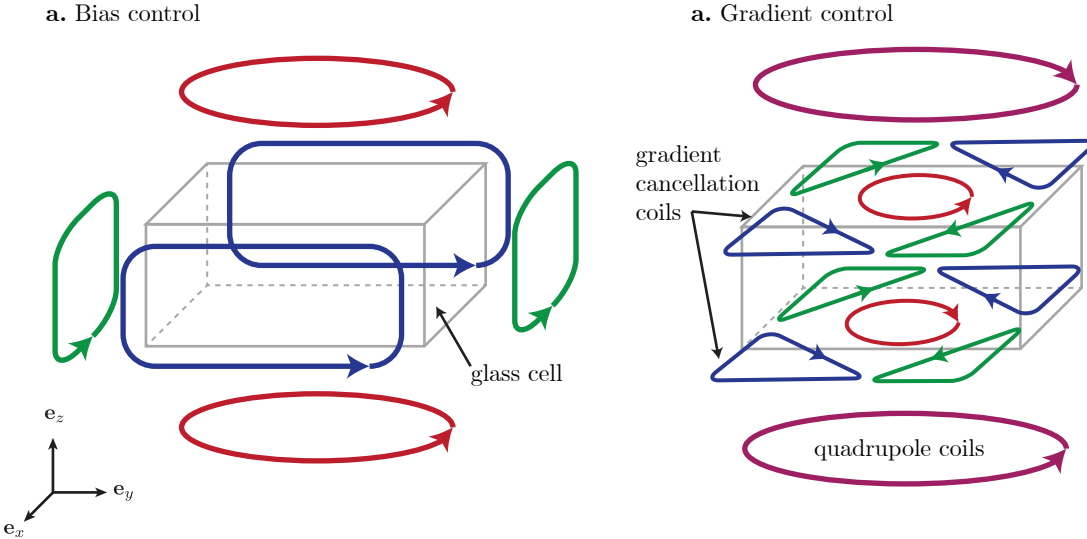


Figure 4: Magnetic coil geometry in the RbLi apparatus. **a.** We use three pairs of Helmholtz coils to produce bias fields along \mathbf{e}_x , \mathbf{e}_y and \mathbf{e}_z . **b.** We have a pair of coils that produce strong quadrupole magnetic fields for the MOT and magnetic trapping. Additionally we have a pair of ‘clover-leaf’ coils to control the gradients in B_z .

the $F = 2 \rightarrow F' = 3$ cycling transition and the repump light is 16 MHz below the $F = 1 \rightarrow F' = 2$ transition. We typically load the MOT for times between 1 – 5 s before we turn off the Zeeman slower currents and laser beams. In preparation for the molasses stage we do a 30 ms decompression stage where we ramp down the gradient to 10 G/cm and reduce the repump power.

The next step is to perform polarization gradient cooling in optical molasses where the polarization gradient from interfering counter propagating lasers further cools the atoms [39]. For this we completely switch off the quadrupole coils and adjust the bias fields in all three directions so that they are zero at the atoms. During this stage the repump power is kept low and the frequency of the cooling light is decreased to 140 MHz below the MOT frequency for 10 ms. We then completely

turn off the MOT repump light to allow atoms to decay into the $F = 1$ manifold and use a small amount of slower repump light to optically pump atoms into the $|F = 1, m_F = -1\rangle$ magnetically trappable state for a total of 1.5 ms.

Once the atoms are successfully pumped into $|F = 1, m_F = -1\rangle$ we capture them in a magnetic trap with a gradient of 62 G/cm and compress them by increasing the current in the coils until we reach a gradient of 160 G/cm in 300 ms. In the magnetic trap we perform RF induced evaporation by turning on an RF field polarized along \mathbf{e}_y with frequency of 24 MHz, which transfers the hotter atoms at the edges of the trap into the $m_F = 0$ state which is not magnetically trappable. We then perform an exponential ramp from the initial frequency to a final frequency of 4.5 MHz in 1 s.

For the final stage of evaporative cooling we transfer the atoms from the magnetic trap into an optical dipole trap. We start by turning on only the ‘tight’ arm of the trap at full power (about 11 W) and slowly decompressing the quadrupole trap to 45 G/cm in 1.5 s. We then turn on the second ‘cross’ beam in 1 s; splitting the power so that there the power split between the tight and cross beams is about 70–30%. As the cross dipole beam is being turned on we ramp the quadrupole field further down to 14 G/cm, slightly above the value necessary for the trap to suspend atoms against gravity. We simultaneously shift the bias field along \mathbf{e}_z to align the center of the quadrupole trap to the dipole trap.

We evaporate the atoms in the dipole trap in two stages. First we exponentially ramp down the power to about 20% of its initial power in 1.5 s (time constant = 0.5 s). Before the final evaporation stage we completely turn off the quadrupole trap

in 1 s. Finally, we perform a second exponential ramp where the power is dropped to about 30% of the intermediate power in 2 s (time constant = 1 s. The slow ramps ensure that there is enough time for the atoms to thermalize as they evaporate. During the second evaporation stage the atoms reach the critical temperature for Bose-Einstein condensation and we are able to produce BECs with about 4×10^4 atoms in the $|F = 1, m_F = -1\rangle$ state. At this point we can prepare different m_F states and set the Zeeman splitting between levels using the techniques described in the following sections.

4.2.1 Adiabatic rapid passage

[Consider moving these two subsections to the previous Chapter...]

We prepare different m_F states within the $F = 1$ manifold using an adiabatic rapid¹ passage protocol (ARP) which is based on the Landau-Zener model [40]. The technique relies on preparing dressed states; eigenstates of the atomic Hamiltonian with an oscillatory field magnetic field (RF or microwaves for our experiments). To perform ARP with RF we set the frequency of the field ω_{RF} so that it matches the Zeeman splitting between the $m_F = -1$ and $m_F = 0$ states for a target bias field $B_0 \mathbf{e}_z$.

We start with atoms in $m_F = -1$ and at a bias field $B_i \approx B_0 - 380 \text{ mG}$ ($\delta \approx 30 \text{ kHz}$). We ramp an $\Omega = 20 \text{ kHz}$ RF field and angular frequency ω_{RF} in 50 ms, effectively mapping atoms in the $m_f = -1$ state into the ground state of the RF Hamiltonian as shown in Figure 4.2.1a. We then sweep the detuning by linearly

¹Rapid with respect to the spontaneous emission rate of the excited state being coupled.

changing the bias field. As the detuning is changed, the state decomposition of the ground state is modified and as long as the rate of change in detuning is small compared to Ω_{RF}^2 (or small compared to the gap in Figure 4.2.1a) the system will adiabatically follow the ground state. After the detuning sweep the RF field is abruptly turned off, projecting the RF eigenstates into the m_F states. In Figure 4.2.1 we set $\omega_{\text{RF}} = 23$ MHz and when the Zeeman splitting between $m_F = -1$ and $m_F = 0$ is equal to ω_{RF} we observe an equal superposition of both states and if the detuning is swept beyond resonance we can reliably prepare the $m_F = 0$ state. In general it is necessary to look at the eigenstates of the three-level RF Hamiltonian

$$\hat{H}_{\text{RF}} = \begin{pmatrix} -\delta & \Omega_{\text{RF}}/2 & 0 \\ \Omega_{\text{RF}}/2 & -\epsilon & \Omega_{\text{RF}}/2 \\ 0 & \Omega_{\text{RF}}/2 & \delta \end{pmatrix}, \quad (4.1)$$

but for large quadratic Zeeman shifts as is usually the case in our experiments we can only look at an effective two-level system.

In order to keep the bias fields as stable as possible we also synchronize the timing of our experiments to the 60 Hz line; this step is performed in different stages of the experiment but perhaps were we have noted it has the biggest impact is right before ARP. For additional magnetic field control and stabilization we use a technique using microwave assisted partial transfer absorption imaging described in the following section.

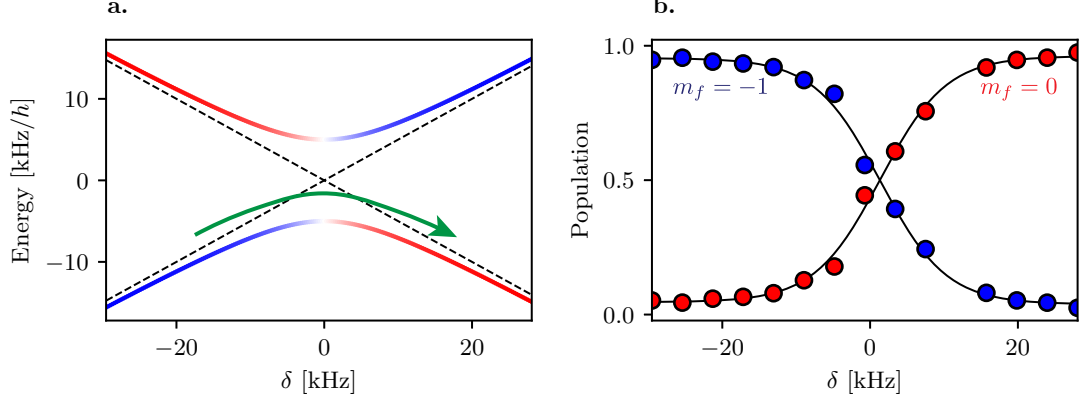


Figure 5: **a.** Eigenenergies and eigenstate decomposition of an RF dressed Hamiltonian for a two-level system (Equation 3.36) with $\Omega = 10$ as a function of detuning. The eigenstates are linear combinations of $m_F = -1$ and $m_F = 0$ (red and blue respectively). **b.** Population in the m_F states for different values of detuning

4.2.2 Magnetic field stabilization with microwave assisted partial transfer absorption imaging

Our experiments are very sensitive to changes in the environmental magnetic field. In the past we used flux gate sensors (**Stefan-Mayer** model FL1-100 f) in the apparatus to feedback and stabilize the magnetic field (see [16]). These sensors are a useful tool, however due to space constraints we were not able to measure the fields close to the atoms and additionally the range of magnetic fields that they operate at is small (only 1 G, we typically operate at $B > 10$ G). We built a 6.8 GHz microwave system (see Section 4.3.4) so that we could use the atoms themselves as sensors of magnetic field.

The method relies in transferring a small fraction of atoms into the $F = 2$ manifold where they can be imaged without the use of repump light and therefore

minimally disturbing the remaining atoms in $F = 1$. We apply two microwave pulses for a total time τ with frequency $\omega_0 - \delta_{\pm}$ where $\delta_{\pm} = \pm 1/(2\tau)$. We typically set ω_0 equal to the Zeeman splitting between the $|F = 1, m_f = -1\rangle$ and $|F = 2, m_f = -2\rangle$ states and we set the coupling strength $\Omega_0 \ll 1/\tau$ such that only about 5% of the atoms are transferred by each pulse. We image the transferred atoms following each pulse using absorption imaging and from the measured densities we calculate the imbalance

$$n_{\text{imb}} = \frac{n(\delta_+) - n(\delta_-)}{n(\delta_+) + n(\delta_-)} \quad (4.2)$$

which gives us a signal that is both insensitive to fluctuations in the number of

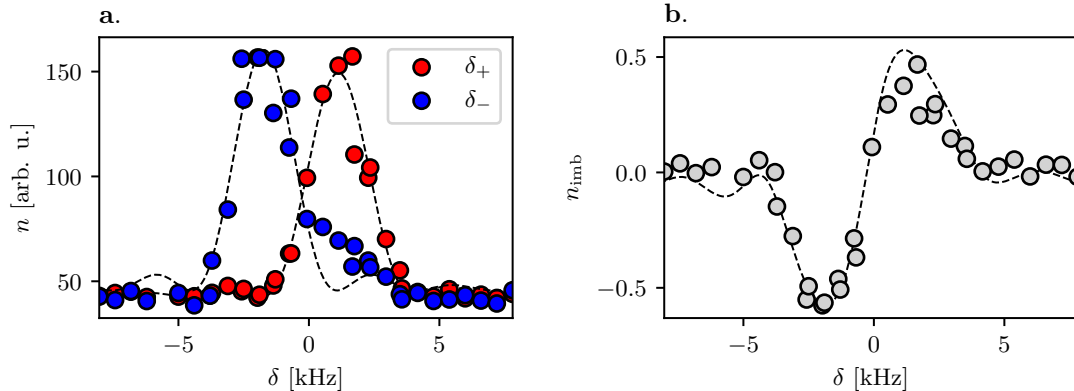


Figure 6: Magnetic field stabilization using microwave assisted PTAI. **a.** Population transferred into $|F = 2, m_F = -1\rangle$ from $|F = 1, m_F = -1\rangle$ as a function of bias magnetic field (global detuning δ). Each microwave pulse was $\tau = 250 \mu\text{s}$ and detuned by $\delta_{\pm} = \pm 1/(2\tau)$ transfer a small fraction of atoms from $|F = 1, m_F = -1\rangle$ into $|F = 2, m_F = -1\rangle$. **b.** Error signal calculated using the transferred atoms by each pulse. We lock the magnetic field to the $\sim 5 \text{ kHz}$ ($\sim 7 \text{ mG}$) wide linear portion of the signal.

atoms and linearly sensitive to changes in magnetic field². We use this error signal

²A single pulse on resonance is quadratically sensitive to detuning (see Equation 3.35)

both to monitor the magnetic field before performing experiments and cancel long term drifts in the field. In most cases, we chose the states $|F = 1, m_F = -1\rangle$ and $|F = 2, m_F = -2\rangle$ as their relative energies are the most sensitive to changes in magnetic field. Figure 6a shows the transferred atoms by each microwave pulse for different values of bias magnetic field and Figure 6b shows the imbalance. The microwave frequency ω_0 is on resonance with the $|F = 1, m_F = -1\rangle \rightarrow |F = 2, m_F = -2\rangle$ transition when both pulses transfer the same number of atoms.

In [41] we studied partial transfer absorption imaging as minimally destructive technique for imaging ultracold atoms. See Chapter 6 for an alternative solution for dealing with magnetic field noise.

4.3 Upgrades to the RbLi Machine

4.3.1 Master laser system

Previously we used a **New Focus Vortex II TLB-6900** extended cavity diode laser as our master laser and a home made saturation spectroscopy setup using a Rb glass cell (see [15, 16]). The frequency of this laser was not very stable and the laser would constantly get out of lock. We replaced the old master laser with a **Vescent photonics DBR Laser Module System** which uses a distributed Bragg reflector laser diode with no external cavity and is therefore very mechanically stable. The frequency of the laser is stabilized and controlled using the **D2-210** spectroscopy module and **D2-125** laser servo. The master laser system is considerably simplified as can be seen in Figure 7.

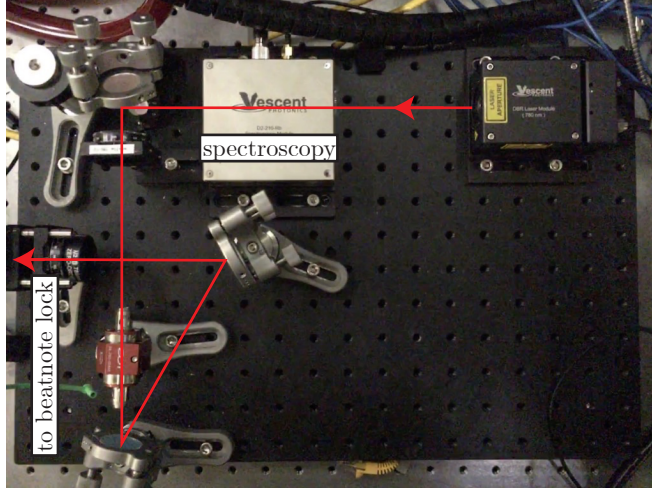


Figure 7: Master laser system. We replaced the old Vortex II laser with a Vescent photonics DBR Laser Module System that is considerably more stable.

4.3.2 Raman laser system

The RbLi apparatus has a laser system with wavelength close to 790 nm that is used to generate Raman induced transitions and spin-dependent potentials (see Section 3.3.2). The original Raman laser system consisted of a **Toptica DL Pro** laser seeding a tapered amplifier mounted on a homemade copper holder. This laser system was replaced by an M squared Ti:Sapphire laser (**SolsTiS-400-SRX-F**) that is pumped by a 532 nm **IPG GLR30** laser. We typically operate the pump laser at 14.5 W, a fraction of this light is redirected into the path of a 1D optical lattice and the remaining power is used to pump the Ti:Sahprie laser. We switched to using a Ti:Sapph laser because of its wide range of tunable wavelengths in the near infrared (725 – 875 nm) and its high power output. Figure 8 shows the typical dependence of the Ti:Sapph output power as a function of pump power.

The output of the laser is split into 3 different Raman beams. The frequency

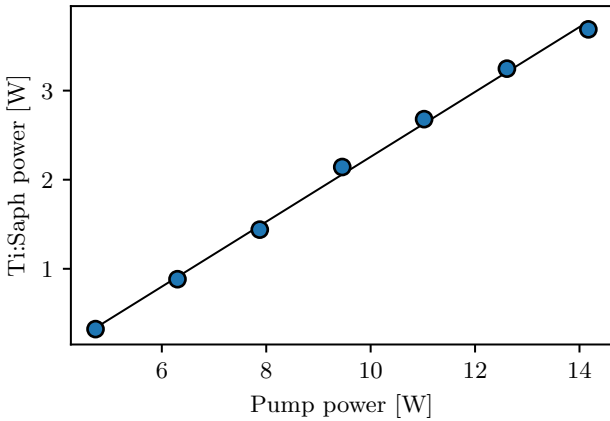


Figure 8: Ti:Sapphire laser output as a function of pump power. This data was taken when the laser was being setup for the first time. The alignment of the laser cavity was optimized to produce maximum power at 15 W pump power. The output power is proportional to the pump power $P_{\text{out}} \approx 0.364P_{\text{pump}}$.

and power of each beam is independently controlled using **IntraAction ATM-801A2** AOMs centered at 80 MHz. We drive the AOMs using homemade drivers made from the **Minicircuits** components listed in Table 4.1 and **Novatech Model 409B** direct digital synthesizer (DDS) to generate an RF signal at the desired frequency. The components are arranged as is shown in Figure 10: we control the amplitude of the RF signal using a mixer connected to a DC signal and the switch can turn off the signal in less than 1 μ s using a TTL signal. We fiber couple the light using single mode optical fibers (non-polarization maintaining) with FC/APC type connectors at the input (laser side) and FC/PC at the output (experiment side). We made this choice so to implement a phase lock that would cancel phase noise added by the fibers. The idea behind this method is that a small fraction of the fiber coupled light is reflected at the flat cut edge of the optical fiber and coupled back where it can be heterodyne probed with the input light (see Figure 9), our implementation

described in Section 3.6.3 of [42]. We control the polarization of the light using polarization controlling paddles (Thorlabs FPC030 and Thorlabs FPC560) which produce a controllable amount of stress in the fibers that changes their birefringence, a method that we have found to be much more stable than using polarization-maintaining fibers even when the polarization of the light is properly aligned to the fiber slow/fast axis. None of the experiments presented in this thesis used the phase lock but the experiments described in Chapter 8 were performed using the new Raman laser system. Figure 9 shows a diagram of the Raman optics as well as the 532 nm optical lattice optics which are shared on the same breadboard.

Table 4.1: List of AOM driver components

Part number	Description
ZHL-1-2W	2 W amplifier
ZAD-3+	Mixer
ZYSWA-2-50DR	Digital switch

4.3.3 High power RF system

The experiments described in Chapters 6 and 8 required the use of high power RF magnetic fields to achieve coupling strengths at the atoms $\Omega \sim 100 - 200$ kHz. To do so we built a resonant circuit with a coil close to the atoms. After multiple attempts to build a resonant coil either on a PCB (similar to the coil used for RF induced evaporation, see [15, 16]) or winding some wires with the right dimensions we found that the product that worked best for our needs was a wireless power charging receiver coil (Würth Elektronik Digikey part number 732-5646-ND) shown in the

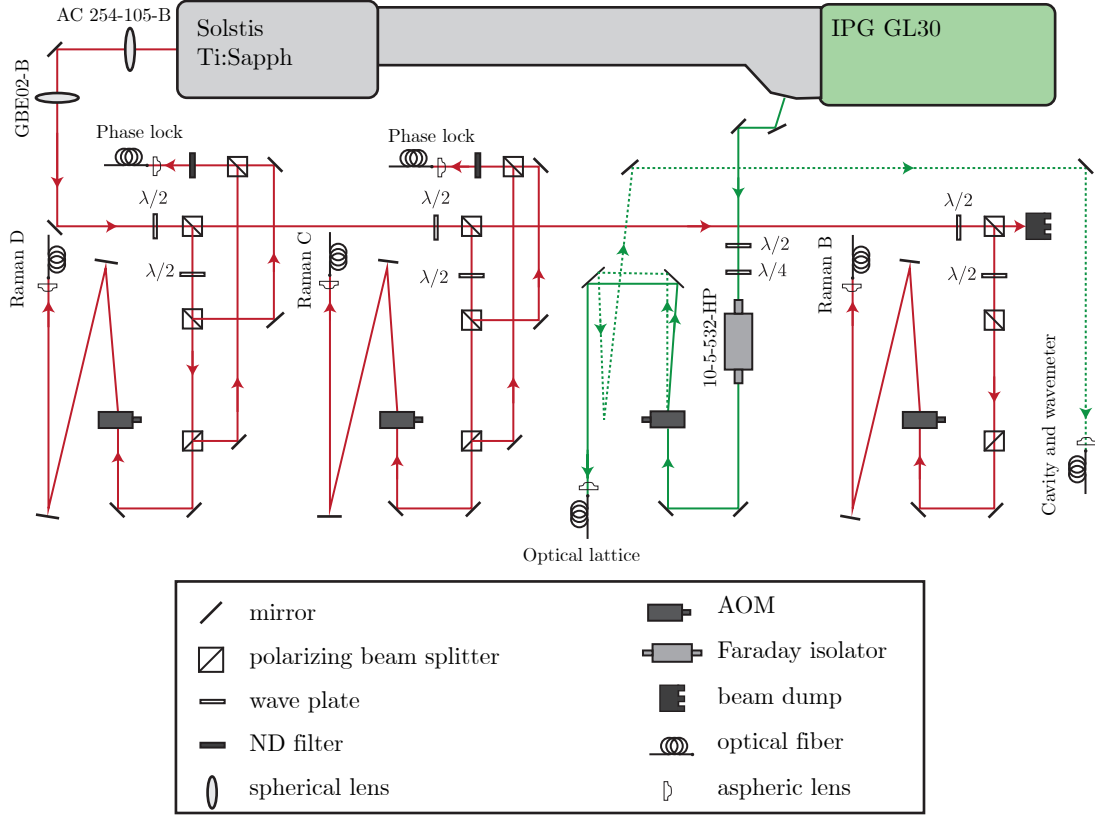


Figure 9: Optical layout of Raman and optical lattice lasers. The Ti:Sapphire laser provides tunable infrared light that we use for three different Raman beams. The beams labeled as ‘Raman C’ and ‘Raman D’ can be phase stabilized. A small fraction of the green pump laser is used to produce a blue-detuned 1D optical lattice.

bottom panel of Figure 4.3.3a. The coil has a self resonant frequency at 22 MHz and a Q-Factor of 45. It has an inner diameter of 1.62 cm and an outer diameter of 2.8 cm, just the right size for us to place it snugly next to the glass cell (on the $-e_x$ side) with minimal perturbations to the laser beams in its vicinity (it only slightly clips one MOT beam).

The loop is mounted on the PCB shown in Figure 11. The board has two connections: the top one in Figure 11 has a small loop used as a pickup antenna that we attach to a power detector **Minicircuits ZX47-40-S+** to monitor the the

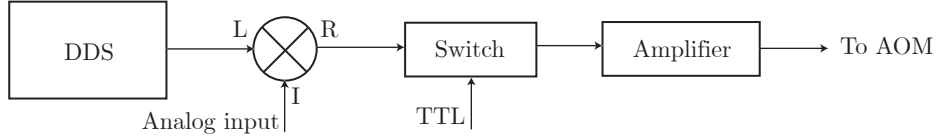


Figure 10: Setup used to drive the AOMs controlling the power and frequency of Raman beams. A similar setup is used to drive a coil used to generate high-power RF fields at the atoms.

antenna and the bottom lines have pads that can be used to make an impedance matching network.

We used a vector network analyzer (VNA) to help us perform the impedance matching. The VNA sends a small amplitude frequency into the circuit and measures the amplitude and phase of the reflected power from which the impedance can be inferred. Figure 12a shows the reflected power as a function of frequency for a test circuit and Figure 12b shows the complex valued impedance as a function of frequency displayed on a Smith chart. The Smith chart is a helpful way to visualize the impedance of a circuit: the black circles correspond to constant resistance, with the right most point corresponding to an open circuit (infinite resistance) and the largest circle corresponding to a short circuit (zero resistance). The arcs correspond to constant reactance; the horizontal axis corresponds to zero reactance ($\text{Im}(Z) = 0$), the top arcs correspond to $\text{Im}(Z) > 0$ and the lower arcs to $\text{Im}(Z) < 0$. The circuit is impedance matched when $Z = 50 \text{ Ohm}$ (the center of the Smith chart), the standard value of RF transmission lines. We tested different components on the pads until we found a peak in reduced transmission at the desired frequency. It is also important to note that it was essential that the circuit was installed in its final location in the

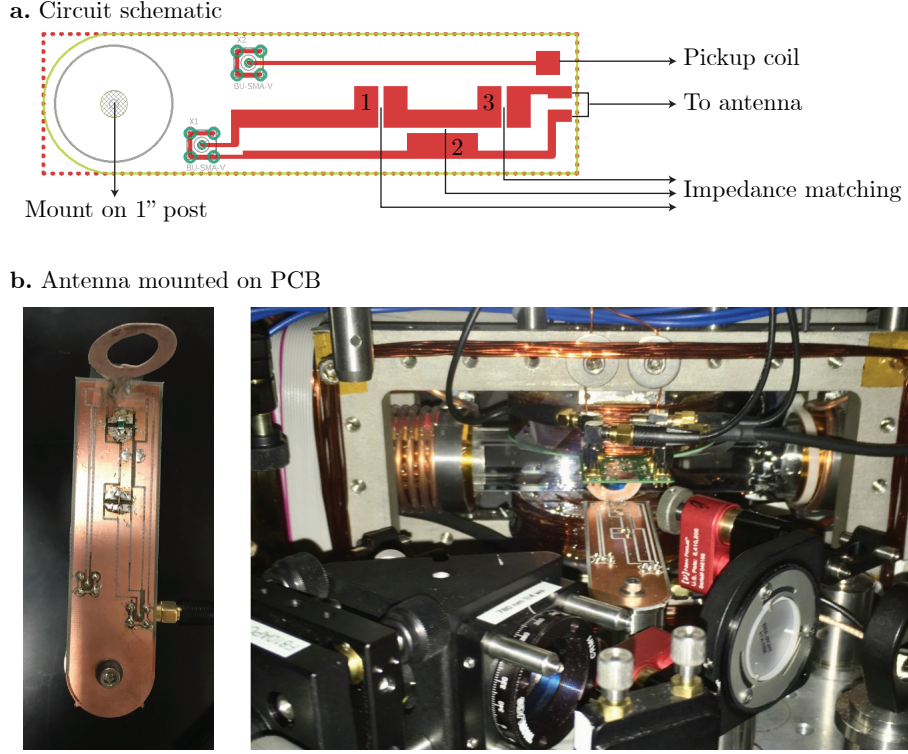


Figure 11: We use a commercial resonator with an impedance matching network to produce high power RF fields. **a.** Diagram of the impedance matching network. **b.** A picture of the resonator mounted on a PCB. We place this device as close to the atoms as possible next to the glass cell.

experiment when measuring the impedance as the other parts in the vicinity of the antenna can shift the resonant frequency.

The driving electronics are very similar to the AOM drivers described in Section 4.3.2. The only difference is we use a 30 W amplifier ([Minicircuits LZY-22+](#)) instead of the smaller amplifiers needed to drive the AOMs.

4.3.4 6.8 GHz microwave system

Our apparatus now has a 6.8 GHz microwave system that allows us to transfer atoms between the $F = 1$ and $F = 2$ ground hyperfine manifolds of ^{87}Rb . We

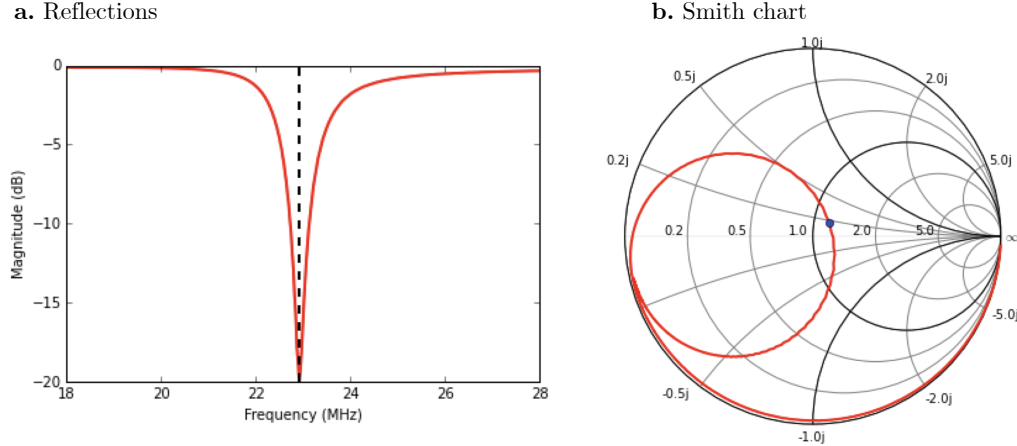


Figure 12: Impedance matching of high power RF antenna. **a.** Reflected power as a function of frequency. **b.** Impedance as a function of frequency, visualized on a Smith chart.

mostly use this system to stabilize the bias magnetic field along \mathbf{e}_z at the atoms using microwave assisted partial transfer absorption imaging (PTAI) (Section 4.2.2). A list of components used to in the setup is presented in Table 4.2 and a diagram of the connections is displayed in Figure 13.

Table 4.2: 6.8 GHz microwave system components

Part number	Description
SRS SG384	Signal generator
Narda 4014C-30	Directional coupler
Marki IRW0618	Mixer
Minicircuits VBFZ-6260-S+	Bandpass filter 6 – 8 GHz
Herley D1956	Voltage controlled attenuator
MSI MSH-5727901	46 dB gain amplifier
Narda 4014C-30	Circulator
Minicircuits ZX47-40-S+	Power detector
Maury microwave 1819C	Stub tuner
ZYSPA-2-50DR	Digital switch

The SRS generator serves as a source of a fixed frequency and amplitude

signal. We control the frequency by mixing a programmable ~ 100 MHz signal from a Novatech into a double balanced mixer; the RF signal can be turned on or off using a TTL switch. The amplitude is controlled by commanding 0–6 V signal from the control computer into an attenuator. The signal is amplified by +43 dB using an amplifier mounted on a water cooled plate. The microwave signal is broadcast to the atoms using a horn antenna. In order to get a coupling microwave coupling strength of the order of 10 kHz or larger it was important to place the horn as close to the atoms as possible and to impedance match the transmission line to maximize the radiated power. We additionally use a circulator that prevents any reflected power to go back into the amplifier. We use couplers at different locations to monitor the performance of the system. The last coupler and the circulator of the system are connected to a power detector that outputs a DC signal proportional to the microwave power. The impedance is tuned with a stub tuner by changing the length of the stubs so that the reflected power measured at the exit port of the circulator is minimized at the desired frequency of operation.

4.4 Computer control and data acquisition

There have been two main changes in our computer control and data acquisition system. We have transitioned from using a LabVIEW based control system to a Python based control system, The `labscrip` suite [43]. With the previous control software the lab devices were programmed using a graphic interface. `Labscrip` instead uses a hybrid approach in which the experimental sequences are

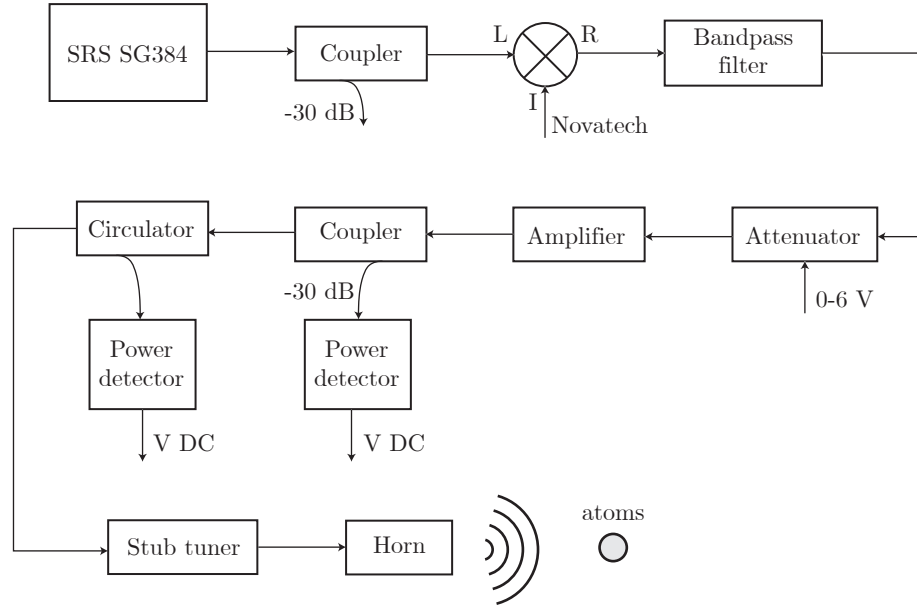


Figure 13: Schematic of 6.8 GHz microwave system.

text based scripts. The use of scripted programming has given us more flexibility and modularity for programming experiments and additionally it is now very easy to do multi-dimensional parameter scans. Each experimental shot is saved in a Hierarchical Data Format version 5 file (HDF5). The file includes images from cameras, oscilloscope traces and analog inputs as well as copy of the script used in the experiment and the values of all of the parameters used. This has been a great upgrade as we no longer rely on the person running an experimental sequence pushing the ‘save’ button and thoroughly documenting the experiment in question³.

The other upgrade worth mentioning is replacing our old Flea3 (FL3-FW-03S1M-C from FLIR, formerly Point Grey) CCD camera with a Mako G-030 camera from **Allied Vision**. With this new camera the time between two consecutive shots

³As I have been digging into old data, I greatly wish we had this feature sooner.

can be as short as $96\,\mu\text{s}$ (we used to wait $\sim 30\,\text{ms}$ with the Flea3 camera), greatly reducing the effect of mechanical vibrations in the experiment that produce fringes in the absorption images. In our experimental sequence the probe and atoms images are separated by $150\,\mu\text{s}$, which is not enough time for the atoms in the first absorption image to be cleared out. We therefore had to change the order in the absorption imaging protocol: first we take a picture of the probe which is $6.8\,\text{GHz}$ detuned and minimally disturbs the atoms, we then apply repump light during the $150\,\mu\text{s}$ interval in between the images to transfer atoms into $F = 2$ and then take the absorption image of the atoms. Figure 14 shows the OD computed using both cameras with no atoms present. When there is a long interval in between the two images the probe captured on the camera changes, leading to the fringes shown in Figure 14a. In contrast for probe images captured within short interval the main noise contribution is shot noise as can be seen in Figure 14b. The addition of this camera was essential to get a better signal to noise ratio in the experiments reported in Chapter 8.

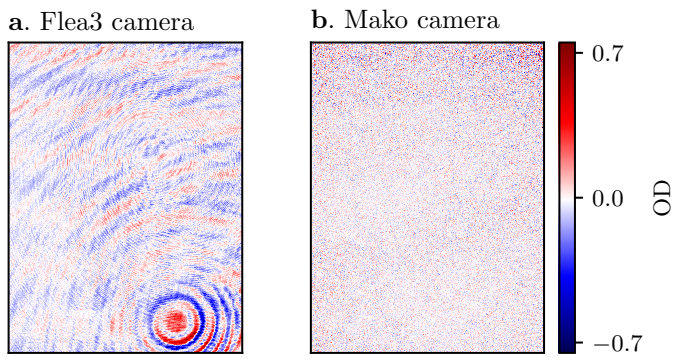


Figure 14: OD computed using two consecutive probe images without atoms. **a.** With the Flea3 camera images are spaced by ~ 30 ms. Changes in the probe result in fringes in the OD. **b.** With the Mako camera images are spaced by $\sim 150 \mu\text{s}$. The main source of noise in the OD is shot noise.

Chapter 5: Fourier Transform Spectroscopy

The idea of using Fourier transform spectroscopy was born from a very different natured project. The project was originally conceived as a way to engineer tunable spin-orbit coupling using multiple-tone Raman transitions. The inspiration came from a previous project where we used multiple-tone Raman transitions to engineer a spin-1 spin-orbit coupled system whose ground state presented different magnetic phases [32]. Fourier spectroscopy was conceived as a new way to characterize the tunable dispersion relation resulting from our proposed coupling scheme. Unfortunately, we realized that this proposal was equivalent to another experiment that achieved tunable SOC using amplitude modulated Raman coupling [44]. We therefore decided to focus on studying Fourier spectroscopy instead, a decision that turned out to be very fruitful for our lab as we continue to use this technique to characterize the spectrum of a variety of systems to this date.

Many spectroscopy techniques in atomic physics rely on using a source of coherent electromagnetic radiation with a well known frequency that probes the internal structure of a system (atom). For example, in absorption spectroscopy [45] a coherent light source is sent through an atomic medium and if the frequency of the light is resonant with an atomic transition it will be absorbed and a reduced transmission

will be measured. Other variants of spectroscopy (e.g. Rabi spectroscopy [30], spin-injection spectroscopy [46]) work under a similar principle: atoms absorb and emit photons with frequencies equal to the transition energies between internal states.

Fourier transform spectroscopy instead employs the connection between the energy spectrum of a system and its dynamics. This connection has been exploited to study the spectrum of both condensed matter [47] and cold atom systems [48, 49] alike. As opposed to other techniques, Fourier spectroscopy relies only on following the unitary evolution of an initial state suddenly subjected to a Hamiltonian of interest and measuring probabilities in a basis that does not diagonalize that Hamiltonian.

The frequency resolution of Fourier transform spectroscopy is limited only by the coherent evolution timescale of the system under study and can otherwise be applied to any system. Other applications of this technique implemented in our lab that are not included in this Chapter include measuring the dispersion relation of a Rashba spin-orbit coupled gas (see Chapter 8) and the band structure of a sub-wavelength optical lattice [50].

In this Chapter I will first give a general description of the Fourier transform spectroscopy technique in Section 5.1. Then in Section 5.2 I will describe a set of experiments where we engineered a tunable spin-orbit coupled system (our original goal) and applied Fourier transform spectroscopy . This work was published in [51].

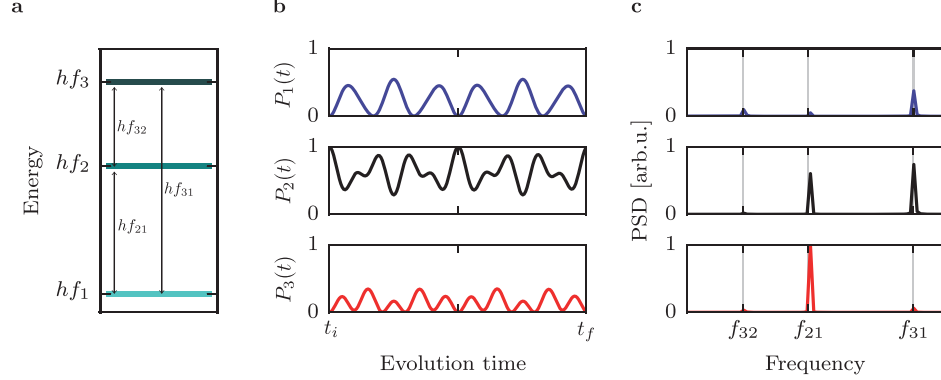


Figure 1: **a.** Eigenenergies of a three-level system described by $\hat{H}'(\Omega_1, \Omega_2, \Omega_3)$. **b.** The system is prepared in $|\psi_2\rangle$ and subjected to \hat{H}' at time t_i . The three panels show the occupation probabilities of the states $|\psi_1\rangle$ (blue), $|\psi_2\rangle$ (black), and $|\psi_3\rangle$ (red) in the measurement basis, for evolution times up to t_f . **c.** Power spectral density of the occupation probabilities from panel b. The three peaks in the Fourier spectra correspond to the energy differences present in panel a.

5.1 Operating principle of Fourier spectroscopy

We focus on a system where we can measure the occupation probabilities of a set of orthonormal states $\{|\psi_i\rangle\}$ that fully span the accessible Hilbert space of the system. We then consider the time evolution of an arbitrary initial state $|\Psi_0\rangle = \sum_i a_i |\psi_i\rangle$ as governed by a Hamiltonian $\hat{H}'(\{\Omega_i\})$ and observe the occupation probabilities of the $\{|\psi_i\rangle\}$ states of the measurement basis as a function of time. When \hat{H}' is applied, the evolution of the initial state is $|\Psi(t)\rangle = \sum_{i,j} a_i c_{i,j} e^{-iE'_j t/\hbar} |\psi'_j\rangle$, where E'_j and $|\psi'_j\rangle$ are the eigenenergies and eigenstates of \hat{H}' , and $c_{i,j}(t) = \langle \psi_i | \psi'_j \rangle$. The probability

$$P_k(t) = |\langle \psi_k | \Psi(t) \rangle|^2 = \left| \sum_{i,j} a_i c_{i,j} c_{j,k}^* e^{-iE'_j t/\hbar} \right|^2 \quad (5.1)$$

of finding the system in a state $|\psi_k\rangle$ of the measurement basis can be expressed as a sum of oscillatory components, with amplitude given by the magnitude of the overlap integrals between the initial state and the eigenvalues of \hat{H}'

$$P_k(t) = 1 + \sum_{i,j \neq l} 2|a_i^2 c_{i,j} c_{j,k} c_{i,l} c_{l,k}| \cos(2\pi f_{j,l} t), \quad (5.2)$$

where $f_{j,l} = (E'_j - E'_l)/\hbar$ is the frequency associated with the energy difference of two eigenstates of the Hamiltonian. Fourier spectroscopy relies on measuring the populations on each state of the measurement basis as a function of time, and extracting the different frequency components $f_{j,l}$ directly by computing the discrete Fourier transform. The bandwidth and frequency resolution of the measurement are determined by the total sampling time and the number of samples. For N samples separated by a time interval Δt , the highest resolved frequency will be $f_{\text{bw}} = 1/2\Delta t$, with resolution $\Delta f = 1/\Delta t N$. This resolution can be decreased if the Fourier transform is calculated using certain types of windowing functions that enhance signal to noise. Any higher frequency $f > f_{\text{bw}}$ will be aliased and measured in the Fourier spectrum as $f_{\text{alias}} = |f - m/\Delta t|$, where m is an integer. If interactions are present in the system, the dynamics get modified in a time scale given by the magnitude of the interactions, giving an additional constraint to the smallest frequency components of a single particle Hamiltonian that can be resolved with our technique.

Figure 1 illustrates the principle of Fourier spectroscopy for a three level sys-

tem, initially prepared in the state $|\Psi_0\rangle = |\psi_2\rangle$, subject to the Hamiltonian

$$\hat{H}' = \begin{pmatrix} E_1 & 0 & 0 \\ 0 & E_2 & 0 \\ 0 & 0 & E_3 \end{pmatrix} + \hbar \begin{pmatrix} 0 & \Omega_1 & \Omega_2 \\ \Omega_1^* & 0 & \Omega_3 \\ \Omega_2^* & \Omega_3^* & 0 \end{pmatrix}, \quad (5.3)$$

where we measure the occupation probability as a function of time for each of the $\{|\psi_1\rangle, |\psi_2\rangle, |\psi_3\rangle\}$ states. The three eigenenergies $E'_i = hf_i$ that result from diagonalizing \hat{H}' are displayed in figure 1a. The three energy differences $hf_{jj'}$ between the levels determine the oscillation frequencies of the occupation probabilities, as can be seen in figure 1b. Finally, a plot of the power spectral densities (PSD) in figure 1c shows three peaks at frequencies corresponding to the three relative energies of \hat{H}' .

5.2 Measuring the SOC dispersion with Fourier transform spectroscopy

5.2.1 System

We applied the Fourier transform spectroscopy technique to measure the dispersion relation of BECs with (tunable) SOC. All of our experiments started with BECs containing about 4×10^4 atoms in the $|f = 1, m_F = -1\rangle$ hyperfine state. The experiments described in Section 5.2.3 were performed in an optical dipole trap with frequencies $(\omega_x, \omega_y, \omega_z)/2\pi = (42(3), 34(2), 133(3))$ Hz. We later modified the trapping frequencies in the xy plane to try to make them more symmetric for the experiments described in Section 5.2.4. We broke the degeneracy of the three m_F magnetic sub-levels by applying a $1.9893(3)$ mT bias field along \mathbf{e}_z that produced

a $\omega_Z/2\pi = 14.000(2)$ MHz Zeeman splitting, and a quadratic Zeeman shift ϵ that shifted the energy of $|f = 1, m_F = 0\rangle$ by $-h \times 28.45$ kHz. We transferred atoms into the $|f = 1, m_F = 0\rangle$ state using ARP and then we monitored and stabilized the magnetic field using partial transfer absorption imaging as described in Chapter 4.2.2 by applying a pair of $250\ \mu\text{s}$ microwave pulses, each of them detuned by ± 2 kHz from the $|f = 1, m_F = 0\rangle \leftrightarrow |f = 2, m_F = 1\rangle$ transition.

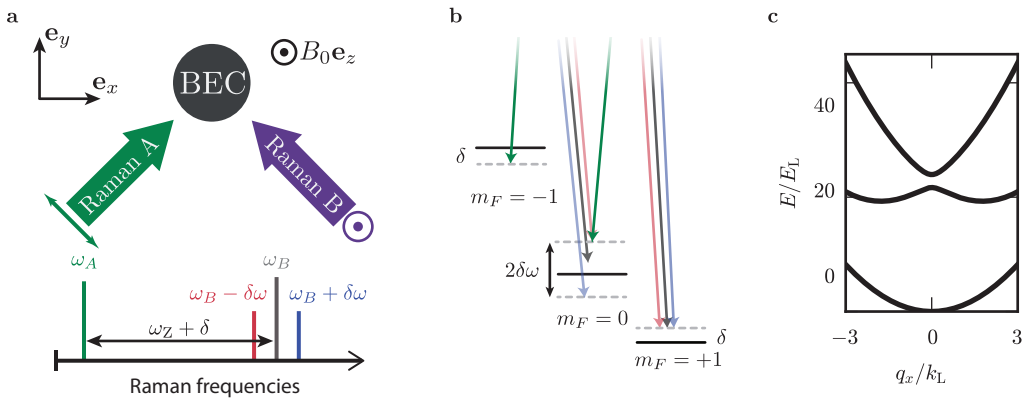


Figure 2: **a.** Setup. A bias magnetic field $B_0 \mathbf{e}_z$, with $B_0 = 1.9893$ mT splits the hyperfine energy levels of the $f = 1$ manifold of ^{87}Rb by $\omega_Z/2\pi = 14$ MHz. A pair of cross polarized Raman beams propagating along $\mathbf{e}_x + \mathbf{e}_y$ and $\mathbf{e}_x - \mathbf{e}_y$ couple the atoms' momentum and spin states. **b.** The Raman frequencies are set to $\omega_A = \omega_L + \delta$ and $\omega_B = \omega_L + \omega_Z$. We add frequency sidebands to ω_B , separated by $\pm \delta\omega$. The amplitude modulation from the interference between the multiple frequency components results in tunable SOC. **c.** SOC dispersion for Raman coupling strength $\Omega_0 = 12E_L$ and $\Omega = 0$, on four photon resonance.

We induced spin-orbit coupling using a pair of intersecting, cross polarized Raman laser beams propagating along $\mathbf{e}_x + \mathbf{e}_y$ and $\mathbf{e}_x - \mathbf{e}_y$, as shown in figure 2a and b. These beams have angular frequency $\omega_A = \omega_L + \delta$ and $\omega_B = \omega_L + \omega_Z$, where 2δ is the, experimentally controllable, detuning from four photon resonance between $m_F = -1$ and $m_F = +1$.

Our system was well described by the Hamiltonian including atom-light inter-

action along with the kinetic contribution

$$\hat{H}_{\text{SOC}} = \frac{\hbar^2 q_x^2}{2m} + \alpha q_x \hat{F}_z + 4E_L \hat{\mathbb{1}} + \hbar \Omega_R \hat{F}_x + (4E_L - \epsilon)(\hat{F}_z^2 - \hat{\mathbb{1}}) + \hbar \delta \hat{F}_z, \quad (5.4)$$

where q is the quasimomentum, $\hat{F}_{x,y,z}$ are the spin-1 angular momentum matrices, $\alpha = \hbar^2 k_L/m$ is the SOC strength, and Ω_R is the Raman coupling strength, proportional to the Raman laser intensity. The Raman field coupled $|m_F = 0, q = q_x\rangle$ to $|m_F = \pm 1, q = q_x \mp 2k_L\rangle$, generating a spin change of $\Delta m_F = \pm 1$ and imparting a $\mp 2k_L$ momentum. The eigenstates of \hat{H}_{SOC} are linear combinations of these states and $|m_F = 0, q = q_x\rangle$, and the set $\{|m_F, q\rangle\}$ constituted the measurement basis for Fourier transform spectroscopy.

Figure 2c shows a typical band structure of our spin-1 SOC system as a function of quasimomentum for a large and negative quadratic Zeeman shift $-\epsilon > 4E_L$. In this parameter regime the ground state band has a nearly harmonic dispersion with an effective mass $m^* = \hbar^2 [d^2 E(k_x)/d^2 x]^{-1}$, only slightly different from that of a free atom.

5.2.2 Tunable SOC

We engineered a highly tunable dispersion relation in which we can independently control the size of the gap at $q_x = 0$ as well as the SOC strength α by adding frequency sidebands to one of the Raman beams. The state of the system can change from $|m_F = -1, q = q_x + 2k_L\rangle$ to $|m_F = 1, q = q_x - 2k_L\rangle$ by absorbing a red

detuned photon first followed by a blue detuned photon and vice versa, in a similar way to the Mølmer-Sørensen entangling gate in trapped ion systems [52]. When we set the angular frequencies of the sidebands to $\omega = \omega_A + \omega_Z \pm \delta\omega$, the Hamiltonian (Equation 5.4) acquired a time-dependent coupling $\Omega_R(t) = \Omega_0 + \Omega \cos(\delta\omega t)$. This periodically driven system is well described by Floquet theory [53] (see Chapter 3.4.3). Figure 3 shows the spectrum of Floquet quasi-energies for a system described by 5.4 where Ω_R oscillates with angular frequency $\delta\omega$.

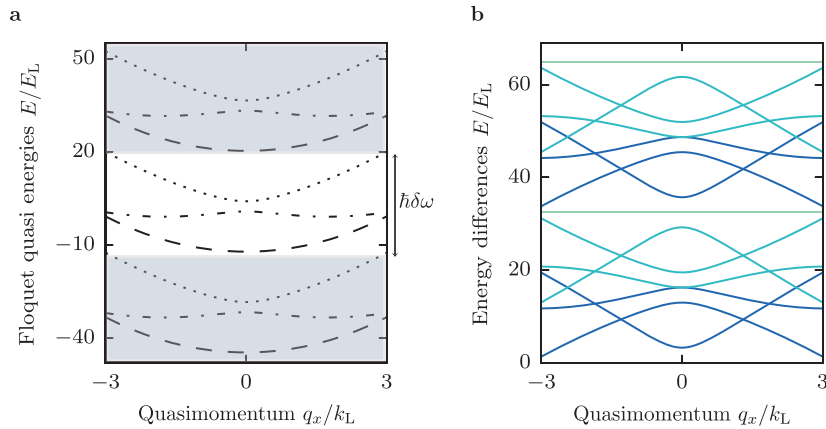


Figure 3: **a.** Floquet quasi-energies of a three level Hamiltonian with SOC and time periodic coupling strength. The quasi-energies are grouped into manifolds consisting of three levels that get repeated with a periodicity equal to $\hbar\delta\omega$. **b.** Energy differences of the Floquet quasi-energies. Each color represents the energy difference, separated by a fixed number of neighboring levels. When the number of neighboring levels is a multiple of 3, the energy differences are straight lines, a result of the periodic structure of the Floquet manifolds.

We found an effective time-independent Hamiltonian by using a unitary transformation $\hat{U}(t)$ and applying a RWA such that the dynamics of the transformed wave function are described by a time independent Hamiltonian. Recall that the time evolution of a wave function in a transformed frame $|\psi'\rangle = \hat{U}^\dagger |\psi\rangle$ is given by the time dependent Schrödinger equation with a Hamiltonian $\hat{H}' = \hat{U}^\dagger \hat{H} \hat{U} - i\hbar \hat{U}^\dagger \partial_t \hat{U}$. Here

we used

$$\hat{U}(t) = \exp[-i\frac{\Omega}{\delta\omega} \sin(\delta\omega t)\hat{F}_x] \quad (5.5)$$

so that $i\hbar\hat{U}^\dagger\partial_t\hat{U} = \hbar\Omega_R(t)\hat{F}_x$. The transformed Hamiltonian $\hat{H}'(t)$ has terms proportional to $\sin(\Omega/\delta\omega \sin(\delta\omega t))$, $\sin^2(\Omega/\delta\omega \sin(\delta\omega t))$, $\cos(\Omega/\delta\omega \sin(\delta\omega t))$ and $\cos^2(\Omega/\delta\omega \sin(\delta\omega t))$ which we simplified using the Jacobi-Anger expansion for large values of θ

$$\begin{aligned} \cos(z \sin \theta) &= J_0(z) + 2 \sum_{n=1}^{\infty} J_{2n}(z) \cos(2n\theta) \approx J_0(z) \\ \sin(z \sin \theta) &= 2 \sum_{n=0}^{\infty} J_{2n+1}(z) \sin((2n+1)\theta) \approx 0, \end{aligned}$$

where J_n is the the n th order Bessel function of the first kind.

This approximation is valid for $\hbar\delta\omega > |\epsilon| + 12E_L$ and $|q_x| \leq 2k_L$ so that quasi-energy manifolds are well separated as in figure 3a. The Floquet Hamiltonian retained the form of Equation 5.4 with renormalized coefficients and an additional coupling term:

$$\hat{H}_{Fl} = \hat{H}_{SOC}(q, \Omega_0, \tilde{\alpha}, \tilde{\delta}, \tilde{\epsilon}) + \tilde{\Omega}\hat{F}_{xz}, \quad (5.6)$$

where $\tilde{\alpha} = J_0(\Omega/\delta\omega)\alpha$, $\tilde{\Omega} = 1/4(\epsilon + 4E_L)[J_0(2\Omega/\delta\omega) - 1]$, $\tilde{\delta} = J_0(\Omega/\delta\omega)\delta$, and $\tilde{\epsilon} = 1/4(4E_L - \epsilon) - 1/4(4E_L + 3\epsilon)J_0(2\Omega/\delta\omega)$. \hat{F}_{xz} is the $\hat{\lambda}_4$ Gell-Mann matrix that directly couples $|m_F = -1, q = q_x + 2k_L\rangle$ and $|m_F = +1, q = q_x - 2k_L\rangle$ states. The experimentally tunable parameters $\delta\omega$, Ω and Ω_0 can be used to tune the SOC

dispersion.

5.2.3 Application of Fourier spectroscopy

We used Fourier transform spectroscopy to measure the spectrum of the SOC Hamiltonian (Equation 5.6) for three coupling regimes: (i) $\Omega_0 \neq 0$ and $\Omega = 0$, (ii) $\Omega_0 = 0$ and $\Omega \neq 0$ and (iii) $\Omega_0 \neq 0$ and $\Omega \neq 0$. We turned on the Raman laser non-adiabatically, in approximately $1\,\mu\text{s}$. We let the system evolve subject to \hat{H}_{SOC} for up to $900\,\mu\text{s}$, and then turned off the laser while releasing the atoms from the optical dipole trap. As usual, we resolved the spin and momentum distribution using Stern-Gerlach and a 21 ms TOF which allowed us to measure the fraction of atoms in each state of the measurement basis $\{|m_F, q\rangle\}$. The density of sampling points and the maximum evolution time were chosen so that the bandwidth of the Fourier transform was comparable to, or larger than, the highest frequency in the evolution of the system while maximizing resolution. Experimental decoherence resulting in loss of contrast of the oscillations, which arises from magnetic field noise and small magnetic field gradients present in our apparatus, was an additional constraint that becomes significant around 1 ms .

In order to map the full spin and momentum dependent band structure of \hat{H}_{SOC} , we measured the time dependent occupation probabilities at a fixed Raman coupling strength and different values of Raman detuning δ , for the same initial state $|m_F = 0, q_x = 0\rangle$. This detuning corresponded to the Doppler shift experienced by atoms moving relative to a light source with quasimomentum $q_x/k_{\text{L}} = \hbar\delta/4E_{\text{L}}$. We

controlled the frequency and the detuning of the Raman beams using two AOMs, one of which is driven by up to three phase coherent frequencies (the carrier frequency plus two sidebands). For each of the three coupling cases that we measured, we applied the Raman beams at detuning values within the interval $\pm 12E_L$ which corresponds to quasimomentum values $\pm 3k_L$.

This approach of changing detuning rather than using atoms with non-zero quasimomentum had the advantage that the state preparation was very reliable (making BECs at rest is easy^{1!}) and we got very good signal to noise ratios due to the relatively high densities of the BECs. The downside is that if one is interested in looking at a large range of quasimomentum values, it takes a long time to repeat each experiment for different detuning values. In future experiments where we used Fourier transform spectroscopy we sacrificed some signal to noise for speed and used the momentum distribution of non-condensed atoms to parallelize our measurements.

5.2.4 Effective mass

Fourier transform spectroscopy only gives access to the relative energies of a Hamiltonian. If we want to recover the absolute energies we need to have an additional energy reference. For this particular set of experiments we had a ground state with a nearly quadratic dispersion and we could measure its effective mass which allowed us to obtain such reference.

We measured the effective mass of the Raman dressed atoms by adiabatically

¹Well, nothing in the lab is really ‘easy’...

preparing the BEC in the lowest eigenstate and inducing dipole oscillations. The effective mass of the dressed atoms is related to the bare mass m and the bare and dressed trapping frequencies ω and ω^* by the ratio $m^*/m = (\omega/\omega^*)^2$. We measured this ratio following [54]; we start in $|m_F = 0, k_x = 0\rangle$ state and adiabatically turn on the Raman laser in 10 ms while also ramping the detuning to $\delta \approx 0.5 E_L$, shifting the minima in the ground state energy away from zero quasi-momentum. We then suddenly bring the field back to resonance, exciting the BEC's dipole mode in the optical dipole trap. We measured the bare state frequency by using the Raman beams to initially induce motion but subsequently turn them off in 1 ms and let the BEC oscillate. For this set of measurements, we adjusted our optical dipole trap to give new trapping frequencies $(\omega_x, \omega_y, \omega_z)/2\pi = (35.6(4), 32.2(3), 133(3))$ Hz, nominally symmetric in the plane defined by \mathbf{e}_x and \mathbf{e}_y . The Raman beams were co-propagating with the optical dipole trap beams; therefore, the primary axes of the dipole trap frequencies are at a 45° angle with respect to the direction of \mathbf{k}_L .

The kinetic and potential terms in the Hamiltonian including the contribution of the Raman and optical dipole trap were

$$\begin{aligned}
 \hat{H}_\perp &= \frac{\hbar^2 q_x^2}{2m^*} + \frac{\hbar^2 q_y^2}{2m} + \frac{m}{2} [\omega_{x'}^2 x'^2 + \omega_{y'}^2 y'^2] \\
 &= \frac{\hbar^2}{2m^*} k_x^2 + \frac{1}{2m} k_y^2 + \frac{m}{4} [(\omega_{x'}^2 + \omega_{y'}^2)(x^2 + y^2) + 2xy(\omega_{x'}^2 - \omega_{y'}^2)], \tag{5.7}
 \end{aligned}$$

where we have used $x' = (x + y)/\sqrt{2}$ and $y' = (x - y)/\sqrt{2}$ to rotate the dipole trap coordinates by 45° . For an axially symmetric trap with $\omega_{x'} = \omega_{y'}$, the frequency of

oscillation along the Raman recoil direction is

$$\omega_x^2 = \frac{m}{2m^*}(\omega_{x'}^2 + \omega_{y'}^2). \quad (5.8)$$

Our trap had a small 3.4 Hz asymmetry and therefore there is some coupling of the motion along the axis perpendicular to \mathbf{k}_L which becomes more significant at larger values of effective mass. The sampling times for the measurements were small compared to the trap asymmetry and therefore we can locally approximate the motion of the atoms by simple harmonic function with a frequency along \mathbf{e}_x given by Equation 5.8.

Figure 4 shows the dipole oscillations along the \mathbf{e}_x and \mathbf{e}_y directions for the three different coupling regimes we explored, as well as the bare state motion. The resulting mass ratios for the three coupling regimes are $m/m^* =$ (i) 1.04(8), (ii) 0.71(7), and (iii) 0.62(4).

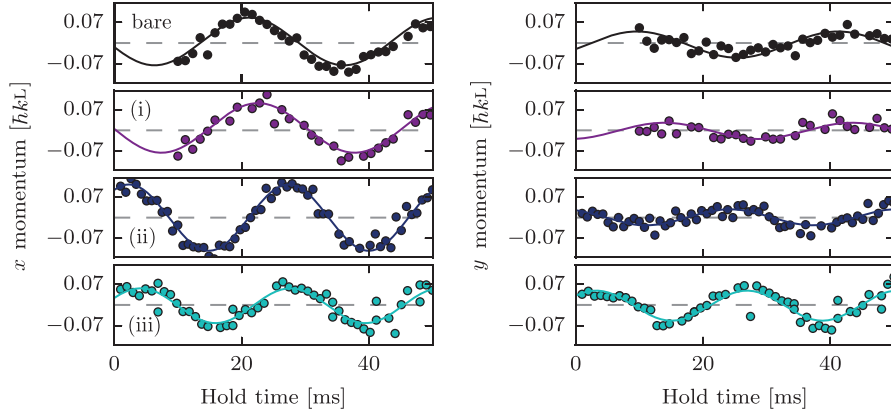


Figure 4: Oscillation of the BEC in the dipole trap along the recoil directions \mathbf{e}_x and \mathbf{e}_y for (top) bare atoms, and the three parameter regimes that we explored (i), (ii), and (iii). We believe that the observed low amplitude oscillations along \mathbf{e}_y are due to the initial detuning ramp not being fully adiabatic.

5.2.5 Measured dispersion

We mapped the band structure of SOC atoms for three different coupling regimes. Figure 5a shows representative traces of the measured occupation probabilities for short evolution times along with fits to the unitary evolution given by \hat{H}_{SOC} with δ , Ω_0 , and Ω as free parameters. The fit parameters agree well with independent microwave and Raman power calibrations. In the lower two panels, where the Raman coupling strength was periodically modulated, the occupation probabilities oscillate with more than three frequencies since the full description of the system was given by a Floquet quasi-energy spectrum. Figure 5b,c shows the occupation probabilities for the parameter regime (iii) for longer evolution times along with the PSD of the occupation probability of each spin state.

We used a non-uniform fast Fourier transform algorithm (NUFFT) on a square window to obtain the power spectral density of the occupation probabilities since our data points were not always evenly spaced because of imperfect imaging shots. The heights of the peaks in the PSD are related to the magnitude of the overlap integrals between the initial state and the Raman dressed states. Figure 5c shows the raw PSD of the time evolution of the system under \hat{H}_{SOC} for a given Raman coupling strength and detuning. We put together all the PSDs for the three coupling regimes in the spectra shown on the top three panels in figure 6. Each column corresponds to a different coupling regime and the colors represent the different spin states of the measurement basis. The spectra show that some overlap integrals vanish near $\delta = 0$, which is manifested as missing peaks in the PSD. The periodic structure of the

Floquet quasi-energy spectrum gives rise to peaks at constant frequencies of $\delta\omega$ and $2\delta\omega$ independently of the Raman detuning, and a structure that is symmetric about the frequencies $2\pi f_1 = \delta\omega/2$ and $2\pi f_2 = \delta\omega$. If you are interested in seeing another nice experiment where the Floquet quasienergy spectrum becomes important due to breaking of the RWA see [55].

We obtained the characteristic dispersion of a SOC system after adding a quadratic term to the PSD, proportional to the measured effective mass, and after rescaling the detuning into recoil momentum units. We combined the PSD of the time evolution of the three $|m_F\rangle$ states to look at the spin dependence of the spectra. Figure 7 shows the measured dispersion relations as well as the Floquet quasi-energies calculated for the Hamiltonian parameters obtained from our calibrations. The spectral lines that can be resolved with our technique depend on the overlap integrals of the initial state with the target Hamiltonian eigenstates. Additional energies can be measured by repeating the experiment with different initial states. The spectral lines we were able to resolve are in good agreement with the calculated energies of the Hamiltonian.

Finally, because it is not so trivial to visualize what we did to recover the dispersion for the periodically driven SOC cases, Figure 8 illustrates in detail the steps that were taken. The red line in panel a represents a level within a Floquet manifold that has the largest overlap integral with the initial $|m_F = 0, q = 0\rangle$ state. The peaks in the PSD correspond to energy differences between the marked level and the levels in neighboring Floquet manifolds pointed by the colored arrows. We show the theoretically computed energy differences on top of the measured PSD in

panel b. The lowest frequency dominant peaks of the PSD correspond to energy differences with the adjacent lower Floquet manifold. To properly recover the SOC dispersion we need to shift the PSD by a negative quadratic term $-\hbar^2 q_x^2 / 2m^*$ as we show on panel c. We finally invert the frequency axis and shift it by $\delta\omega$. Including the effective mass to reconstruct the spectrum of the time-independent SOC case, amounts to shifting the PSD by a positive quadratic term.

Conclusion

We introduced the basic principles of the Fourier transform spectroscopy technique and used it to measure the spin and momentum dependent dispersion relation of a spin-1 spin-orbit coupled BEC. We additionally studied a periodically driven SOC system and found a rich Floquet quasi-energy spectrum. Our method can be applied generically to any system with long enough coherent evolution to resolve the energy scales of interest, and could prove particularly useful to study systems where it is harder to predict or compute the exact energies, such as cold atom realizations of disordered or highly correlated systems [56]. Moreover, this technique can be extended with the use of spectrograms to study time dependent spectra, such as that of systems with quench-induced phase transitions.

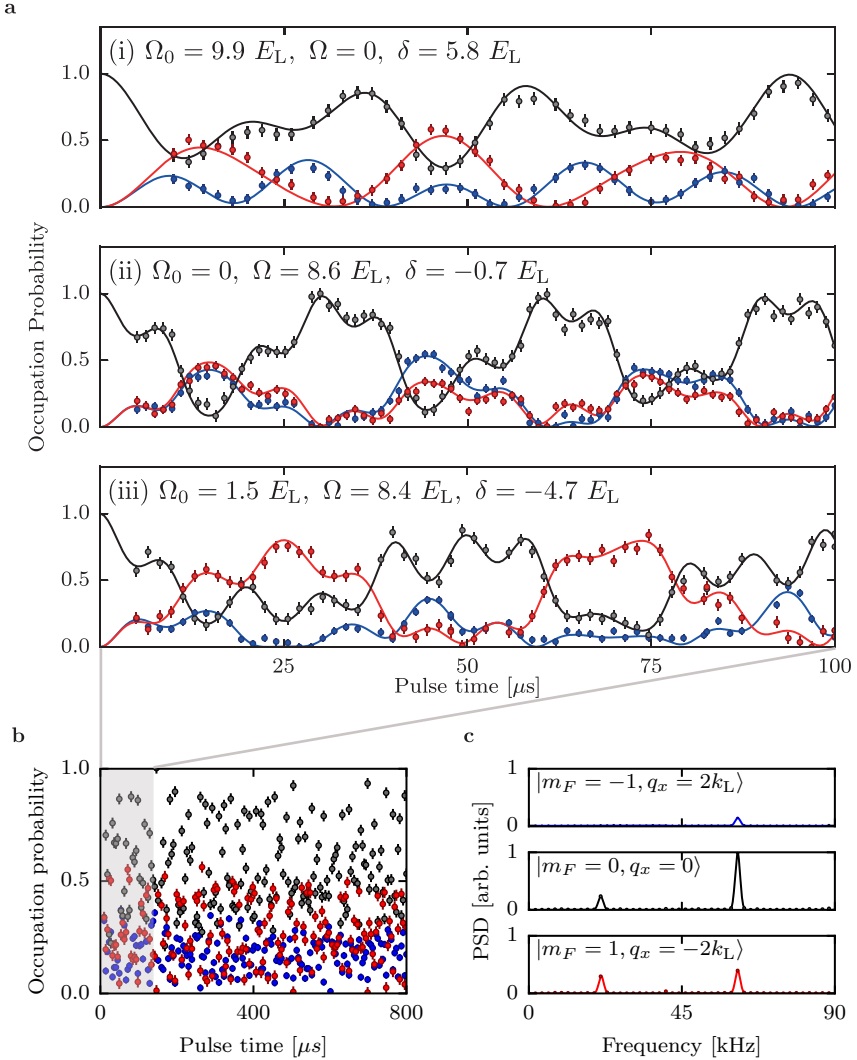


Figure 5: **a.** Occupation probability for the three states in the measurement basis $|m_F = -1, q = q_x + 2k_L\rangle$ (blue), $|m_F = 0, q = q_x\rangle$ (black), and $|m_F = +1, q = q_x - 2k_L\rangle$ (red), following unitary evolution under \hat{H}_{SOC} for times up to 100 μ s at different spin-orbit coupling regimes: (i) $\Omega_0 = 9.9 E_L$, $\Omega = 0$, $\delta = 5.8 E_L$, (ii) $\Omega_0 = 0$, $\Omega = 8.6 E_L$, $\delta = -0.7 E_L$, $\delta\omega = \epsilon + 12 E_L$, and (iii) $\Omega_0 = 1.5 E_L$, $\Omega = 8.4 E_L$, $\delta = -4.7 E_L$, $\delta\omega = \epsilon + 17 E_L$. **b.** Occupation probability for long pulsing up to 800 μ s for parameters as in (iii). **c.** Power spectral density of the occupation probability. We subtract the mean value of each probability before taking the Fourier transform to remove peaks at $f = 0$. The peaks in the PSD then correspond to the relative eigenenergies of \hat{H}_{SOC} .

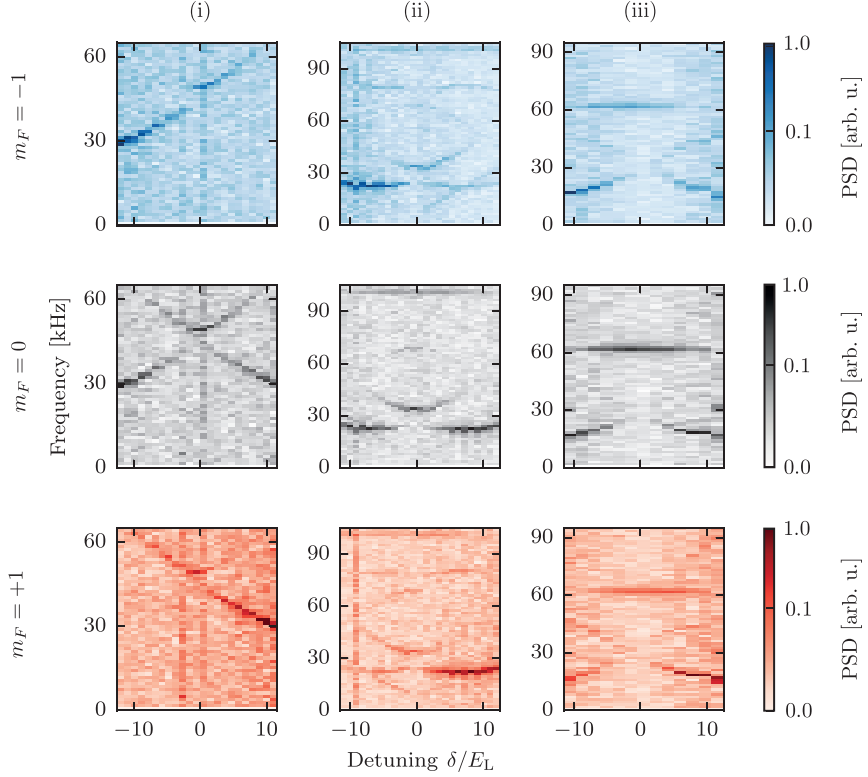


Figure 6: Power spectral density of the time dependent occupation probability for each state in the measurement basis for three coupling regimes: (Left) $\Omega_0 = 9.9E_L$, $\Omega = 0$, (Center) $\Omega_0 = 0$, $\Omega = 8.6E_L$, $\delta\omega = \epsilon + 12E_L$, and (Right) $\Omega_0 = 4.9E_L$, $\Omega = 8.4E_L$, $\delta\omega = \epsilon + 17E_L$. Each panel is normalized to peak amplitude to highlight small amplitude features in the PSD of the periodically driven SOC, and the highest value on the frequency axis corresponds to the FFT bandwidth.. **b.** Spin-dependent SOC dispersion for three different coupling regimes. We combine the PSD of the occupation probability of the states $|m_F = \pm 1, q_x = \mp 2k_L\rangle$, and shift each frequency by an amount proportional to the squared quasimomentum and the effective mass. The dashed lines are the calculated Floquet energies for the Hamiltonian using our calibration parameters.

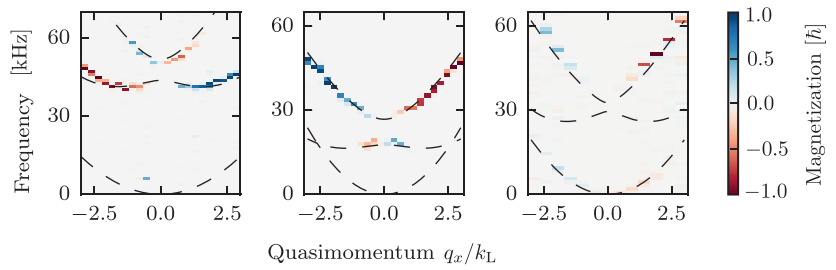


Figure 7: Spin-dependent SOC dispersion for three different coupling regimes. We combine the PSD of the occupation probability of the states $|m_F = \pm 1, q_x = \mp 2k_L\rangle$, and shift each frequency by an amount proportional to the squared quasimomentum and the effective mass. The dashed lines are the calculated Floquet energies for the Hamiltonian using our calibration parameters.

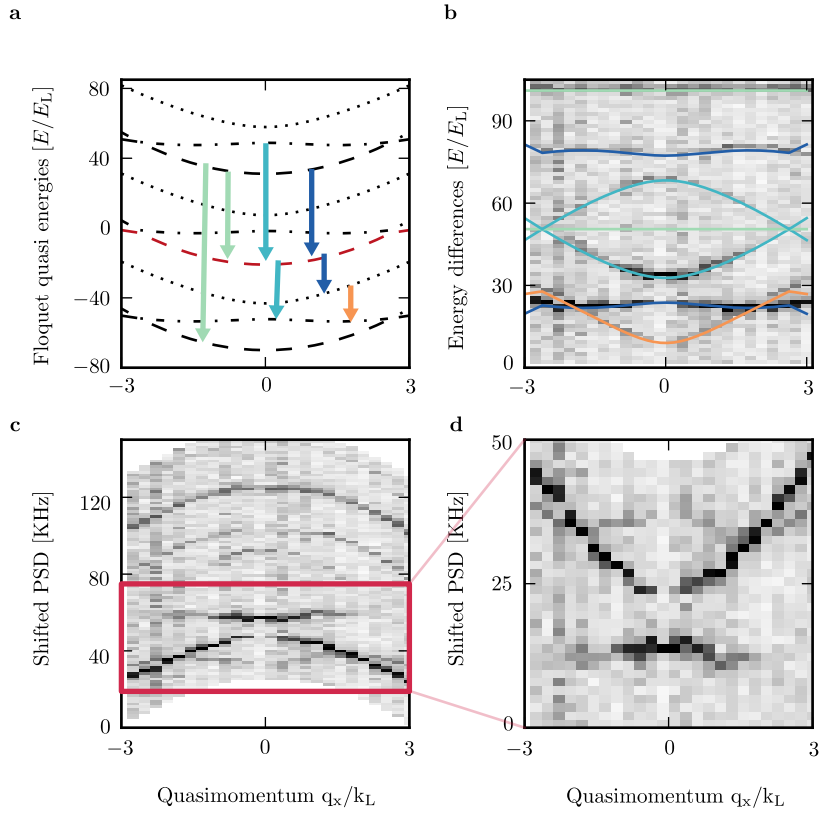


Figure 8: **a** Floquet quasi-energy spectrum of a SOC Hamiltonian with periodic coupling strength. The red line represents the eigenstate that has the largest overlap with the initial $|m_F = 0\rangle$ state. The arrows indicate the energies of the states that have non-zero overlap with the initial state and can be measured with Fourier transform spectroscopy. **b** PSD of the occupation probability and numerically calculated energy differences between the levels indicated by the arrows on panel a. **c** PSD shifted by a quadratic term $-\hbar^2 q_x^2 / 2m^*$. The red box indicates the region of interest where we can recover the SOC spectrum. **d** We invert the frequency axis and shift it by $\delta\omega$.

Chapter 6: Synthetic clock transitions through continuous dynamical decoupling

Most of the experiments and experimental techniques described so far have used the hyperfine $|m_F\rangle$ states as effective spins and dressed them with an RF or Raman field. However, due to the linear dependence of their energies with respect to magnetic field, and our lack of control of environmental changes we always had to take special care to stabilize the magnetic field on the lab (see Section 4.2.2). An alternative to doing active magnetic field stabilization is to use of ‘clock’ transitions which are first order insensitive to changes in magnetic field, however, they are not present in all systems or for arbitrary system parameters. However, under almost all circumstances, clock transitions can be synthesized using dynamical decoupling protocols. These protocols involve driving the system with an external oscillatory field, resulting in a dynamically protected ‘dressed’ system.

The idea of implementing continuous dynamical decoupling (CDD) in the lab came from a theoretical proposal to engineer Rashba type SOC using Raman beams and a strong RF field [57], the second being a necessary ingredient for CDD. We initially worked in implementing CDD protocols to create ‘synthetic clock states’ as an intermediate step towards our final goal of engineering Rashba SOC. Just like

with Fourier spectroscopy, CDD became a workhorse of the lab both for the stability it provides against environmental fluctuations and because it has given us access to non-zero matrix coupling elements that we otherwise would not have when working with the bare $|m_F\rangle$ states. We have continued to use CDD not only for engineering Rashba SOC (Chapter 8) but also to engineer subwavelength optical lattices [50] and Hofstadter [58] cylinders (work in preparation). On the theory side, we also worked on a proposal that uses them as a platform for emulating \mathcal{PT} symmetric Hamiltonians [59].

This Chapter discusses the implementation of CDD in our system of ultra-cold atoms. First I will give a general overview of dynamical decoupling and continuous dynamical decoupling. Then I will describe the technical details and characterization of our CDD protocol which produces a protected three-level system of dressed-states and whose Hamiltonian is fully controllable. Finally I discuss an implementation of concatenated CDD that renders the system first-order insensitive to both magnetic field noise and noise in the control field. This work was published in [60] and was done in parallel with [61].

6.1 Basic principles of CDD

Dynamical decoupling (DD) protocols consist in applying an external control Hamiltonian, generally implemented by a series of pulses, which has the effect of canceling out the dynamics that arise from the quantum system coupling to the environment. DD was first introduced in the context of nuclear magnetic resonance

(NMR) with the discovery of spin-echoes [62], where a ‘refocusing’ pulse was applied to eliminate dephasing of spins resulting from variations in magnetic field. These ideas were later generalized in [63] to protect a system from decoherence induced by interactions with a quantum environment. Continuous dynamical decoupling (CDD) relies on the application of time-periodic continuous control fields, rather than a series of pulses. Unlike conventional dynamical decoupling, CDD does not require any encoding overhead or quantum feedback measurements.

A number of dynamical decoupling protocols, pulsed or continuous, have been shown to isolate quantum systems from low-frequency environmental noise [64–72]. Thus far, CDD has inoculated multi-level systems in nitrogen vacancy centers in diamond, nuclear magnetic resonance experiments, and trapped atomic ions [73–80], from spatiotemporal magnetic field fluctuations.

6.2 CDD of a spin-1 system

We implemented CDD using a strong RF magnetic field with strength Ω , that linked the three $|m_F\rangle$ states comprising the $F = 1$ electronic ground state manifold of ^{87}Rb . The RF field was linearly polarized along \mathbf{e}_x , and had angular frequency ω close to the Larmor frequency $\omega_0 = g_F\mu_{\text{B}}B_0$ from a magnetic field $B_0\mathbf{e}_z$; g_F is the Lande g -factor and μ_{B} is the Bohr magneton. Using the rotating frame approximation for the frame rotating at ω (which is valid for $\omega \gg \Omega$), the system is described by

$$\hat{H} = \hbar\Delta\hat{F}_z + \hbar\epsilon(\hat{F}_z^2 - \hat{\mathbb{1}}) + \hbar\Omega\hat{F}_x, \quad (6.1)$$

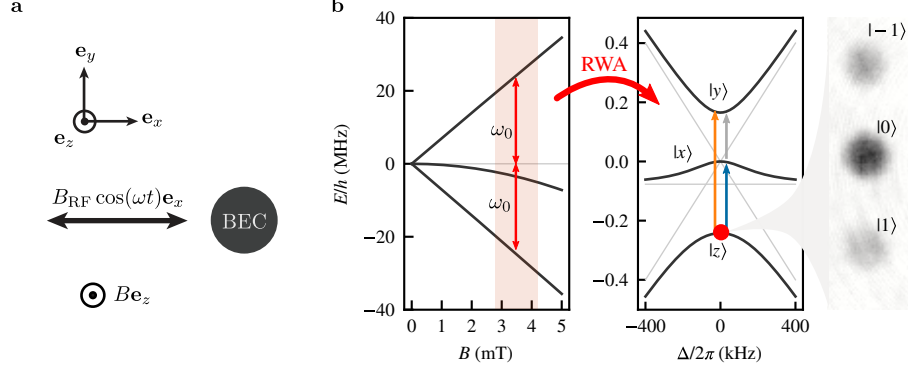


Figure 1: **a.** Setup for implementing CCD using a strong RF magnetic field. **b.** Left: dependence of the $5^2S_{1/2}$, $F = 1$ ground state of ^{87}Rb on magnetic field, where the quadratic dependence of the $|m_F = 0\rangle$ state's Zeeman shift has been exaggerated so it is visible on the same scale. Center: energies of the $|xyz\rangle$ eigenstates, for $\Omega/2\pi = 200$ kHz (black curves) and $\Omega = 0$ (grey curves). Right: TOF absorption image of $|z\rangle$ at $\Delta = 0$, showing the constituent $|m_F\rangle$ states.

with detuning $\Delta = \omega - \omega_0$; quadratic Zeeman shift ϵ ; spin-1 angular momentum operators $\hat{F}_{x,y,z}$; and identity operator $\hat{\mathbb{1}}$.

6.3 The $|xyz\rangle$ states

The eigenstates of Equation 6.1 correspond to the CDD basis. In this section I describe their properties and show that they are first order insensitive to magnetic field fluctuations.

6.3.1 State decomposition

We denote the eigenstates of Equation 6.1 by $|x\rangle$, $|y\rangle$ and $|z\rangle$. They are linear combinations of the $|m_F\rangle$ basis states, and for $\Delta = 0$ the (non-normalized)

eigenvectors are:

$$\begin{aligned}
|x\rangle &= | -1 \rangle - | 1 \rangle, \\
|y\rangle &= | -1 \rangle - \frac{\epsilon + \tilde{\Omega}}{\sqrt{2\Omega}} | 0 \rangle + | 1 \rangle, \\
|z\rangle &= | -1 \rangle - \frac{\epsilon - \tilde{\Omega}}{\sqrt{2\Omega}} | 0 \rangle + | 1 \rangle.
\end{aligned} \tag{6.2}$$

Figure 2 shows the full state decomposition as a function of Δ , where it can be seen that the $|xyz\rangle$ states adiabatically map to the $|m_F\rangle$ states for $\Delta \gg \Omega$: for positive (negative) detuning $|z\rangle$ maps to $|1\rangle$ ($| -1 \rangle$); $|y\rangle$ maps in the exact opposite way to $|z\rangle$; and $|x\rangle$ always maps to $|0\rangle$.

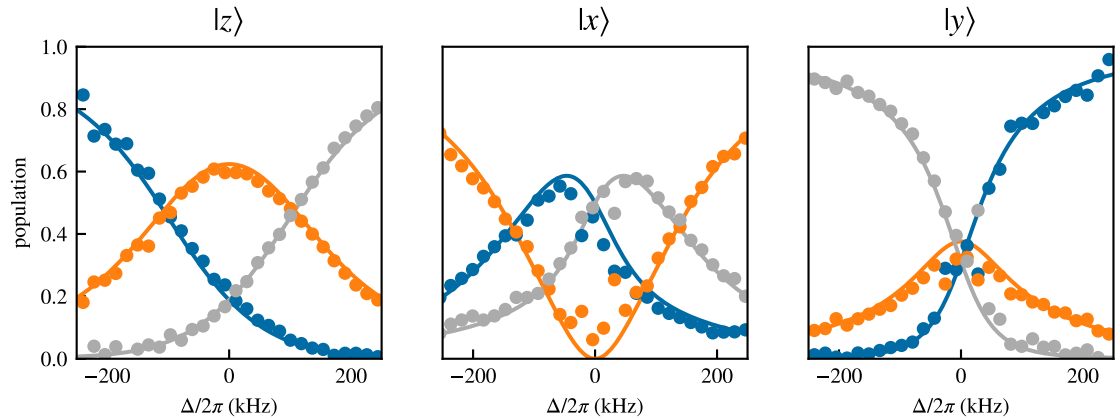


Figure 2: Decomposition of the $|xyz\rangle$ states on the $|m_F\rangle$ basis for $\Omega/2\pi = 145(1)$ kHz. The $|m_F = -1, 0, 1\rangle$ states correspond to blue, orange, gray respectively.

We labeled our dressed states $|xyz\rangle$ since for $\Omega \rightarrow 0^+$ and $\Delta = 0$, they contin-

uously approach the $|XYZ\rangle$ states familiar from quantum chemistry [81]:

$$\begin{aligned} |X\rangle &= \frac{|1\rangle - |-1\rangle}{\sqrt{2}}, \\ |Y\rangle &= i\frac{|1\rangle + |-1\rangle}{\sqrt{2}}, \\ |Z\rangle &= |0\rangle. \end{aligned} \tag{6.3}$$

which transform under the application of the spin-1 operators as $\epsilon_{jkl}\hat{F}_j|k\rangle = i\hbar|l\rangle$, so that a resonant probe field can induce transitions between at least one pair of states, irrespectively of its polarization.

Finally, when $\Omega \rightarrow \infty$ they are independent of the driving field amplitude and continuously approach the eigenstates of the \hat{F}_x operator

$$\begin{aligned} |x\rangle &= |1\rangle - |-1\rangle, \\ |y\rangle &= |1\rangle + \sqrt{2}|0\rangle + |-1\rangle, \\ |z\rangle &= |1\rangle - \sqrt{2}|0\rangle + |-1\rangle. \end{aligned} \tag{6.4}$$

6.3.2 Energies

We can understand the clock-like nature of these states by looking at their eigenvalues which are even functions with respect to Δ as can be seen by the leading

order expansion of the eigenenergies $E_i = \hbar\omega_i$ for $\Delta \rightarrow 0$

$$\begin{aligned}\omega_x &= -\frac{\epsilon}{\Omega^2}\Delta^2 + \mathcal{O}(\Delta^4), \\ \omega_y &= \frac{1}{2}(-\epsilon + \tilde{\Omega}) - \frac{(\epsilon + \tilde{\Omega})}{-\epsilon^2 - 4\Omega^2 + \epsilon\tilde{\Omega}}\Delta^2 + \mathcal{O}(\Delta^4), \\ \omega_z &= \frac{1}{2}(-\epsilon - \tilde{\Omega}) + \frac{(\epsilon - \tilde{\Omega})}{\epsilon^2 + 4\Omega^2 + \epsilon\tilde{\Omega}}\Delta^2 + \mathcal{O}(\Delta^4),\end{aligned}\quad (6.5)$$

where we have defined $\tilde{\Omega} = \sqrt{4\Omega^2 + \epsilon^2}$. The energy differences $\hbar\omega_{xy}$, $\hbar\omega_{zy}$ and $\hbar\omega_{zx}$ are only quadratically sensitive to Δ for $\Delta \ll \Omega$ ¹ so that detuning fluctuations $\delta\Delta$ are suppressed to first order, making these a trio of synthetic clock states. For the zx transition, the curvature of ω_x and ω_z has the same sign for $\epsilon < \tilde{\Omega}$ (Equation 6.5). Since the quadratic term changes curvature it can be made arbitrarily small. However, this cancellation does not take place when we consider the dependence of ϵ on Δ from the Breit-Rabi expression. However one can still find an optimal Ω for which ω_{zx} depends quartically on Δ .

6.3.3 Transition matrix elements

Unlike the $|m_F\rangle$ basis, an oscillatory magnetic field with the right polarization can drive transitions between all pairs of the $|xyz\rangle$ states with non-zero transition matrix elements. The transition matrix elements between the $|xyz\rangle$ have a dependence on both Ω and Δ . For the $\Delta = 0$ case they can be read from the representation of the spin-1 matrices in the $|xyz\rangle$ basis

¹The energies are quadratic in Δ for $\Delta \ll \Omega$, and linear for $\Delta \gg \Omega$ with a slope of 7 MHz/mT.

$$\begin{aligned}
\hat{F}_x &\rightarrow \begin{pmatrix} \frac{2\Omega}{\tilde{\Omega}} & 0 & -\frac{\epsilon}{\tilde{\Omega}} \\ 0 & 0 & 0 \\ -\frac{\epsilon}{\tilde{\Omega}} & 0 & -\frac{2\Omega}{\tilde{\Omega}} \end{pmatrix} \\
\hat{F}_y &\rightarrow \begin{pmatrix} 0 & -\frac{i(\tilde{\Omega}-\epsilon)}{\Omega\sqrt{\frac{(\epsilon-\tilde{\Omega})^2}{\Omega^2}+4}} & 0 \\ \frac{i(\tilde{\Omega}-\epsilon)}{\Omega\sqrt{\frac{(\epsilon-\tilde{\Omega})^2}{\Omega^2}+4}} & 0 & -\frac{i(\tilde{\Omega}+\epsilon)}{\Omega\sqrt{\frac{(\tilde{\Omega}+\epsilon)^2}{\Omega^2}+4}} \\ 0 & \frac{i(\tilde{\Omega}+\epsilon)}{\Omega\sqrt{\frac{(\tilde{\Omega}+\epsilon)^2}{\Omega^2}+4}} & 0 \end{pmatrix} \\
\hat{F}_z &\rightarrow \begin{pmatrix} 0 & -\frac{\sqrt{\frac{\epsilon}{\tilde{\Omega}}+1}}{\sqrt{2}} & 0 \\ -\frac{\sqrt{\frac{\epsilon}{\tilde{\Omega}}+1}}{\sqrt{2}} & 0 & -\frac{2}{\sqrt{\frac{(\tilde{\Omega}+\epsilon)^2}{\Omega^2}+4}} \\ 0 & -\frac{2}{\sqrt{\frac{(\tilde{\Omega}+\epsilon)^2}{\Omega^2}+4}} & 0 \end{pmatrix}, \tag{6.6}
\end{aligned}$$

where the states have been ordered by decreasing energy ($|y\rangle$, $|x\rangle$, $|z\rangle$). We can therefore see that a term in a Hamiltonian that is proportional to \hat{F}_x can only drive transitions between $|z\rangle$ and $|y\rangle$ and that coupling terms proportional to \hat{F}_y and \hat{F}_z can drive both drive transitions between $|z\rangle$ and $|x\rangle$ or $|x\rangle$ and $|y\rangle$ with different strengths. It can be seen from Equation 6.6 that when Ω and ϵ are comparable in magnitude there exists at least one non-zero transition matrix element for each pair of dressed states and they can all be coupled cyclically.

6.4 $|xyz\rangle$ state preparation

We implemented CCD to BECs with $N \approx 5 \times 10^4$ atoms. For all of the experiments described in this Chapter the dipole trap had trapping frequencies of $(f_x, f_y, f_z) = (42(3), 34(2), 133(3))$ Hz. We applied a $B_0 \approx 3.27$ mT bias field that lifted the ground state degeneracy, giving an $\omega_0/2\pi = 22.9$ MHz Larmor frequency, with a quadratic shift $\epsilon/2\pi = 76.4$ kHz. We determined that the ambient magnetic field fluctuations were dominated by contributions from line noise giving an rms uncertainty $\delta\Delta/2\pi = g_F\mu_B\delta B/h = 0.67(3)$ kHz.

The state preparation consisted of two stages of ARP. On the first stage we followed the usual protocol described in Section 4.2.1 to prepare the BEC in any of the $|m_F = 0, -1, 1\rangle$ states. On the second stage we adiabatically transformed the $|m_F\rangle$ states into the $|xyz\rangle$ states. We started with the bias field far from resonance ($\Delta(t = 0)/2\pi \approx -450$ kHz) and with all coupling fields off. Then we ramped on Ω in a two-step process. We first ramped from $\Omega = 0$ to an intermediate value Ω_{mid} , approximately half its final value in 1 ms. We then ramped Δ to zero in 3 ms by increasing the magnetic field B_0 . After allowing B_0 to stabilize for 30 ms, we ramped the RF dressing field to its final value Ω in 1 ms, yielding the dynamically decoupled $|xyz\rangle$ states. It was important that the wait for the field to stabilize was performed at an intermediate Ω_{mid} as we found several times that the capacitors on the impedance matching network of the antenna used to generate the RF field would burn if we kept the power on for too long. After performing any experiment with the $|xyz\rangle$ states we measured their populations by adiabatically deloading them

back into the $|m_F\rangle$ basis. We first ramped B_0 so that Δ approached its initial detuned value in 2 ms, and then ramped off the dressing RF field in 1 ms. A typical experimental sequence for Δ and Ω can be visualized in Figure 4. As usual, we obtained the spin-resolved momentum distribution using absorption imaging after TOF, with a Stern-Gerlach field to spatially separate the spin components. The right panel of Figure 1b shows a TOF image of the $|m_F\rangle$ state decomposition of the $|z\rangle$ state. For this image as well as for the measurement of the dressed state decomposition shown in Figure 2 we suddenly (not-adiabatically) turned the RF coupling off, thereby projecting the $|xyz\rangle$ states back into the $|m_F\rangle$ basis.

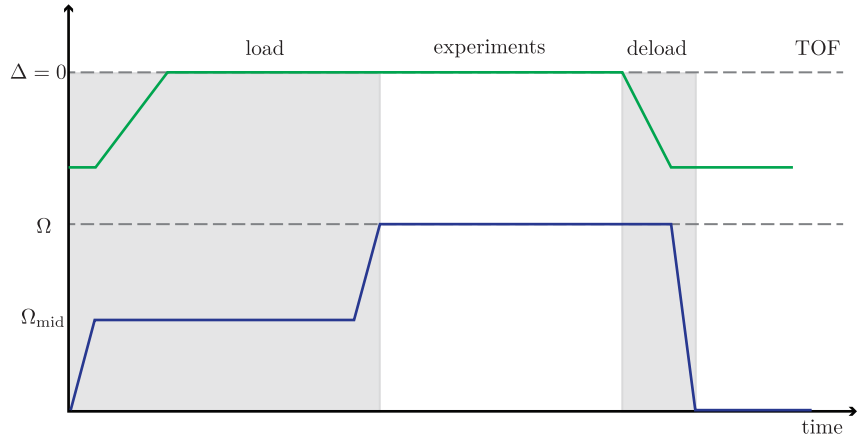


Figure 3: Detuning and RF coupling strengths ramps (not to scale) performed to adiabatically prepare the $|xyz\rangle$ states starting in the $|m_F\rangle$ states and vice versa.

6.5 Initial characterization of Ω

Producing RF fields with large coupling strength was not a trivial task and when testing different antenna designs it was important to have an easy and quick way of characterizing them. We mostly relied on two different techniques to get an

initial estimate of Ω : first, we prepared atoms in $|m_F = -1\rangle$ and pulse on the RF to drive transitions between the three $|m_F\rangle$ states. We would then fit the populations in the three states as a function of pulsing time to the time evolution given by propagating the time dependent Schrödinger equation using the RF Hamiltonian (Equation 6.1) with Ω and Δ as free parameters.

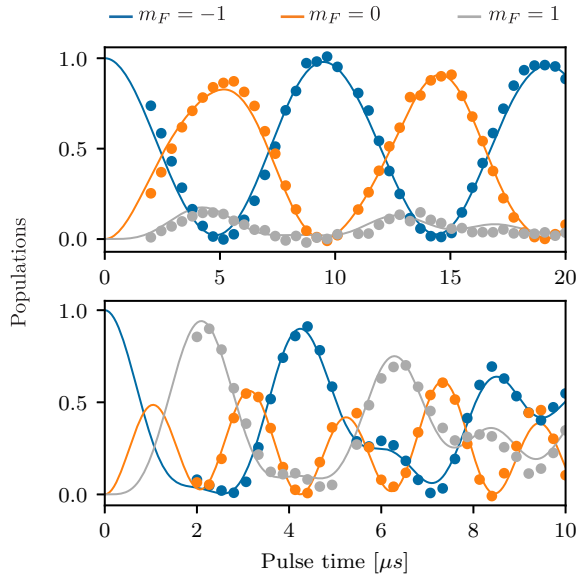


Figure 4: We prepared the system in the $|m_F = 0\rangle$ state and pulsed Ω and fit the populations in the $|m_F\rangle$ states as a function of pulsing time to get an initial estimate of Ω . The top panel shows the time evolution of $\Omega/2\pi \approx 76$ kHz and the bottom panel shows the evolution for $\Omega/2\pi \approx 238$ kHz

Alternatively, we followed the loading procedure described in Section 6.4 but suddenly turned Ω off for different values of Δ to get the decomposition of the $|xyz\rangle$ states in terms of $|m_F\rangle$ states. We then fit the populations to the eigenstates of the Equation 6.1 with Ω and Δ as free parameters. Figure 2 is an example of such type of calibration.

For an antenna with a high quality factor such as ours ($q \sim 20$) we could not ‘suddenly’ turn Ω on or off as it takes some time for power to build up and to die out

when the RF fields are turned on or off. If we did not include this into the model used to calibrate Ω we could get some results that were slightly off. In the end we only used this measurements as initial estimates and once we found an antenna design that could produce a large enough Ω we used the spectroscopy techniques described in next section to fully characterize the system.

6.6 Spectroscopy

We confirmed our control and measurement techniques spectroscopically by measuring the energy differences between the $|xyz\rangle$ states with an additional probing field with angular frequency $\omega + \omega_p$, coupling strength Ω_p and polarized along \mathbf{e}_y . In the frame rotating with angular frequency ω and after using a RWA the system was described by the Hamiltonian

$$\begin{aligned}\hat{H} = & \Delta\hat{F}_z + \hbar\epsilon(\hat{F}_z^2/\hbar^2 - \hat{\mathbb{I}}) + \Omega\hat{F}_x \\ & + \Omega_p (\sin(\omega_p t)\hat{F}_x + \cos(\omega_p t)\hat{F}_y).\end{aligned}\quad (6.7)$$

In this rotating frame the probe field initially polarized along \mathbf{e}_y has components along \mathbf{e}_x and \mathbf{e}_y , resulting in at least one non-zero transition matrix element for all transitions between pairs of dressed states. If the probing field was polarized along \mathbf{e}_z we would not be able to drive the zy transition as can be seen from the matrix elements in Equation 6.6.

To probe the dependence on detuning of the $|xyz\rangle$ state energies, we pulsed Ω_p on for a constant time and scanned ω_p for different values of Δ . Figure 1b shows

the spectroscopically resolved values of $\omega_{xy}/2\pi$, $\omega_{yz}/2\pi$, and $\omega_{zx}/2\pi$ for $\Omega/2\pi = 194.5(1)$ kHz and the side panel shows a sample spectra measured with coupling strength $\Omega_p/2\pi \approx 1$ kHz and $\Delta/2\pi \approx 9$ kHz. The dashed curves were computed by diagonalizing Equation 6.1, and they clearly depart from our measurements for the zx transition. This departure results from neglecting the weak dependence of the quadratic shift ϵ on bias field B_0 . In near-perfect agreement with experiment, the solid curves from the full Breit-Rabi expression account for this dependency.

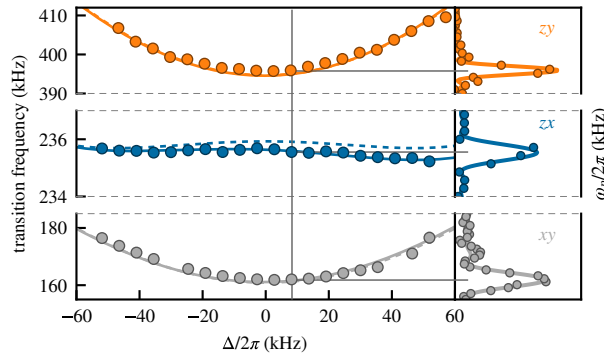


Figure 5: Left: spectroscopic data showing transitions between the $|xyz\rangle$ states for $\Omega/2\pi = 194.5(1)$ kHz. The vertical scale of the center panel (zx transition) has only 10% the range of the other panels. The dashed lines correspond to the Hamiltonian of Equation 6.1 while the solid lines include the dependence of the quadratic shift on Δ . Right: representative spectra.

6.7 Robustness

To characterize the robustness of the $|xyz\rangle$ states, we focus on the zx transition which can be made virtually independent of magnetic field variations due to the similar curvature of $\omega_z(\Delta)$ and $\omega_x(\Delta)$ (see the middle panel of Figure 1b). We quantified the sensitivity of this transition to field variations with three methods corresponding to the different markers in Figure 6b: (1) Triangles denote data using

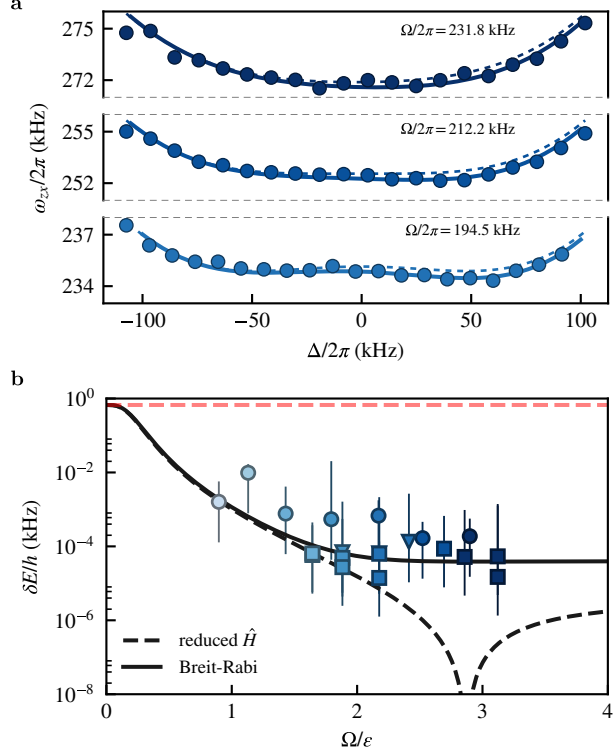


Figure 6: **a.** Transition frequency $\omega_{zx}/2\pi$ for three values of $\Omega/2\pi$. The dashed curves correspond to Equation 6.7, while the solid curves use the Breit-Rabi expression. **b.** The change in energy from our experimental detuning fluctuations as measured in the $|m_F\rangle$ basis is $\delta\Delta/2\pi = 0.67$ kHz (red dashed line). Triangles correspond to $|xyz\rangle$ spectroscopy data, squares to side-of-peak π -pulse data, and circles to double-dressed data. The black dashed (solid) curve was calculated using Equation 6.7 (the Breit-Rabi expression). The shading of the data points corresponds to the Rabi frequencies in Figure 8.

full spectroscopic measurements similar to Figure 6a. (2) Squares denote data in which a detuned π -pulse of the probe field transferred approximately half of the atoms from $|z\rangle$ to $|x\rangle$. This ‘side-of-peak’ technique overcomes the limitation of Rabi spectroscopy being first-order insensitive to changes in ω_{zx} . (3) Circles describe data using a double dressing technique that will be described in Section 6.9. In each case we measured the energy shift from resonance as a function of detuning (magnetic field) and then used a fourth order polynomial fit to extract the rms residuals $\delta\omega_{zx}$

due to the known detuning noise ². The results are not consistent with the theory simple from Equation 6.7 (dashed) and instead require the Breit-Rabi expression (solid) to obtain full agreement ³.

Even at our smallest coupling $\Omega/2\pi = 69(1)$ kHz the typical magnetic field noise was attenuated by two orders of magnitude, rendering it essentially undetectable. Ideally, the radius of curvature of $\omega_{zx}(\Delta)$ changes sign at about $\Omega/2\pi = 220$ kHz, leaving only a Δ^4 contribution, however, in practice the small dependence of ϵ on B prevents this perfect cancellation.

6.7.1 Optimal response to noise

The sensitivity of the zx transition to detuning fluctuations can be optimized further by working at $\Delta \neq 0$ as shown in Figure 7. This behavior can only be captured by including the dependence of the quadratic shift on Δ as given by the Breit-Rabi expression.

For small values of Ω the optimum value of Δ corresponds to one of the concave features of the zx transition energy that arise due to the asymmetry introduced by the quadratic shift. As Ω gets larger, these features merge into a single one and the optimum value is $\Delta \approx 0$. The deviation from $\Delta = 0$ is due to an overall tilt of the transition energy coming from the dependence of the quadratic shift on Δ . At the optimum point $\Omega/\epsilon \approx 3$ the sensitivity of the synthetic clock transition is

²Our procedure also quantifies the small fluctuations that survive for spectra that are flat beyond second order, as in Equation 6.1.

³The fluctuations can be even smaller for a given Ω if we allow for $\Delta \neq 0$.

1.9×10^{-7} kHz, c.f, the ^{87}Rb clock transition which scales as 57.5 kHz/mT² and gives 5.8×10^{-7} kHz.

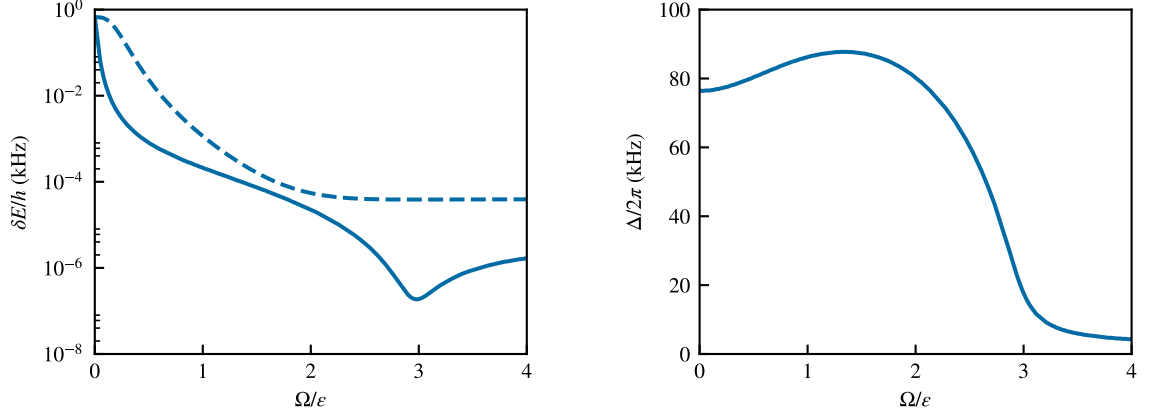


Figure 7: Left: The optimum response (solid) of the zx transition to detuning fluctuations allowing for finite Δ compared to $\Delta = 0$ (dashed) for the full Breit-Rabi model. Right: The values of Δ that correspond to the minimum derivative of ω_{zx} .

6.8 Driving dressed state transitions

We explored the strength of the probe-driven transitions between these states by observing coherent Rabi oscillations (Figure 8a) where our BEC was prepared in $|z\rangle$ and the probe field had strength $\Omega_p/2\pi \approx 1$ kHz. The top panel shows Rabi oscillations between $|m_F = 0\rangle$ and $|m_F = -1\rangle$ states for reference, and the remaining panels show oscillations between $|z\rangle$ and $|x\rangle$. The observed Rabi frequency between dressed states decreased with increasing Ω indicating a dependence of the zx transition matrix elements on Ω . We repeated this experiment driving all possible pairs of dressed state transitions at fixed Ω_p for, and Figure 8b shows the dependence of these matrix elements on Ω for $\Delta = 0$.

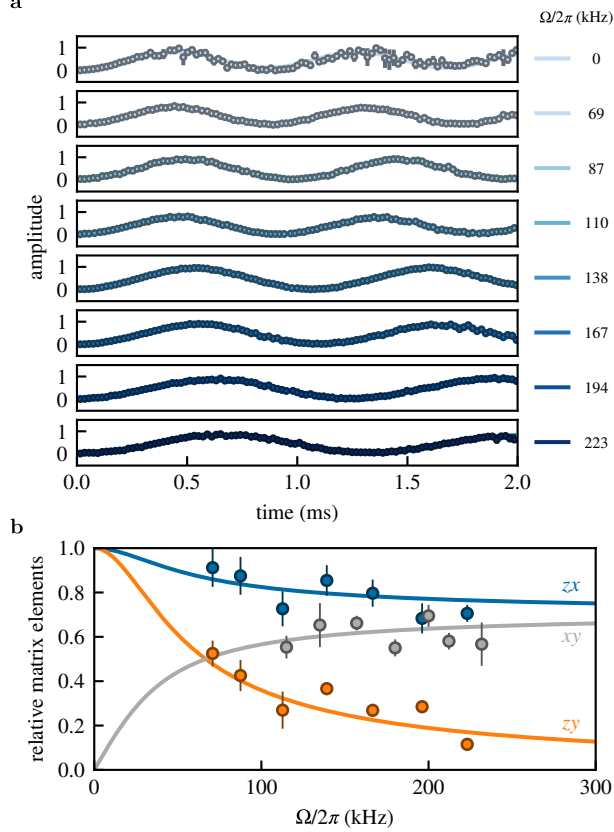


Figure 8: **a.** Rabi oscillations. Phase coherence is maintained throughout the oscillations in the dressed basis, while it is quickly lost in the $|m_F\rangle$ basis. The marker size reflects the typical uncertainties on the dressed basis oscillations. **b.** Transition matrix elements for zx (blue) and zy (orange) transitions decrease monotonically with increasing Ω for $\Delta = 0$, while they increase for xy .

The coherence of the Rabi oscillations for longer times was limited by gradients in Ω that lead to phase separation of the dressed states, and therefore loss of contrast in the oscillations. This effect was faster for smaller frequency Rabi oscillations. For example for $\Omega_p/2\pi = 5$ kHz we observed coherent Rabi oscillations with almost full contrast for more than 10 ms while for the $\Omega_p/2\pi = 870$ Hz oscillation shown in Figure 9 the contrast was significantly reduced after 5 ms. The loss of contrast was even worse when we tried performing a Ramsey sequence where the time evolution is most sensitive to the environment. One solution to this problem would be to change

the experimental setup to a double loop antenna to generate a more spatially uniform magnetic field.

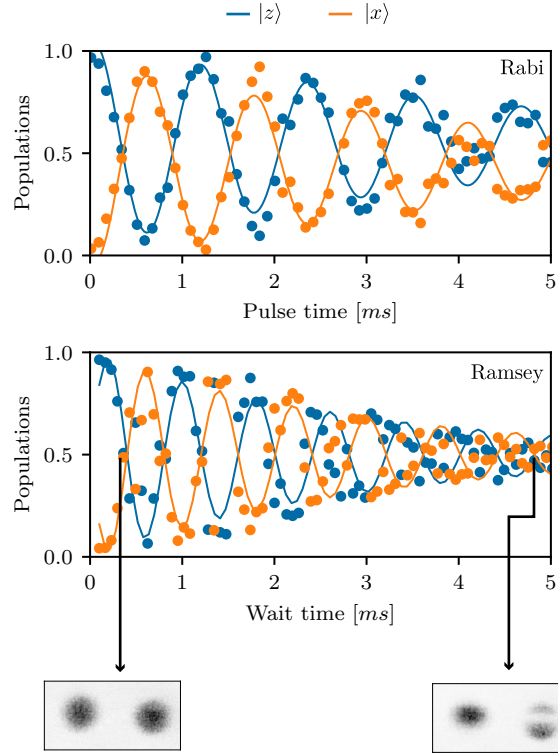


Figure 9: Loss of contrast in coherent oscillations. A Rabi oscillation (top) between the $|z\rangle$ and $|x\rangle$ states with $\Omega_p/2\pi = 870$ Hz decays by $1/e$ in 4.6 ms and a Ramsey oscillation (middle) with about 1 kHz frequency decays in about 3 ms. The gradients in Ω lead to phase separation of dressed states and loss of contrast for longer pulse/wait times.

In comparison, we found that for both Rabi and Ramsey oscillations between the $|m_F\rangle$ states the phase started deteriorating after a few hundreds of μ s, this is not surprising due to bias magnetic field temporal noise. We cancelled gradient magnetic fields so that no phase separation of the bare states was observed for > 10 sec. As a result, the system can in principle undergo coherent evolution without loss of contrast for a long time but because of field fluctuations between shots what we actually observe is full contrast noise.

6.9 Concatenated CDD

The driving field Ω coupled together the $|m_F\rangle$ states, giving us the $|xyz\rangle$ synthetic clock states that were nearly insensitive to magnetic field fluctuations. However, the spectrum of these states is first-order sensitive to fluctuations $\delta\Omega$ of the driving field. Reference [68] showed that an additional field coupling together with these $|xyz\rangle$ states can produce doubly-dressed states that are insensitive to both $\delta\Omega$ and $\delta\Delta$: a process called concatenated CDD. In our experiment, the probe field provided the concatenating coupling field. Because $\Omega_p \ll \Omega$, we focus on a near-resonant two-level system formed by a single pair of dressed states, here $|z\rangle$ and $|x\rangle$, which we consider as pseudospins $|\uparrow\rangle$ and $|\downarrow\rangle$. These are described by the effective two-level Hamiltonian

$$\hat{H}_p = \frac{\hbar\Delta'}{2}\hat{\sigma}_3 + \hbar\Omega' \cos(\omega_p t)\hat{\sigma}_1, \quad (6.8)$$

with energy gap $\Delta' \approx \omega_{z,x}$ (shifted by off-resonant coupling to the zy and xy transitions) and coupling strength $\Omega' \propto \Omega_p$, as set by the matrix elements displayed in Figure 8b. Here $\hat{\sigma}_{1,2,3}$ are the three Pauli operators.

We perform a second transformation into a frame rotating with angular frequency ω_p and use a RWA to compute the eigenenergies of Equation 6.8. For large values of Ω' the energies take the values $E_{\uparrow,\downarrow} \approx \pm\Omega'/2 + (\Delta')^2/2\Omega'$. Even though $E_{\uparrow,\downarrow}$ are still first order sensitive to Ω because $\Delta' \approx \omega_{z,x} \propto \Omega$, its effect is suppressed by a factor of $1/\Omega'$. Thus, the concatenated CDD field protects from the fluctua-

tions $\delta\Delta'$ of the first dressing field in a similar way that CDD provided protection from detuning noise $\delta\Delta$. Table 6.1 summarize the dependence of the $|xyz\rangle$ and $|\uparrow\downarrow\rangle$ energies on Δ , Ω and Ω' .

Table 6.1: Energies of the CDD and CCDD states as a function of Δ , Ω and Ω' . The dependence on parameters not relevant to the expansion is given by the functions f_1 , f_2 , g_1 and g_2 .

	CDD	concatenated CDD
Δ dependence	$f_1(\epsilon, \Omega)\Delta^2$	$f_2(\Omega, \epsilon)\frac{\Delta^2}{\Omega'}$
Ω, Ω' dependence	$\Omega + g_1(\Delta, \epsilon)\frac{1}{\Omega}$	$\left[\Omega^2 + \epsilon\Omega + g_2(\Delta, \epsilon)\frac{1}{\Omega}\right]\frac{1}{\Omega'}$

We produced doubly-dressed states by doing (one more!) ARP sequence. We initialized the system in the $|\downarrow\rangle$ state with RF coupling strength Ω_i . We set the probe frequency to be ~ 20 kHz off resonant with respect to the $|\downarrow\rangle \rightarrow |\uparrow\rangle$ transition and ramped it on in 10 ms. We then ramped $\Omega_i \rightarrow \Omega_f$ in 30 ms. The experimental sequence can be visualized in Figure 10. We chose the value of Ω_f such that it would bring ω_p to resonance at $\Delta = 0$, creating double dressed states that were equal superposition of $|\downarrow\rangle$ and $|\uparrow\rangle$. We quantified the sensitivity of this transition to large changes in the detuning Δ in terms of the fractional population imbalance $\langle\hat{\sigma}_3\rangle = P_\downarrow(\Delta) - P_\uparrow(\Delta)$, shown in Figure 11a for $\Omega_f/2\pi = 138.2(1)$ kHz ⁴. This signal is first-order sensitive to $\omega_{\downarrow,\uparrow}$, and provided our third measurement of sensitivity to detuning in Figure 6b denoted by circles.

We compared the fidelity of preparing a superposition of the $|\downarrow\rangle$ and $|\uparrow\rangle$

⁴We chose the maximum value of Δ such that the population of $|y\rangle$, was negligible after de-loading.

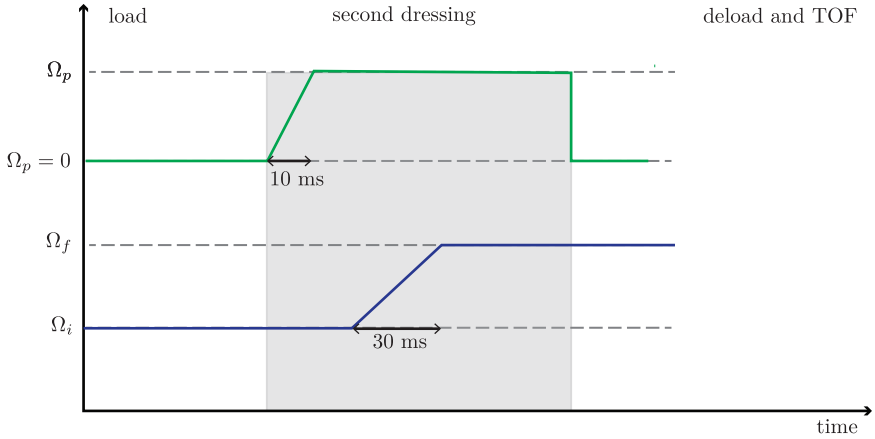


Figure 10: Experimental protocol for implementing concatenated CDD. We started an initial RF coupling strength Ω_i and ramped on the probe field Ω_p in a few ms with $\omega_p = \omega_{z,x}(\Omega_f)$ so that it was initially slightly off resonant with the zx transition. We then ramped the the RF field to Ω_f , brining ω_p to resonance.

states to adiabatically preparing a similar superposition of the the $|m_F = 0\rangle$ and $|m_F = -1\rangle$ states using a single ARP (no dressed states involved), both with a probe field strength of ≈ 1 kHz. Figure 11b shows the rms deviation of the population imbalance measured over a few hundred repetitions of the experiment. The rms deviation for the dressed basis is $0.024(1)$ and is and order of magnitude smaller than for the $|m_F\rangle$ basis $0.29(1)$, where it practically impossible to prepare a balanced superposition for the parameters used here ⁵.

Figure 11c shows the response of the $|\downarrow\rangle \rightarrow |\uparrow\rangle$ transition to small changes $\delta\Omega$ for different values of Ω_p . We prepared an equal superposition of $|\downarrow\rangle$ and $|\uparrow\rangle$ following the same procedure as before for $\Omega_f/2\pi = 138.2(1)$ kHz. We then measured how the population imbalance changes for small variations of Ω — the effective detuning in the ‘twice-rotated frame’ — for different probe amplitudes Ω_p . We

⁵In Figure 11b, the noise in the $|m_F\rangle$ basis is not Gaussian distributed as is typical of line noise in these experiments.

defined a sensitivity parameter $d\langle \hat{\sigma}_3 \rangle / d\Omega$, obtained from the linear regime of the population imbalance measurements (see inset in Figure 11c). The robustness of the doubly-dressed states against $\delta\Omega$ fluctuations increased with Ω_p , thus verifying the concatenating effect of CDD in the $|xyz\rangle$ basis.

However promising the application of multiple concatenating fields might seem, this procedure has a fundamental limitation. Each time a new coupling field is applied the energies of the dressed states are reduced to something on the order of magnitude of the applied concatenating field. For example, in the experiments we have described here we started with $|m_F\rangle$ with transition frequencies on the order of MHz. The transition frequencies of the $|xyz\rangle$ states are reduced to hundreds of kHz (or in general the magnitude of Ω). After applying the second concatenating RF field the transition frequencies of the $|\Downarrow\uparrow\rangle$ are of the order of Ω_p which needs to be smaller than Ω in order for the second RWA to be valid. Therefore we see that after applying multiple concatenating fields we are at the risk of having some very robust states that are also very closely spaced in energy which might not be desirable for some applications.

6.10 Conclusions

We realized a three-level system that is dynamically decoupled from low-frequency noise in magnetic fields, measured now-allowed transitions between all three states, and demonstrated control techniques for creating arbitrary Hamiltonians. These techniques add no heating or loss mechanisms, yet within the protected

subspace retain the full complement of cold-atom coherent control tools such as optical lattices and Raman laser coupling, and permit new first-order transitions that are absent in the unprotected subspace. These transitions enable experiments requiring a fully connected geometry as for engineering exotic states, e.g., in cold-atom topological insulators, and two-dimensional Rashba spin-orbit coupling in ultracold atomic systems [57, 82].

The synthetic clock states form a decoherence-free subspace that can be used in quantum information tasks where conventional clock states might be absent, or incompatible with other technical requirements [83]. Moreover, their energy differences are proportional to the amplitude of the dressing field, and hence tunable, so they can be brought to resonance with a separate quantum system. The effective quantization axis can be arbitrarily rotated so that the two systems can be strongly coupled, pointing to applications in hybrid quantum systems [84, 85]. Introducing a second coupling field shields the system from fluctuations of the first, a process which can be concatenated as needed. More broadly, synthetic clock states should prove generally useful in any situation where fluctuations of the coupling field can be made smaller than those of the environment.

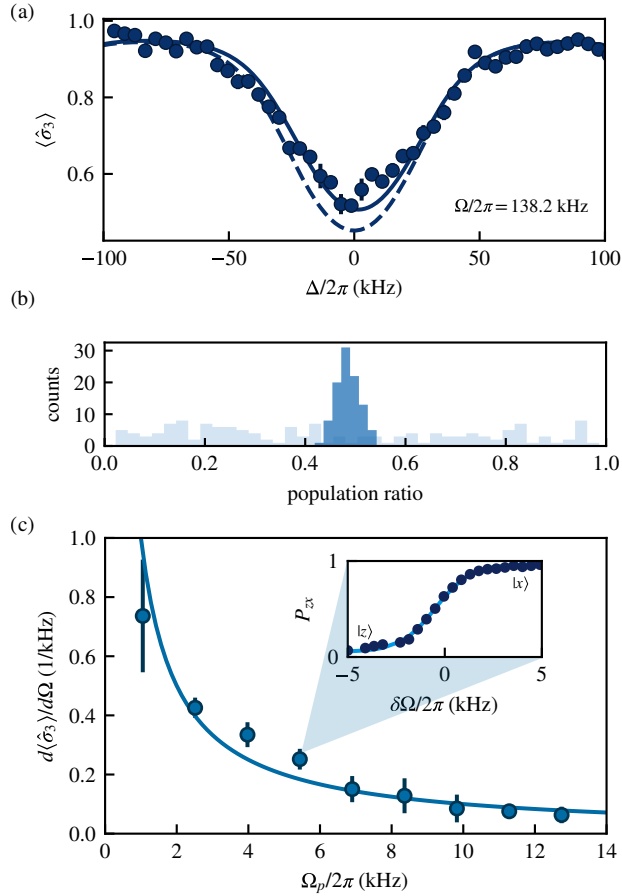


Figure 11: (a) The fractional population imbalance of the $\downarrow\uparrow$ transition for $\Omega/2\pi = 138.2(1)$ kHz over detuning Δ . The dashed curve is calculated using Equation 6.7 and the solid one using the full Breit-Rabi expression. (b) The fidelity of preparing a balanced superposition of $|\downarrow\rangle$ and $|\uparrow\rangle$ (dark blue) states compared to $|m_F = 0\rangle$ and $|m_F = -1\rangle$ states (light blue). (c) The robustness of \downarrow, \uparrow transition against fluctuations $\delta\Omega$ for different probe field coupling strengths. The points represent the slope of the fitted curves to the fractional population imbalance (inset).

Chapter 7: Topological order in quantum systems

Topological order can be found in a wide range of physical systems, from crystalline solids [86], photonic meta-materials [87] and even atmospheric waves [88] to optomechanic [89], acoustic [90] and atomic systems [91]. Topological systems are a robust foundation for creating quantized channels for transporting electrical current, light, and atmospheric disturbances. These topological effects can be quantified in terms of integer-valued invariants such as the Chern number, applicable to the quantum Hall effect [92, 93], or the \mathbb{Z}_2 invariant suitable for topological insulators [94].

The topology of Bloch bands defines integers that serve to both classify crystalline materials and precisely specify properties, such as conductivity, that are independent of small changes to lattice parameters [86]. Topologically non-trivial materials first found application in metrology with the definition of the von Klitzing constant as a standard of resistance, which is now applied in the realization of the kilogram [95]. Today, topological systems have found applications in the engineering of low loss optical waveguides [87] and present a promising path to quantum computation [96]. [Not sure if I want to keep this paragraph as it is.]

We got interested in topology when working on engineering Rashba [27] type spin-orbit coupling in the lab. Our system had non-trivial topology but it broke from

the usual mold of topological materials as it didn't have an underlying crystalline structure that conventionally yields to integer Chern numbers.

Before describing our experiments that characterize the unconventional topology of a Rashba spin-orbit coupled gas, in this Chapter I take a step back to describe the basic concepts of topology and its applications to the band theory of solids. The ideas of topology and how exactly one can connect donuts with band structures might feel a bit obscure and complicated for non-experts in the field. I wrote this Chapter with that in mind, with the hope that it can be followed by non-experts and provide some insight and intuition about this field. The concepts introduced in this Chapter will be necessary for understanding the results presented in Chapter 8.

7.1 Topology in mathematics

Topology is a branch of mathematics that studies continuity [97]. The most familiar example might be that of objects being continuously deformed into one another. For example, a donut can be continuously deformed into a coffee mug but if we want to deform it into a pretzel we need to poke more holes in it. This gives us some intuition that the donut and the mug must share the same topology, which is different from that of the pretzel. Topology also studies more abstract objects but I will limit the discussion to closed two-dimensional surfaces in three dimensions, which will be enough to provide some intuition when we define topological invariants for band structures in the following sections.

The topology of 2D surfaces can be classified by the Euler characteristic, and it

is related to the local Gaussian curvature of a surface by the Gauss-Bonet theorem. The Gaussian curvature can be interpreted in the following way: at any point in a surface we can find a normal vector which is orthogonal to the tangent plane of the surface. We can then define a family of planes containing the normal vector and their intersection with the surface defines a family of curves. The curvature of any of these curves at the point where the planes intersect, which is equal to the quadratic coefficient in a Taylor expansion around that point, is called the normal curvature κ . When we consider all the normal curvatures, the minimum and maximum of these are called the principal curvatures and are used to define the Gaussian curvature at any point of a surface $K = \kappa_{min}\kappa_{max}$ [97]

The Gauss-Bonnet theorem states that the integral of the local Gaussian curvature over the whole surface is equal to the integer valued Euler characteristic

$$\chi = \frac{1}{2\pi} \int_S K dA, \quad (7.1)$$

which is related to the genus g (number of holes or handles in the surface) by $\chi = 2(1 - g)$. The Gauss-Bonnet theorem is a very powerful result as it relates the local properties of a surface, the Gaussian curvature, with a global topological invariant, the Euler characteristic. [Add picture to describe principal curvatures?]

In the following sections I will introduce topological invariants in the context of condensed matter physics, which even though might seem a bit more abstract, their interpretation can be closely related to the concepts just defined in this section.

7.2 Topological order in condensed matter

Just like topology classifies properties of geometric objects, one important task of condensed matter physics has been to classify phases of matter. Many of these phases, for example magnetic or conducting phases, can be described in terms of order parameters related to spontaneously broken symmetries [98]. However, in the past few decades and increasing number of systems have been found where it is only possible to understand their phases and properties in terms of the underlying topology of their quantum states. This new paradigm of physics has been so important that in 2016 the Nobel prize in physics was awarded to David J. Thouless, F. Duncan M. Haldane and J. Michael Kosterlitz for the theoretical discoveries of topological phase transitions and topological phases of matter

The effects of topology in condensed matter systems were first observed when von Klitzing and colleagues [99] measured the quantized Hall resistance in two-dimensional electron gases subjected to a strong perpendicular magnetic field. The effect can be understood semi-classically by thinking of the electrons' quantized cyclotron orbits¹ that give rise to Landau levels. If the Landau levels are filled then there is an energy gap separating two consecutive levels and the material acts as an insulator but if an electric field is applied the orbits drift and the electrons will be 'skipping orbits' in the edge as can be seen in Figure 1, giving rise to what is known as edge states.

¹This is an intuitive but not very complete explanation of the quantum Hall effect, see [100] if you want to learn more about this subject.

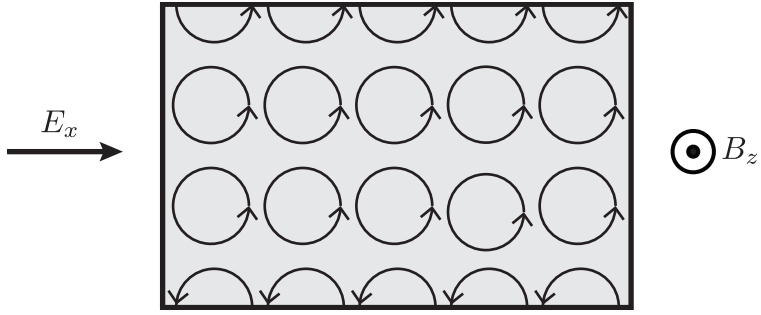


Figure 1: The quantum Hall effect. An electron gas is confined in a two-dimensional material and a strong magnetic field is applied perpendicular to the plane. The electrons on the bulk travel in cyclotron orbits while the electrons on the edge travel ‘skipping orbits’.

In a seminal paper Thouless, Kohomoto, Nightingale, and den Nijs [92] explained that the quantization of the Hall conductivity is determined by the underlying topology of the band structure. Just like the Euler characteristic defined in Equation 7.1 classifies 2D solids that can be continuously deformed without opening or closing holes, there is a topological invariant that classifies band structures that can be deformed into one another without opening or closing an energy gap. This invariant, initially known as the ‘TKNN invariant’, was later recognized by the mathematical physicist Barry Simon as the ‘first Chern class invariant from $U(1)$ fiber bundles’ [101]² and the TKNN invariant became what is known today as the Chern number or Chern invariant. Another very valuable contribution from Simon’s work was that he made the connection between the Chern number and the Berry’s geometrical phase [103] which will be defined in the following sections and will allow us to make a physical interpretation of this otherwise abstract seeming topological

²See [102] if you want to dive into hardcore topology.

invariant.

7.3 Berry phase and Berry curvature

A Berry or geometric phase is used to describe the phase acquired by a quantum state as it moves through a closed trajectory in parameter space. It plays a key role in topological band theory and can help provide a physical interpretation of the Chern number.

Consider a Hamiltonian \hat{H} that depends on a set of parameters $\mathbf{r} = (r_1, r_2, \dots)$. If the parameters are slowly changed in time, the corresponding change in the system can be described by a path in parameter space $\mathbf{r}(t)$. The state $|\psi(t)\rangle$ evolves according to the time dependent Schrödinger equation and at any given time t there is a basis that satisfies

$$\hat{H}(\mathbf{r}) |n(\mathbf{r})\rangle = E_n(\mathbf{r}) |n(\mathbf{r})\rangle \quad (7.2)$$

for $\mathbf{r} = \mathbf{r}(t)$. Suppose the system is initially in state $|n(\mathbf{r}(t=0))\rangle$, if the parameters are changed slowly such that the adiabatic theorem is valid, then at time t the state of the system can be written as

$$|\psi(t)\rangle = \exp \left\{ -\frac{i}{\hbar} \int_0^t dt' E_n(\mathbf{r}(t')) \right\} \exp(i\gamma_n(t)) |n(\mathbf{r}(t))\rangle, \quad (7.3)$$

where the first exponential term corresponds to a dynamical phase factor, and the second term is a geometric phase. By imposing that $|\psi(t)\rangle$ satisfies the time-

dependent Schrödinger equation one finds that

$$\gamma_n(t) = i\langle n(\mathbf{r}) | \nabla_{\mathbf{r}} n(\mathbf{r}) \rangle \cdot \dot{\mathbf{r}}(t), \quad (7.4)$$

where the term

$$\mathbf{A}_n(\mathbf{r}) = i\langle n(\mathbf{r}) | \nabla_{\mathbf{r}} n(\mathbf{r}) \rangle \quad (7.5)$$

is usually referred to as the Berry connection³ or the Berry vector potential for reasons that will become apparent. Because eigenvectors can only be defined up to a global phase, \mathbf{A} is a gauge dependent quantity. If we make a gauge transformation such that $|n(\mathbf{k})\rangle \rightarrow e^{i\xi(\mathbf{k})} |n(\mathbf{k})\rangle$ then the Berry connection is also transformed as $\mathbf{A}_n(\mathbf{k}) \rightarrow \mathbf{A}_n(\mathbf{k}) - \nabla_{\mathbf{k}}\xi(\mathbf{k})$. However if we integrate the Berry connection on a closed loop

$$\gamma_n(\mathcal{C}) = \oint_{\mathcal{C}} \mathbf{A}_n(\mathbf{r}) \cdot d\mathbf{l}, \quad (7.6)$$

we obtain the Berry phase which, unlike the Berry connection, is gauge independent (modulo 2π).

An alternative way to compute Berry's phase uses Stokes's theorem from vector calculus

$$\begin{aligned} \oint_{\mathcal{C}} \mathbf{A}_n \cdot d\mathbf{l} &= \int_{\mathcal{S}} \nabla \times \mathbf{A}_n \cdot d\mathbf{S} \\ &= \int_{\mathcal{S}} \boldsymbol{\Omega}_n \cdot d\mathbf{S}, \end{aligned} \quad (7.7)$$

³This is related to the connection defined in differential geometry that is used to describe things like parallel transport.

where the vector field $\Omega_n = \nabla \times \mathbf{A}_n$ is known as the Berry curvature or Berry fieldT.

By rewriting the Berry phase in this way, its resemblance with the definition of the Euler characteristic from Equation 7.1 becomes apparent.

Using some vector calculus identities the Berry curvature can be rewritten as

$$\begin{aligned}\Omega_n &= i[\nabla_{\mathbf{r}} \langle n |] \times [\nabla_{\mathbf{r}} |n \rangle] \\ &= \sum_{j \neq n} i[\langle n | \nabla_{\mathbf{r}} |j \rangle] \times [\langle j | \nabla_{\mathbf{r}} |n \rangle] \\ &= i \sum_{j \neq n} \frac{\langle n | \nabla_{\mathbf{r}} \hat{H} |j \rangle \times \langle j | \nabla_{\mathbf{r}} \hat{H} |n \rangle}{(E_j - E_n)^2},\end{aligned}\tag{7.8}$$

where $\langle n | \nabla_{\mathbf{r}} |j \rangle$ was replaced with $\langle n | \nabla_{\mathbf{r}} \hat{H} |j \rangle / (E_j - E_n)$ by differentiating Equation 7.2. This expression shows that Ω_n is a gauge independent quantity as it does not depend on the derivatives of a particular gauge choice for $|n\rangle$ but rather on $\nabla_{\mathbf{r}} \hat{H}$ which is gauge independent. Also we can see that Ω_n becomes singular when there are degeneracies present in the Hamiltonian, and these degeneracies act as ‘sources’ for the Berry connection. Finally, even though the system may remain in state $|n\rangle$ during the adiabatic evolution, this expression for the Berry curvature makes it explicit that other eigenstates of the Hamiltonian have an influence in the Berry phase acquired.

7.3.1 Aharonov-Bohm phase as an example of a Berry's phase

A familiar example of geometric phases is the Aharonov-Bohm phase [104] gained by electrons moving along closed trajectories around a solenoid. This phase was initially conceived as a way of showing that in quantum mechanics magnetic vector potentials, typically conceived only as mathematical objects, can have a physical effect on the wave function. They considered a coherent electron beam split into two paths around a solenoid that produces a magnetic field \mathbf{B} as shown in Figure 2. Outside the solenoid the magnetic field $\mathbf{B} = 0$, but there can be a non-zero magnetic vector potential such that $\mathbf{B} = \nabla \times \mathbf{A}$. The two beams are later recombined. Even though the electron's trajectories are not modified, when looking at the interference pattern one finds that the two paths acquired different phases, and their difference is remarkably equal to magnetic flux piercing the area enclosed by the electrons path $\Delta\varphi = 2\pi\Phi_B/\Phi_0$, where $\Phi_0 = h/e$ is the flux quantum.

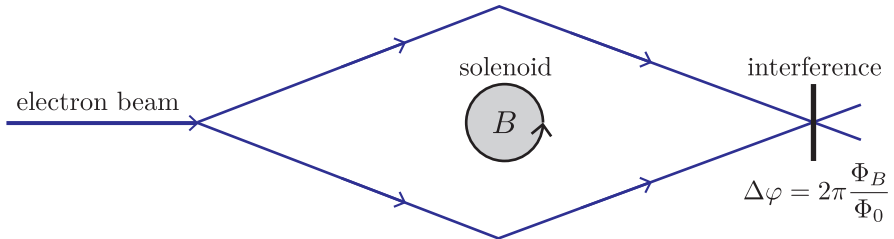


Figure 2: The Aharonov-Bohm experiment. A coherent electron beam is split into two paths surrounding a solenoid which produces a non-zero magnetic field \mathbf{B} inside the gray region and $\mathbf{B} = 0$ outside. The two beams are later recombined and an interference pattern reveals a phase difference $\Delta\varphi = 2\pi\Phi_B/\Phi_0$ equal to the magnetic flux enclosed by the electron's path.

This Aharonov-Bohm phase can be interpreted as an example of a Berry phase

in real space. For a charged particle in the presence of a vector potential the momentum dependence of the free-particle Hamiltonian is modified $\mathbf{p} \rightarrow \mathbf{p} - q\mathbf{A}$ so that the wave function will depend on the magnetic vector potential as well. Using Equations 7.6 and 7.7 it can be shown that the Berry phase associated to a closed path around the solenoid is exactly equal to the Aharonov-Bohm phase:

$$\begin{aligned}\gamma_n(\mathcal{C}) &= \frac{e}{\hbar} \oint_{\mathcal{C}} \mathbf{A}(\mathbf{r}) \cdot d\mathbf{r} \\ &= \frac{e}{\hbar} \int_S \nabla \times \mathbf{A} \cdot d\mathbf{S} \\ &= \frac{e\Phi_B}{\hbar},\end{aligned}\tag{7.9}$$

For this particular example, the Berry connection is exactly equal to the magnetic vector potential and the Berry curvature is the magnetic field. This gives us a very physical intuition for interpreting the Berry phase in terms of the ‘magnetic flux’ from abstract sources of ‘magnetic fields’ in parameter space.

7.3.2 Chern number

The Chern number is conventionally used to describe the topology of materials which have an underlying crystalline structure. According to Bloch’s theorem, the wave functions of a space periodic Hamiltonian can be written as $|\psi(\mathbf{k})\rangle = e^{i\mathbf{k}\cdot\mathbf{r}} |u(\mathbf{k})\rangle$, where $|u(\mathbf{k})\rangle$ are periodic wave functions. If we define the Bloch Hamiltonian

$$\hat{H}(\mathbf{k}) = e^{i\mathbf{k}\cdot\mathbf{r}} \hat{H}(\mathbf{r}) e^{-i\mathbf{k}\cdot\mathbf{r}},\tag{7.10}$$

their eigenvectors are given by $|u(\mathbf{k})\rangle$ and the eigenvalues define the band structure. Translational symmetry implies that $\hat{H}(\mathbf{k} + \mathbf{a}) = \hat{H}(\mathbf{k})$ where \mathbf{a} is a reciprocal lattice vector. The crystal momentum or quasimomentum is only defined within the periodic Brillouin zone and therefore can be mapped into a torus in d dimensions if we glue the edges together.

The Chern number of the n th band is defined as

$$C_n = \frac{1}{2\pi} \int_{BZ} \Omega_n d\mathbf{k}, \quad (7.11)$$

where the relevant parameter space is crystal momentum and the surface of integration corresponds to the BZ (a torus). The definition of Chern number is closely related to the definition of the Berry phase from Equation 7.7. For our previous example of a quantum Hall system, the integer proportionality factor in the quantized conductance is exactly equal to the Chern number.

Just like two-dimensional surfaces are classified by the integral of their Gaussian curvature, the topology of Bloch bands and of quantum systems in general is determined by the integral of the Berry curvature. In a similar way, the integral connects local properties of a quantum system, the Berry connection, with a global topological invariant, the Chern number. One subtle difference is that the Euler characteristic is only determined by the surface (and its intrinsic Gaussian curvature) while the Chern number is defined both by a surface (the BZ) and an additional local curvature (the Berry curvature). By studying different Hamiltonians one can obtain a different Berry curvature, but the geometry of the BZ and thereby

the surface of integration is typically defined by a torus⁴. This difference will be important later on when we describe the experiments performed to study a system with Rashba spin-orbit coupling and an unconventional topology.

7.4 The bulk-edge correspondence principle

Earlier I mentioned that topological systems provide very robust channels for transporting things like electrical current and light. This transport phenomena typically arises when there is a spatial interface between two topologically distinct phases. The electrons skipping orbits at the interface of a (topological) quantum Hall material and (trivial) vacuum are one example of this. Notice that for this particular example the modes propagate along a given direction, they are chiral. In general one can expect to have modes moving along two directions, and the difference between the number of these modes $N_L - N_R$ is fixed and determined by the topology of the bulk states. The bulk-edge correspondence principle relates the difference in the number of these modes with the bulk topology of the materials at the interface:

$$\Delta C = N_R - N_L \quad (7.12)$$

where ΔC is the difference of Chern number on the interface.

⁴In next chapter we consider a case where this breaks down.

7.5 Example: two-level model

Many of the concepts introduced in the previous section can be readily applied and understood using a two-level model

$$\hat{H}(\mathbf{k}) = \mathbf{h}(\mathbf{k}) \cdot \hat{\boldsymbol{\sigma}} \quad (7.13)$$

where $\hat{\boldsymbol{\sigma}} = (\sigma_x, \sigma_y, \sigma_z)$ are the Pauli matrices and $\mathbf{h}(\mathbf{k}) = (h_x(\mathbf{k}), h_y(\mathbf{k}), h_z(\mathbf{k}))$ are functions of \mathbf{k} . This model has been used to describe a number of physical systems like graphene [93] and spin-orbit coupled systems [27, 28]. Let us now consider the simple case $h(\mathbf{k}) = \mathbf{k}$, for which $\nabla_{\mathbf{k}} \hat{H} = \boldsymbol{\sigma}$ and using Equation 7.8 it can be shown that

$$\boldsymbol{\Omega} = -\frac{\mathbf{h}}{2h^3} \quad (7.14)$$

which can be recognized as the field of a Dirac monopole [105] with charge $-1/2$. The degeneracy in the energies that gives rise to the monopole is known as a Dirac point as the energies in that vicinity resemble the dispersion of a massless Dirac particle. It follows from Equation 7.14 that the Berry phase gained by moving in a closed path \mathcal{C} is equal to the flux from the monopole in the surface enclosed by \mathcal{C} as is shown in Figure 3. This connects nicely with our intuition from the Aharonov-Bohm effect. For a closed surface enclosing the Dirac point, the Chern number is an integer equal to 1.

For a Hamiltonian with arbitrary $\mathbf{h}(\mathbf{k})$ we can define a normalized vector

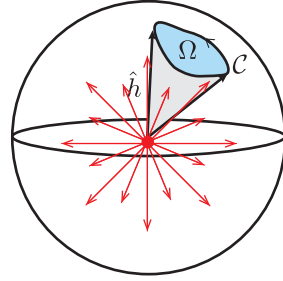


Figure 3: For a two-level system, the Berry curvature from a Dirac point can be viewed as a Dirac monopole in momentum (parameter) space. The Chern number can be interpreted as the flux from the monopole on the solid angle subtended by the vector $\hat{h}(\mathbf{k})$ or alternatively as the number of times $\hat{h}(\mathbf{k})$ wraps around a unit sphere.

$\hat{h} = \mathbf{h}/|\mathbf{h}|$ and the Chern number takes the form

$$C = \frac{1}{4\pi} \int (\partial_{k_x} \hat{h} \times \partial_{k_y} \hat{h}) \cdot \hat{h} d\mathbf{k} \quad (7.15)$$

and can be interpreted as the number of times that the vector $\hat{h}(\mathbf{k})$ wraps around a unit sphere [106], a quantity that is known as the winding number.

7.6 Monopoles and Dirac strings

We just gained some intuition about interpreting the Chern number as the flux from Dirac monopoles. But if we stick to our knowledge of electromagnetism we might remember that monopoles are forbidden since

$$\int_S \mathbf{B} \cdot d\mathbf{S} = \int_V (\nabla \cdot \mathbf{B}) dV \quad (7.16)$$

and $\nabla \cdot \mathbf{B} = \nabla \cdot (\nabla \times \mathbf{A}) = 0$. So how is this possible? The solution to this problem was envisioned by Dirac [105] and is now called a Dirac string. If we consider an semi-infinitely long and infinitesimally thin solenoid, the magnetic field in the finite end will resemble that of a monopole as can be seen in Figure 4. This tiny solenoid corresponds to the Dirac string. A more mathematical interpretation of

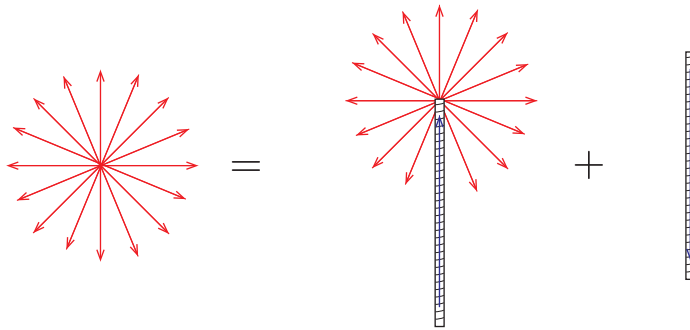


Figure 4: For a two-level system, the Berry curvature from a Dirac point can be viewed as a Dirac monopole in momentum (parameter) space. The Chern number can be interpreted as the flux from the monopole on the solid angle subtended by the vector $\hat{h}(\mathbf{k})$ or alternatively as the number of times $\hat{h}(\mathbf{k})$ wraps around a unit sphere.

these strings comes from the fact that the vector potential of a monopole has ‘lines’ where it becomes singular. For example for a particular gauge we can write

$$\mathbf{A}(\mathbf{r}) = g \frac{-y\mathbf{e}_x + x\mathbf{e}_y}{r(r+z)} \quad (7.17)$$

which is singular for the negative z axis where $z = -r$. The orientation of the Dirac string is gauge dependent, something that should not surprise or bother us at this point. However, the physical effects of the Dirac string should be gauge independent, or in other words, the Aharonov-Bohm phase gained by a charged particle moving

in a path that encloses the string should be an integer multiple of 2π . This is argument gives rise to the Dirac charge quantization [105], and in the context of topology, it guarantees that when we calculate the Berry phase by integrating the Berry connection (vector field) along a path that enclose a Dirac string, its effect will be indistinguishable.

7.7 Conclusions

Topology plays a very important role both in math and in physics. In this Chapter I reviewed the basic concepts of topology in the context of condensed matter physics that will be relevant for our experiments with unconventional topology. As a closing remark, Figure 5 summarizes the main concepts that were introduced and is a reminder that topological invariants are global properties defined in terms of integrals of local properties. Furthermore, we can use our intuition from electromagnetic theory to interpret topological invariants in quantum mechanics.

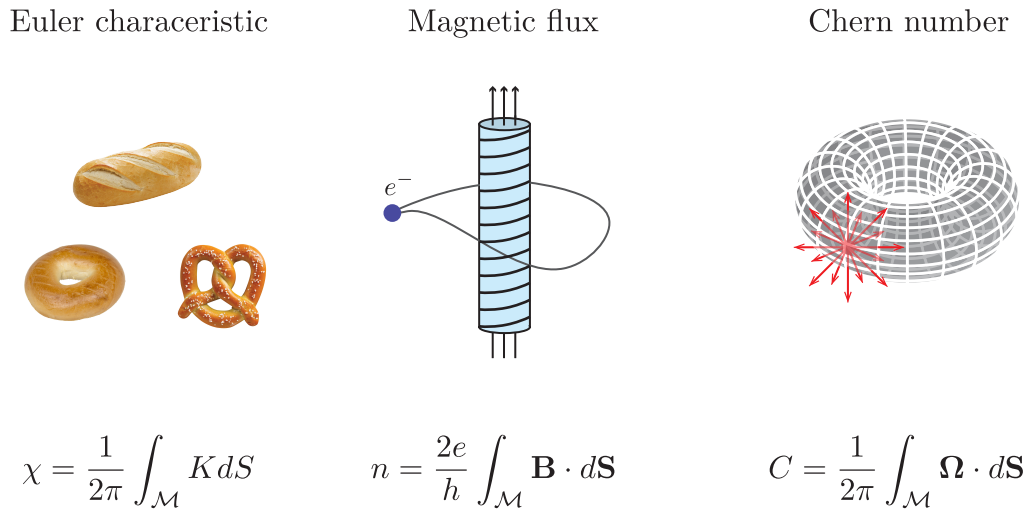


Figure 5: The Euler characteristic and the Chern number are topological invariants defined by integrals of local curvatures. The Aharonov-Bohm phase gives us physical intuition to interpret the Chern number as the flux from a ‘Berry field’.

Chapter 8: Unconventional topology with a Rashba SOC quantum gas

As I mentioned in the previous Chapter topological order is present in a wide range of physical systems and is quantified by integer valued topological invariants such as the Chern number. In this Chapter I describe a system with Rashba-type spin-orbit coupling whose topological invariants can take half-integer values. If the concept of half-integer invariants does not sound odd, think of a donut with half a hole.

Ultracold atomic systems are an emerging platform for engineering topological lattices, from the Harper-Hofstadter model [107, 108], the Haldane model [109], to the Rice-Mele model [110, 111] as well as assembling spin-orbit coupled lattices without analogues in existing materials [112, 113]. However, experimental realizations of topological materials have mostly focused on engineering different topological bands (with different Berry curvatures) in lattice systems, where the BZ is always a torus. Here I show that by eliminating the lattice potential and thereby changing the BZ from \mathbb{T}^2 to \mathbb{R}^2 , i.e. from a torus to a Cartesian plane, it is possible to create topological branches of the dispersion relation with half-integer Chern number.

The experiments presented here combine the experimental techniques that

were presented in Chapters 5 and 6, additionally I use the key concepts of topology described in Chapter 7. This Chapter is organized in the following way: First I give a general overview of Rashba SOC and describe theoretical proposals for engineering this type of coupling in ultracold atom systems. Then I describe our experimental implementation of Rashba SOC in the lab using a trio of Raman coupled CDD states and validate our quantum engineering using Fourier transform spectroscopy. Finally I describe a quantum state tomography procedure to measure the eigenstates of our system, from which we can directly obtain the Chern number.

To avoid confusion between dressed state xyz labels and Cartesian coordinates, in this Chapter I will use the numbers 1, 2, 3 to label the coordinates $\mathbf{e}_x, \mathbf{e}_y, \mathbf{e}_z$ and the letters x, y, z to label clock state parameters.

8.1 Rashba spin-orbit coupling

Rashba SOC [27] appears in condensed matter systems where electrons are confined in a 2D plane and experience an intrinsic out-of-plane electric field. If the electron's momentum is given by $\hbar\mathbf{k} = \hbar(k_x\mathbf{e}_x + k_y\mathbf{e}_y)$ and the electric field is $\mathbf{E} = E\mathbf{e}_z$, in the electron's moving frame there will be a momentum dependent magnetic field $\mathbf{B}_{\text{SOC}} = -\hbar\mathbf{k}/m \times \mathbf{E}/c^2 = \hbar E/mc^2(-k_y, k_x, 0)$. The interaction between the electron's spin with this field through the magnetic Zeeman interaction $-\mu \cdot \mathbf{B}_{\text{SOC}}$ gives rise to the SOC Hamiltonian

$$\hat{H}_{\text{SOC}} = \frac{2\alpha}{m}(k_y\hat{\sigma}_x - k_x\hat{\sigma}_y) \quad (8.1)$$

where $\alpha = g\mu_B E/c^2$, g is the electrons gyromagnetic ratio, μ_B is the Bohr magneton and $\hat{\sigma}_i$ are the Pauli matrices.

A can be seen in Figure 1, the Rashba dispersion relation is characterized by having a Dirac point located at $\mathbf{k} = 0$ (see Section 7.5) and a degenerate ground state that is described by the ring $k_x^2 + k_y^2 = \alpha^2$. If we combine Equation 8.1 with the free particle Hamiltonian the Hamiltonian can be written as $\hat{H} = (\hbar\mathbf{k} - \hat{\mathbf{A}})^2/2m$ where $\hat{\mathbf{A}} = \alpha(\hat{\sigma}_y\mathbf{e}_x - \hat{\sigma}_x\mathbf{e}_y)$ can be interpreted as a (matrix valued) non-Abelian gauge potential [114] whose elements do not commute. This term is closely related to the Berry connection discussed in Section 7.3. This non-Abelian gauge potential in combination with the Dirac point hints at us that a system with Rashba SOC has non-trivial topology.

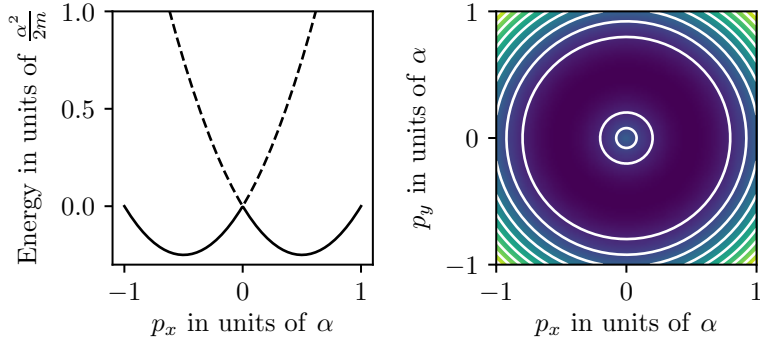


Figure 1: The Rashba dispersion relation has a Dirac point located at $\mathbf{k} = 0$ and a degenerate ground state that is described by the ring $k_x^2 + k_y^2 = \alpha^2$. [TODO: Might be nice to add the ‘hedgehog’ field as well]

SOC is a necessary ingredient for realizing \mathbb{Z}_2 topological insulators and the quantum spin-Hall effect. Furthermore, the degeneracy of the ground state single particle eigenstates could open the possibility of studying strongly correlated phases

in the presence of interactions for systems of both fermions and bosons [115–117].

Using ultracold atomic systems to engineer SOC, and in particular Rashba type SOC, has been a longstanding goal [29].

8.2 Rashba SOC for neutral atoms

Proposals for engineering Rashba type SOC in neutral atoms consist in using lasers to link internal states of an atom with its linear momentum. In order to achieve non-trivial gauge potentials it is necessary to couple $N \geq 3$ levels (see [23]). I will describe the proposal by [118] which considers a ‘ring coupling’ which is shown in Figure 2 for the case of $N = 3$. The states $|j\rangle$ represent internal atomic states and they are linked to each other with complex valued matrix elements $\frac{\Omega_j}{2} e^{i\mathbf{k}_j \cdot \mathbf{x}}$, where \mathbf{k}_j is a momentum transfer associated with the $|j\rangle \rightarrow |j+1\rangle$ transition and $\Omega_i = e^{i\phi_i} |\Omega|$ represents the coupling strength. We require that $\sum \mathbf{k}_i = 0$ so that no momentum is transferred when a closed loop $|1\rangle \rightarrow |2\rangle \cdots \rightarrow |N\rangle \rightarrow |1\rangle$ is completed. For this case the \mathbf{k}_i momenta vectors can be written as $\mathbf{k}_j = \mathbf{K}_{j+1} - \mathbf{K}_j$, and we make $\mathbf{K}_j = k_L \sin(2\pi j/N) \mathbf{e}_x + k_L \cos(2\pi j/N) \mathbf{e}_y$, corresponding to the vertices of an N sided regular polygon. We can further make a gauge transformation such that we can replace the phases ϕ_i associated to each coupling with $\bar{\phi} = \sum_i \phi_i / N$.

The Hamiltonian describing this coupling along with the kinetic term is

$$H_{j,j'} = \frac{\hbar^2 k^2}{2m} \delta_{j,j'} + \frac{\Omega}{2} (e^{i(\bar{\phi} + \mathbf{k}_j \cdot \mathbf{x})} \delta_{j,j'+1} + \text{h.c.}), \quad (8.2)$$

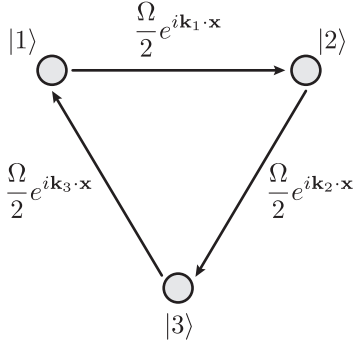


Figure 2: The Rashba ring coupling. To generate Rashba SOC in a system of cold atoms it is necessary to cyclically couple $N \geq 3$ internal states such that the transition $|j\rangle \rightarrow |j+1\rangle$ has a momentum transfer \mathbf{k}_j and $\sum_j \mathbf{k}_j = 0$ such that there is no momentum transfer for a closed loop $|1\rangle \rightarrow |2\rangle \dots |N\rangle \rightarrow |1\rangle$. The ring coupling combined with the free particle Hamiltonian give rise to a 2-level subspace that can be described to first order by the Rashba Hamiltonian

and after applying the unitary transformation $U_{j,j'} = \exp[i\mathbf{K}_i \cdot \mathbf{x}] \delta_{j,j'}$ ¹ it gets transformed to

$$H_{j,j'} = \frac{\hbar^2}{2m} |\mathbf{q} + \mathbf{K}_j|^2 \delta_{j,j'} + \frac{\Omega}{2} (e^{i\bar{\phi}} \delta_{j,j'+1} + \text{h.c.}), \quad (8.3)$$

where I have replaced the momentum \mathbf{k} by the quasimomentum \mathbf{q} . The off diagonal terms of Equation 8.3 can be related to a 1D periodic tight-binding Hamiltonian with hopping elements $\Omega/2$ where the internal states $|j\rangle$ represent lattice sites and completing one loop corresponds to gaining a ‘flux’ of $N\bar{\phi}$. To visualize how the Rashba Hamiltonian emerges from this coupling scheme, it is helpful to write the Hamiltonian in a basis that is conjugate to the index j ²

$$|l\rangle = \frac{1}{\sqrt{N}} \sum_{j=1}^N e^{i2\pi jl/N} |j\rangle \quad (8.4)$$

¹This transformation is equivalent to applying a state dependent momentum boost $\mathbf{k} \rightarrow \mathbf{k} + \mathbf{K}_j$

²Just like position and momentum are conjugate variables related by Fourier transforms, the $|j\rangle$ and $|l\rangle$ basis are related by a discrete Fourier transform.

where the index l is analogous to the crystal momentum index for a Bloch Hamiltonian. In this new basis, terms in the diagonals are displaced to the off-diagonal and likewise terms in the off diagonals are displaced to the diagonal. Under this basis the Hamiltonian starts looking very much Rashba-like

$$H_{l,l'} = \left[\frac{\hbar^2}{2m} (q^2 + k_L^2) + E_l \right] \delta_{l,l'} + \frac{\hbar^2 k_L}{m} [(iq_x + q_y) \delta_{l-1,l'} + \text{h.c.}] , \quad (8.5)$$

where $E_L = 2\hbar\Omega \cos(2\pi l/3 + \bar{\phi})$ correspond to the eigenenergies when $q = 0$. The phase $\bar{\phi}$ can be tuned such that a pair of states with consecutive l index become degenerate, indicating the presence of a Dirac point at $q = 0$. Figure 3 shows the energies E_l for $N = 3$ and $\bar{\phi} = 0$.

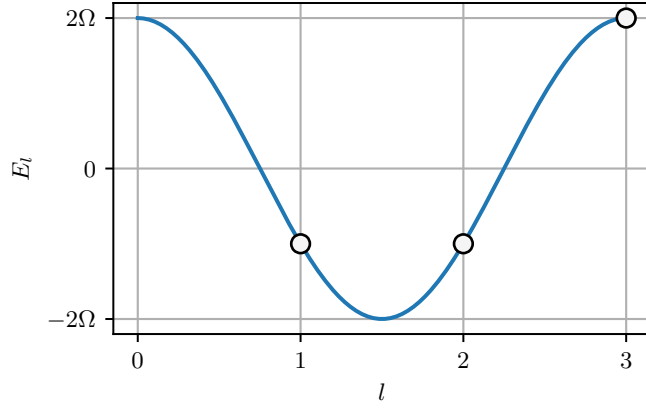


Figure 3: Eigenenergies of Equation 8.5 for $q = 0$ for $N = 3$ and $\bar{\phi} = 0$. For this particular choice of phase, the energies of the $l = 1$ and $l = 2$ states become degenerate

We can consider the degenerate states as pseudospins which are described to

zeroth order by the Rashba plus free particle Hamiltonian

$$\hat{H}^{(0)} = \frac{\hbar^2 q^2}{2m} + \frac{\hbar^2 k_L}{m} (\hat{\sigma}_x q_y - \hat{\sigma}_y q_x), \quad (8.6)$$

with spin orbit coupling strength given by $\alpha = \hbar^2 k_L / 2$. The zeroth-order Hamiltonian has continuous rotational symmetry while the proposed ring coupling only has discrete rotational symmetry. The symmetry of the Hamiltonian is recovered when higher order corrections are added to the Hamiltonian. The complete expressions for the higher order terms for $N = 3$ and $N = 4$ can be found in [118], and they are reminiscent of quadratic and cubic Dresselhaus SOC [119]. The largest leading order term for the $N = 3$ case is inversely proportional to Ω so that this ring-coupling scheme results in a more ‘Rashba-like’ Hamiltonian as one goes to higher coupling strengths. Figure 4 shows level curves of the ground state eigenenergies of Equation 8.5 for $N = 3$ and $\bar{\phi} = 0$ for increasing Ω . At low Ω the dispersion has discrete rotational symmetry and is characterized by three local minima³. As Ω is increased the local minima start merging into each other and in the large Ω limit we recover the characteristic Rashba ring-like dispersion.

8.3 Experimental implementation of Rashba SOC

We implemented the ring-coupling scheme and thereby engineered Rashba SOC by resonantly coupling the $|xyz\rangle$ states from Chapter 6 states using two-photon Raman transitions [57] as depicted in Figure 5. The engineered system consisted

³or... an alien face?

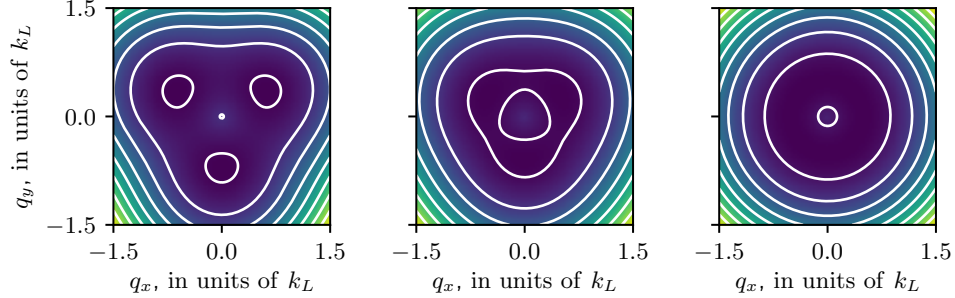


Figure 4: Ground state dispersion relation of Equation 8.5 for $N = 3$ and $\bar{\phi} = 0$ for $\Omega = 1.75 E_L$ (left), $\Omega = 3.5 E_L$ (middle) and $\Omega = 175 E_L$ (right). Higher order corrections to $\hat{H}^{(0)}$ decay as $1/\Omega^2$ and in the large Ω limit we recover the Rashba ring dispersion.

of an effective spin-1/2 Rashba subspace, along with a topologically trivial high-energy branch. Our engineered Rashba system had a single Dirac cone near $\mathbf{q} = 0$, where the two lower dispersion branches become degenerate and the Berry curvature becomes singular. Each of these branches extend to infinite momentum, making the supporting manifold a plane rather than a torus. We characterized this system using both spectroscopy and quantum state tomography. This allowed us to measure the dispersion branches and directly observe the single Dirac point linking the lowest two branches as well as to reconstruct the Berry connection to derive the associated Chern numbers.

All of our experiments started with about $N \approx 1 \times 10^6$ ^{87}Rb atoms in a crossed optical dipole trap [120], with frequencies $(f_1, f_2, f_3) \approx (70, 85, 254)$ Hz, just above the transition temperature for Bose-Einstein condensation. We initially prepared the atoms in the $|F = 1, m_F = -1\rangle$ state of the $5S_{1/2}$ electronic ground state and transferred atoms to the $m_F = 0$ and $m_F = +1$ states as needed using ARP. A bias field $B_0 \mathbf{e}_3$ gave a $\omega_0/2\pi = 23.9$ MHz Larmor frequency along with a

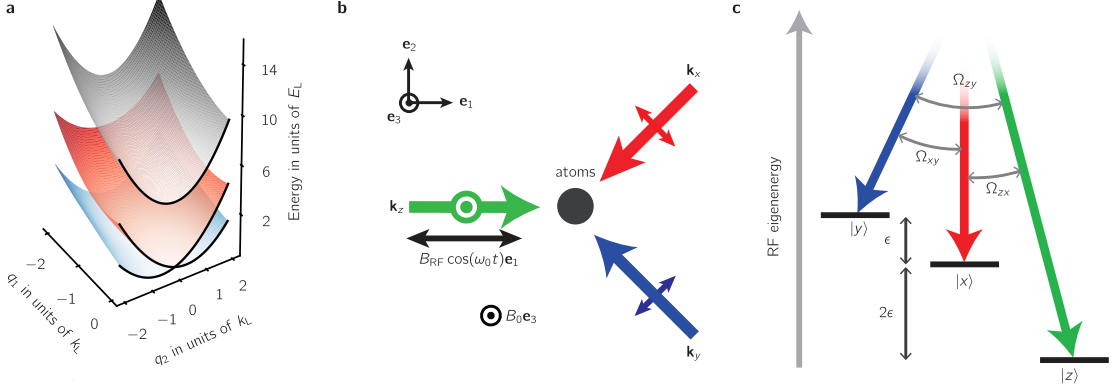


Figure 5: **a** Our engineered dispersion consisted of a two-level Rashba subspace (red and blue) with a single Dirac point linking the lowest two branches and a topologically trivial higher branch (gray). **b** We generated $|xyz\rangle$ states by combining a bias magnetic field along \mathbf{e}_3 with an RF magnetic field oscillating along \mathbf{e}_1 . These states were coupled by three cross-polarized Raman laser beams propagating along \mathbf{e}_1 , $\mathbf{e}_2 - \mathbf{e}_1$ and $-\mathbf{e}_1 - \mathbf{e}_2$. **c** Each pair of Raman lasers was in two-photon resonance with a single transition between the $|xyz\rangle$ states which we coupled strengths $(\Omega_{zx}, \Omega_{xy}, \Omega_{yz})/2\pi = (12.6(5), 8.7(8), 10(1))$ kHz.

quadratic shift of $\epsilon/2\pi = 83.24$ kHz. The RF field used to generate the $|xyz\rangle$ states and implementing CDD had strength $\Omega_{\text{RF}} = 1.41(2)\epsilon$. We adiabatically prepared the $|xyz\rangle$ states starting from the m_F states following the procedure described in Section 6.4.

8.3.1 Raman coupling the $|xyz\rangle$ states

We Raman-coupled atoms prepared in any of the $|xyz\rangle$ states using the three cross-polarized Raman laser beams shown in Figure 5b, tuned to the ‘magic zero’ wavelength $\lambda_L = 790$ nm. We arranged the Raman lasers into the tripod configuration shown in Figure 5c, bringing each pair into two-photon resonance with a single transition with strengths $(\Omega_{zx}, \Omega_{xy}, \Omega_{yz})/2\pi = (12.6(5), 8.7(8), 10(1))$ kHz. The ge-

ometry of our experimental implementation differs from [57] where all Raman lasers are perpendicular. We had to go away from the ideal configuration because we needed all of the Raman recoil vectors to lie on the imaging plane (spanned by \mathbf{e}_1 and \mathbf{e}_2) in order to image all the Raman induced \mathbf{k} dependent dynamics. As a result of this the dispersion relation no longer has discrete rotational symmetry, however the Dirac point is still present in our system. The only way to break the degeneracy of this system is to change the phase $\bar{\phi}$ and for our laser configuration we always have $\bar{\phi} = 0$.

The energies of the $|xyz\rangle$ states are $\omega_x = 0$ and $\omega_{z,y} = -(\epsilon \pm \sqrt{4\Omega_{\text{RF}}^2 + \epsilon^2})/2$. We set the frequencies of the Raman lasers to $\omega_x = \omega_L + \omega_0 + \omega_{xy}$, $\omega_y = \omega_L + \omega_0$ and $\omega_z = \omega_L - \omega_{zx}$, where $\omega_L = 2\pi c/\lambda_L$ and $(\omega_{zx}, \omega_{xy}, \omega_{zy})/2\pi = (166.47, 83.24, 249.71)$ kHz are the transition frequencies between pairs of dressed states and are integer multiples of ϵ for our coupling strength $\Omega = \sqrt{2}\epsilon$.

The Raman coupled states can be described by the combined kinetic and light-matter Hamiltonian

$$\hat{H}_{\text{R}}(\mathbf{k}) = \sum_{j \in \{xyz\}} \left(\frac{\hbar^2 k^2}{2m} + \hbar\omega_i \right) |j\rangle \langle j| + \sum_{j' \neq j} \hbar\Omega_{j,j'} e^{i(\mathbf{k}_{j,j'} \cdot \mathbf{x} - i\omega_{j,j'} t)} |j\rangle \langle j'|, \quad (8.7)$$

where $\mathbf{k}_{j,j'}$ is the recoil momentum from an $|j\rangle \rightarrow |j'\rangle$ transition and Ω_{ij} is the Raman coupling strength between a pair of RF dressed states. The Hamiltonian above only includes the matrix elements associated to resonant couplings. We apply the unitary transformation $\hat{U}_{j,j'} = \exp(-i\mathbf{k}_j \cdot \mathbf{x} - \omega_j t) \delta_{j,j'} |j\rangle \langle j'|$ so that the Hamiltonian takes

the familiar form of the ring coupling scheme

$$\hat{H}_R = \sum_{j \in \{xyz\}} \left(\frac{\hbar^2(\mathbf{q} - \mathbf{k}_j)^2}{2m} + \hbar\delta_j \right) |j\rangle \langle j| + \sum_{j \neq j'} \hbar\Omega_{jj'} |j\rangle \langle j'|, \quad (8.8)$$

where \mathbf{k}_j are the Raman wave vectors and δ_j is the detuning from Raman resonance.

This coupling scheme simultaneously overcomes three limitations of earlier experiments [121, 122] that performed the ring coupling using states in both $5S_{1/2}$ hyperfine manifolds of ${}^{40}\text{K}$: (1) working in the same hyperfine manifold eliminates spin-relaxation collisions [123]; (2) unlike m_F states, the $|xyz\rangle$ states can be tripod-coupled with lasers far detuned relative to the excited state hyperfine splitting greatly reducing spontaneous emission [81]; and (3) CDD renders the $|xyz\rangle$ states nearly immune to magnetic field noise.

8.3.1.1 Floquet and off resonant coupling effects

We operated in a regime where the transition energies between the $|xyz\rangle$ states were integer multiples of ω_{xy} : $\omega_{zx} = 2\omega_{xy}$ and $\omega_{zy} = 3\omega_{xy}$, and therefore we can use Floquet theory for a complete description of our system [124]. We observed that the effective Raman coupling strengths for the driven three level system differed from our calibrations which were performed looking at Rabi oscillations from individual pairs of lasers because of the presence of nearby quasi-energy manifolds and off resonant coupling terms. This effect could be mitigated for larger values of ω_{xy} as the spacing between quasi-energy manifolds is increased and the off resonant coupling terms less relevant. Appendix ?? has a full derivation of the Raman Hamiltonian starting from

the $|m_F\rangle$ basis in the lab frame including the full time dependence and off resonant coupling terms.

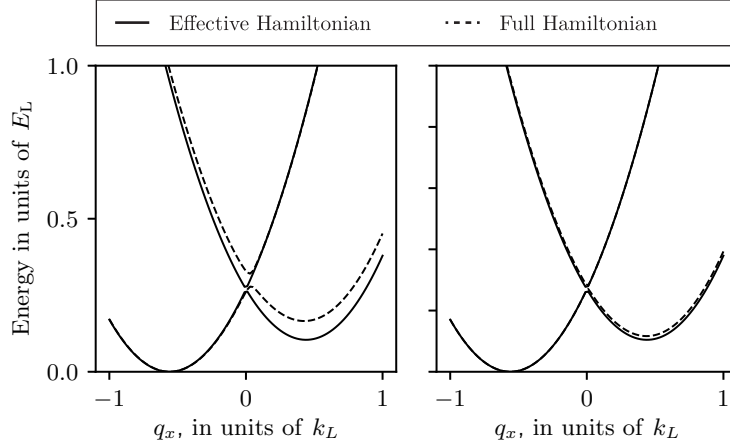


Figure 6: Solid lines: Dispersion relation from RWA Hamiltonian (Equation 8.8) as a function of q_x for $\Omega_{i,j} = 1.5 E_L$ and $\delta_i = 0$. Dashed lines: Dispersion relation computed for the full Floquet Hamiltonian. We considered $\omega_{zx} = 2\omega_{xy}$ and $\omega_{zy} = 3\omega_{xy}$ in both cases so the separation between Floquet manifolds is ω_{xy} . In the left panel $\omega_{xy} = 83.24$ kHz as in our experiments and in the right panel $\omega_{xy} = 416.2$ kHz. As the spacing between Floquet manifolds becomes we get a better agreement between the spectra of the RWA and Floquet Hamiltonians.

8.3.1.2 Lifetime

The limited lifetime due to spontaneous emission has always been a concern for Raman coupled systems. This was in part one of the reasons why we pursued the topology direction rather than trying to measure a fragile many-body phase. The measured spontaneous emission limited lifetime of our system was 320(17) ms, measured with the Raman lasers applied to the m_f states. However, it was reduced to 40(2) ms when we Raman coupled the $|xyz\rangle$ states, which we attribute to technical noise in the relative phase between the RF dressing field and the Raman laser

fields, which has caused considerable consternation in ongoing experiments. All the experiments reported here were short compared to this timescale so this decreased lifetime was not an issue but it is a limitation that needs to be addressed in future experiments. Figure 7 shows measurements of the lifetimes of Raman dressed atoms in both $|m_f\rangle$ and $|xyz\rangle$ states. We obtained the lifetime by fitting decaying exponentials to the integrated OD obtained from absorption images of thermal atoms where the Raman was turned on in 1 ms and held on for up to $50 \mu\text{s}$ ⁴.

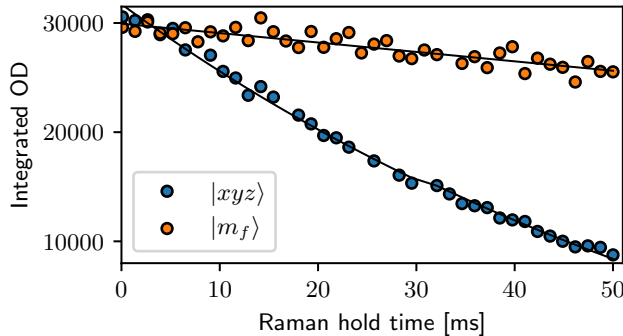


Figure 7: Lifetime of Raman dressed states. We Raman dressed atoms in the $|m_f\rangle$ and $|xyz\rangle$ states. The orange markers correspond to atoms initially prepared in $|m_f = -1\rangle$ (no high power RF involved) and the blue markers correspond to atoms $|xyz\rangle$ (three averaged traces). The lifetime of doubly dressed states is significantly reduced as compared to the lifetime of the Raman dressed $|m_f\rangle$ states, indicating that resonant scattering of photons is not our only loss mechanism.

8.3.2 Measuring quasimomentum distributions

Each pair of Raman lasers coupled states $|i, \mathbf{k}\rangle \rightarrow |j, \mathbf{k} + \mathbf{k}_{i,j}\rangle$ where $|i\rangle$ and $|j\rangle$ denote the initial and final $|xyz\rangle$ states, \mathbf{k} is the initial momentum and $\mathbf{k}_{i,j} = \mathbf{k}_i - \mathbf{k}_j$ is the two-photon Raman recoil momentum. Dressed states with quasimomentum \mathbf{q}

⁴How long we could hold on the Raman was limited by the RF antenna heating up.

are comprised of three bare states $|j, \mathbf{k}\rangle$ with momentum $\mathbf{k} = \mathbf{q} - \mathbf{k}_j$. The eigenstates of our Rashba SOC Hamiltonian take the form

$$|\Psi_n(\mathbf{q})\rangle = \sum_{j \in xyz} \sqrt{a_{n,j}(\mathbf{q})} e^{i\phi_{n,j}(\mathbf{q})} |j, \mathbf{k} = \mathbf{q} - \mathbf{k}_j\rangle, \quad (8.9)$$

where the quasimomentum \mathbf{q} is a good quantum number and the amplitudes are parametrized by $a_{n,j}(\mathbf{q})$ and $\phi_{n,j}(\mathbf{q})$. We leveraged the wide momentum distribution of a non-condensed ensemble ($T \approx 180$ nK and $T/T_c \approx 1.1$) to sample a wide range of momentum states simultaneously. By starting separately in each of the $|xyz\rangle$ states we sampled the range of quasimomentum states shown in Figure 8b, where the momentum distributions of an initial state $|j, \mathbf{k}\rangle$ is shifted from $\mathbf{q} = 0$ by the corresponding Raman wave vector \mathbf{k}_j .

Our measurement protocol consisted of abruptly removing the confining potential and the Raman lasers, initiating a 21 ms TOF. During this TOF we adiabatically transformed each of the $|xyz\rangle$ states back to a corresponding $|m_F\rangle$ state following the procedure described in Section 6.4 and spatially separated them using a Stern-Gerlach gradient. Finally we used resonant absorption imaging to measure the resulting spin-momentum distributions.

The FWHM of the cloud after TOF is about $700 \mu\text{m}$ which is much larger than the size of the in-situ cloud $\sim 50 \mu\text{m}$ and therefore the spatial density distribution of the TOF images represents momentum distribution of the atoms. For the $7.4 \mu\text{m}$ pixel size of our camera and the 3.283 magnification of our imaging system, the momentum resolution of our images was 0.018 k_L and the momentum distribution

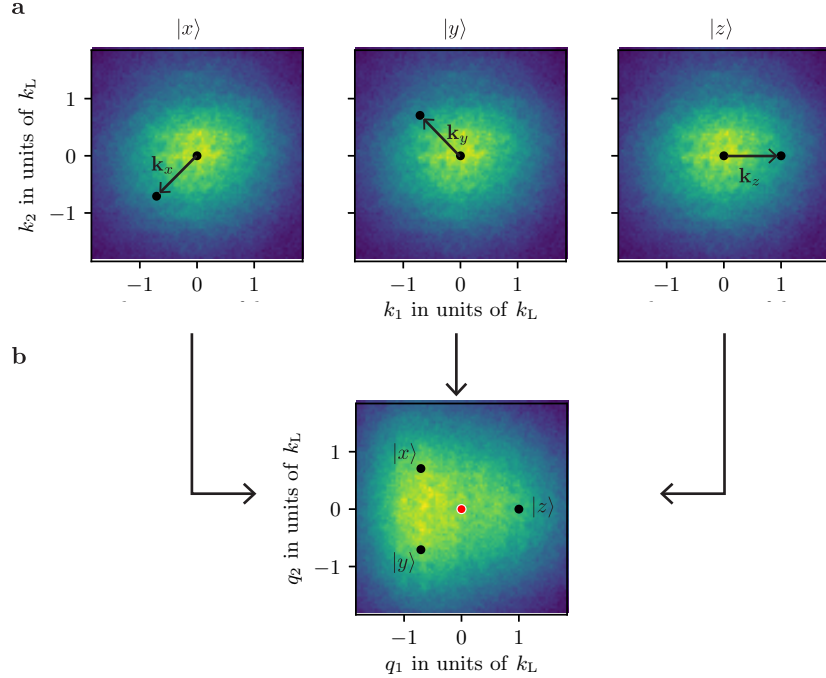


Figure 8: Mapping momentum into quasimomentum: **a** We used non-condensed atoms with a broad momentum distribution ($T \approx 180$ nK and $T/T_c \approx 1.1$). **b** Atoms in $|j, \mathbf{k}\rangle$ are mapped to Raman dressed states with quasimomentum $\mathbf{q} = \mathbf{k} + \mathbf{k}_j$. The black dots in the bottom panel represent the location of $\mathbf{k} = 0$ for each of the $|xyz\rangle$ states and the red dot corresponds to $\mathbf{q} = 0$. We performed our experiments starting separately in each of the $|xyz\rangle$ states, which allowed us to sample a larger range of quasimomentum states.

of a single state measured after TOF had a FWHM of $\sim 2.2 k_L$.

8.3.2.1 Correcting shears from Stern-Gerlach gradient

The magnetic field gradient used to separate the different m_f states in TOF additionally creates a trap for atoms in the direction perpendicular to the Stern-Gerlach separation, causing a compression (expansion) of the $m_f = -1$ (+1) states (see Section 3.2.1). The faster moving atoms are subject to a stronger potential and therefore the projections of a given momentum state \mathbf{k} along the Stern-Gerlach axis

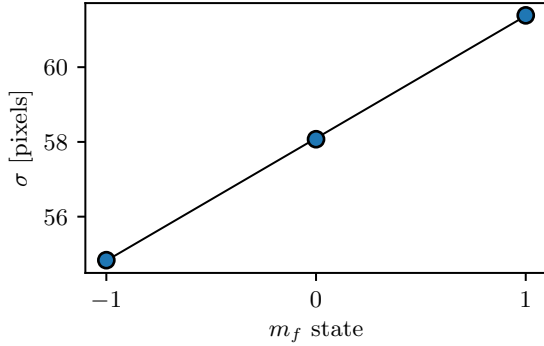


Figure 9: We measured the standard deviation of the momentum distribution along the axis perpendicular to the SG for 10 shots on each m_f state. From the slope of the linear fit we obtain a shearing parameter $\alpha \approx \pm 0.067$ for $m_f = \pm 1$.

and perpendicular to it were transformed as $k_{\parallel} \rightarrow k_{\parallel}$ and $k_{\perp} \rightarrow (1 + \alpha)k_{\perp}$, where $\alpha = 0$ for $m_f = 0$ and $\text{sign}(\alpha) = \pm 1$ for $m_f = \pm 1$.

Since we were interested in mapping the momentum distribution of atoms it was important for us to quantify and correct the effect of these shears in the TOF images. We used two different methods: First we prepared thermal atoms in all three of the m_f states and fit 2D Gaussians rotated by the angle of the SG displacement; 63.8 degrees for our images. Figure 9 shows the standard deviation extracted from the Gaussian fits along the axis perpendicular to the SG deviation as a function of m_f state. We performed a linear fit of σ and found that the $m_f = \pm$ states are expanded/contracted by about $\pm 6.7\%$ size of the compared to the $m_f = 0$ cloud ($\alpha = \pm 0.067$).

Alternatively we performed the Ramsey interferometer described in Section 8.5 but coupling only 2 states, either $|z\rangle \leftrightarrow |x\rangle$ or $|x\rangle \leftrightarrow |y\rangle$ (mapped to $| -1 \rangle \leftrightarrow | 0 \rangle$ and $| 0 \rangle \leftrightarrow | +1 \rangle$ after TOF). We looked at the oscillation frequencies of the density

for each pixel of the CCD camera (each sheared momentum state) and fit them to Equation 8.17 for fixed value of the recoil momentum $\mathbf{k}_{i,j}$ and with a free shear parameter that modifies \mathbf{q} . Using this method we extracted a shearing of the order of 7%, in good agreement with the Gaussian fitting method.

The transformed momentum coordinates were described by a function

$$g(\mathbf{k}) = (k_{\parallel}, (1 + \alpha)k_{\perp}) \quad (8.10)$$

and our observed data $(y_i^{(\text{shear})}, \mathbf{k}^{(\text{shear})})$ was the density in the sheared coordinate system at the i th pixel of the CCD sensor. The density in the unsheared coordinate was estimated using

$$y_j = \frac{\sum_i \exp[-(g(\mathbf{k}_j) - \mathbf{k}_i^{(\text{shear})})^2/2\sigma^2] y_i^{(\text{shear})}}{\sum_i \exp[-(g(\mathbf{k}_j) - \mathbf{k}_i^{(\text{shear})})^2/2\sigma^2]}, \quad (8.11)$$

where σ is the spacing between two consecutive pixels ($\sim 0.018 k_L$). Prior to any data analysis we applied this transformation to all of our images, where we used different values of α that define $g(\mathbf{k})$ for each of the m_f states.

8.4 Fourier spectroscopy of the Rashba dispersion

We directly measured the 2D dispersion relation using Fourier transform spectroscopy [51]. We considered the evolution of an initial state $|i, \mathbf{k}\rangle$ suddenly subjected to the Raman coupling lasers. This atomic Rabi-type interferometer is analogous to the three-port beam-splitter depicted in Figure 10a. During a pulse time t_p

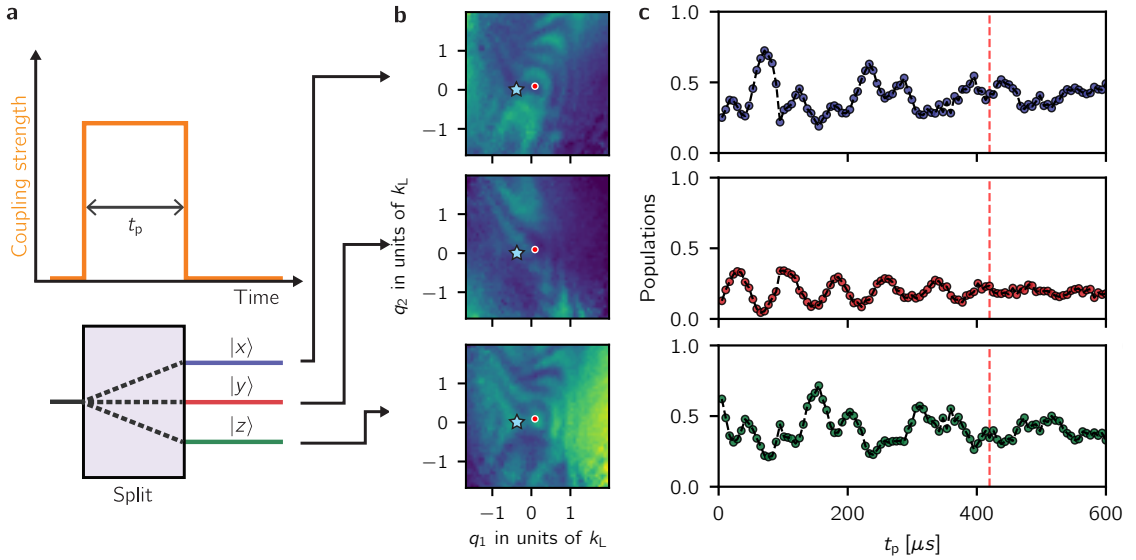


Figure 10: **a** Fourier spectroscopy protocol. We applied the Raman lasers for a variable time t_p : a Rabi-type atomic interferometer analogous to a three-port beam splitter. **b** Probabilities as a function of quasimomentum for a fixed Raman pulse time $t_p = 420 \mu\text{s}$ **c** Dynamics of the final populations of the $|xyz\rangle$ states with quasimomentum $(q_1, q_2) = (-0.55, -0.18) k_L$ (blue star in panels **b**) after initializing the system in the $|z\rangle$ state.

we followed the dynamics of the populations in the $|xyz\rangle$ states which evolved with oscillatory components proportional to $\sum_{j \neq n} a_{n,j}(\mathbf{q}) \cos([E_n(\mathbf{q}) - E_j(\mathbf{q})]t_p / \hbar)$, with frequencies determined by the eigenenergy differences $E_n - E_j$. Figure 10b shows the momentum dependent populations for a fixed pulse time t_p and Figure 10c shows representative final populations as a function of t_p for a fixed quasimomentum state. We Fourier transformed the populations with respect to t_p and for a given quasimomentum state for a total of 9 state, all of them with the same \mathbf{q} accounting for each of the three initial $|xyz\rangle$ states that was then split into 3 states. Figure 11 shows the PSD computed for each of the 9 states for planes of constant q_1 . The amplitude of the oscillatory components depends on the overlap integral between the initial

state and the Raman dressed states (see Equation 5.1) so sampling all these states gave us access to a wider range of measurable frequencies. The spectral maps in Figure 12b were produced by averaging the PSDs from the 9 different states using \bar{n} , the mean population in t_p , as a weight:

$$\text{PSD}^{(\text{mean})}(\mathbf{q}) = \frac{\sum_{i,j} \text{PSD}_{i,j}(\mathbf{q}) \bar{n}_{i,j}(\mathbf{q})}{\sum_{i,j} \bar{n}_i j(\mathbf{q})}, \quad (8.12)$$

where the indices i, j represent the different states of the grid shown in Figure 11. The extrema in the spectral maps are the energy differences $E_n - E_j$ in the engineered dispersion (Figure 10a). Figure 12 was obtained by combining all the spectral maps, and together they show the presence of a single Dirac point in the Rashba subspace, evidenced by the gap closing near $\mathbf{q} = 0$ and the photon-like lower branch. The dashed curves correspond to the energy differences computed for our system using the dispersions shown in Figure 12a, and are in clear agreement with our experiment. This measurement directly confirms the expected set of energies, including the existence of a two-state subspace approximately described by the Rashba Hamiltonian.

8.5 Quantum state tomography with Ramsey interferometer

The Fourier spectroscopy measurement confirmed our quantum engineering of the Rashba Hamiltonian. However, the energies shed no light on the topology of the different branches of the dispersion, which instead requires knowledge of the eigenstates. The Berry curvature present in the definition of the Chern number (Equa-

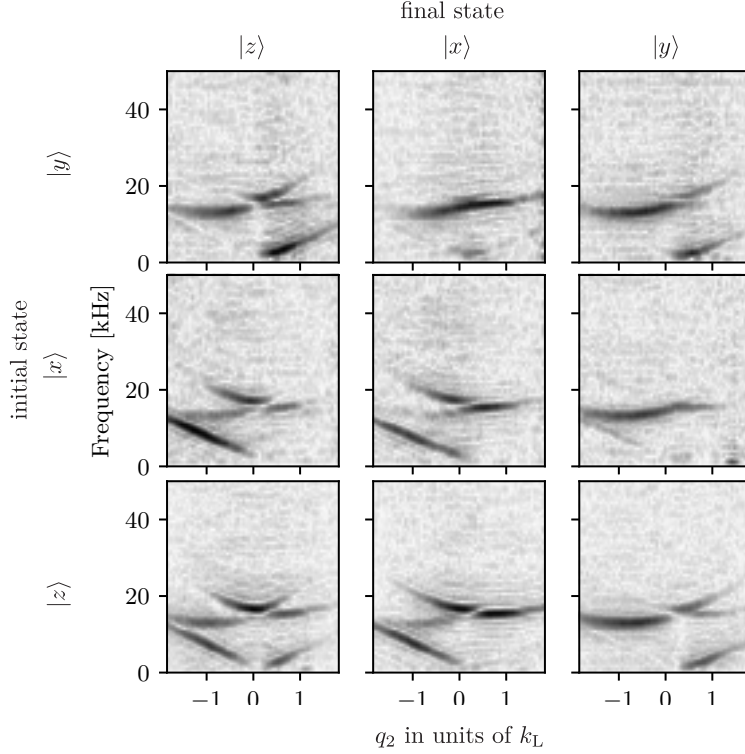


Figure 11: PSD of all the analyzed states as a function of q_2 for fixed $q_1 = 0.18 k_L$. The different overlaps between the initial state, the Raman dressed states and the measured final state result in peaks with different amplitudes.

tion 7.11) can be derived from the Berry's connection $\mathbf{A}_n(\mathbf{q}) = i \langle \Psi_n(\mathbf{q}) | \nabla_q | \Psi_n(\mathbf{q}) \rangle$,

which as discussed in Chapter 7 behaves much like a vector potential in classical electromagnetism. The Berry curvature $\boldsymbol{\Omega}_n(\mathbf{q}) = \nabla_q \times \mathbf{A}(\mathbf{q})$ is the associated magnetic field and the flux through any surface is the line integral of $\mathbf{A}(\mathbf{q})$ along its boundary, after neglecting the contributions of Dirac strings which I will discuss later. Using the expression for the Raman dressed eigenstates from Equation 8.9 we obtain

$$\mathbf{A}_n(\mathbf{q}) = - \sum_{j \in \{x,y,z\}} a_{n,j}(\mathbf{q}) \nabla_q \phi_{n,j}(\mathbf{q}), \quad (8.13)$$

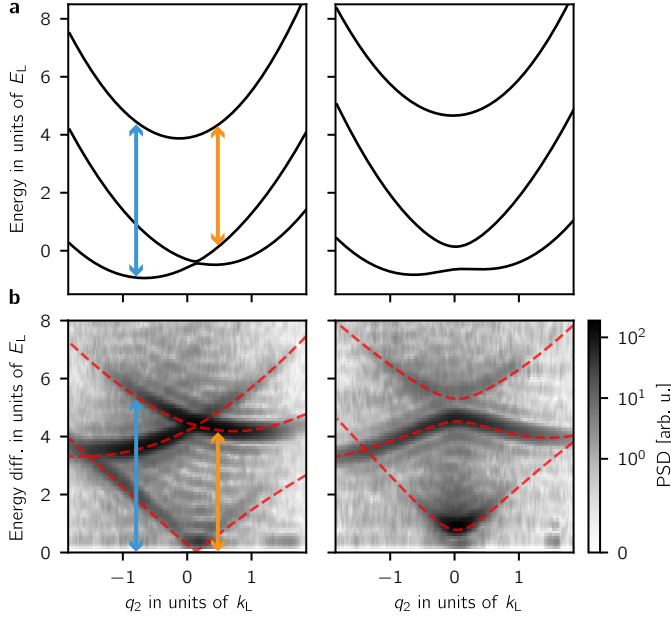


Figure 12: **a** Predicted dispersion relation as a function of q_2 for fixed $q_1 = -0.09 k_L$ (left) and $0.65 k_L$ (right), computed for the experiment parameters. The energy differences between the branches enclosing the vertical arrows appear as peaks in the spectral maps below. **b** Power spectral density (PSD) for the same parameters as above which we obtained by Fourier transforming the populations in the $|xyz\rangle$ states with respect to t_p . The dashed lines correspond to the energy differences computed using the dispersion curves on the top panel.

which depends on both the phase and amplitude of the wave function. We obtained $a_{n,j}(\mathbf{q})$ and $\phi_{n,j}(\mathbf{q})$ using a three-arm time-domain Ramsey interferometer (see Section 3.4.2), implementing a variant of quantum state tomography [125, 126]. The use of a multi-path interferometer allowed us to transduce information about phases into state populations, which we readily obtained from absorption images.

Figure 13 shows our experimental protocol which I will describe in more detail in the following section. We adiabatically mapped an initial $|j, \mathbf{k}\rangle$ state into a corresponding eigenstate $|n, \mathbf{q} = \mathbf{k} + \mathbf{k}_j\rangle$, either in the topologically trivial highest dispersion branch ($n = 3$) or in the topological ground branch ($n = 1$) by dy-

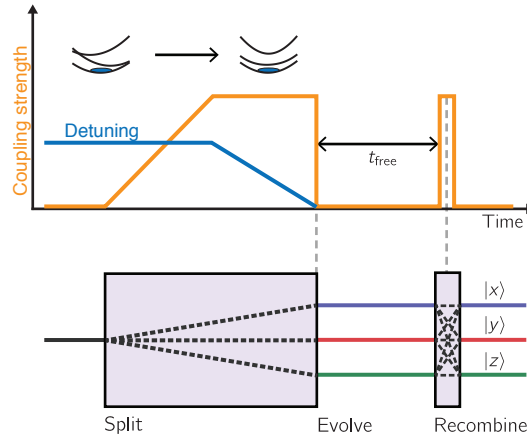


Figure 13: Experimental protocol for three-arm Ramsey interferometer (not to scale). (Top) We started with atoms in state $|z, y, \mathbf{q}_i = \mathbf{k} + \mathbf{k}_j\rangle$ and with detuning $\delta_y = \pm 5 E_L$ and $\delta_z = \pm 5 E_L$. We ramped the Raman lasers on in $750 \mu\text{s}$ and then ramped the detuning to nominally zero. We let the system evolve in the dark for times between $5 \mu\text{s}$ and $400 \mu\text{s}$, followed by a $25 \mu\text{s}$ Raman pulse. (Bottom) The implemented experimental protocol was equivalent to a three-arm interferometer that split an initial state into three final states with amplitudes related to the initial wave function phases.

namically tailoring both the Raman coupling strength and detuning. We suddenly turned off the Raman coupling, thereby allowing the three bare state components of the Rashba eigenstates to undergo free evolution for a time t_{free} , constituting the three arms of our time-domain interferometer. Finally we applied a three-port beam splitter using a brief Raman ‘recombination’ pulse to interfere the three arms.

8.5.1 Wave function evolution in Ramsey interferometer

Rashba dressed state preparation: We started with $|xyz\rangle$ states at different RF coupling strength $\Omega_0 = \Omega_{\text{RF}}/\pi 2 \pm 20 \text{ kHz}$, such that the energies of the $|z\rangle$ and $|y\rangle$ states were shifted by about $\pm 18.8 \text{ kHz}$. We used the same Raman frequencies as described earlier and therefore the change in the $|xyz\rangle$ state eigenenergies

corresponded to non-zero δ_z and δ_y in Equation 8.8. We chose the detuning such that the initial state had a large overlap with either the $n = 1$ or the $n = 3$ eigenstates of Equation 8.8. We then ramped on the Raman coupling in $750\ \mu\text{s}$, adiabatically mapping the $|z\rangle$ and $|y\rangle$ states into the $n = 1$ or $n = 3$ eigenstates. Because our only experimental knob for dynamically changing the detuning was Ω_{RF} we could not control δ_x so when we initialized the system in $|x\rangle$ the the final dressed state always corresponded to the $n = 2$ branch. After turning on the Raman we ramped Ω_{RF} to its final value in $1\ \text{ms}$, effectively ramping δ_z and δ_y close to zero. This detuning ramp had the additional effect of moving the location Dirac point through the atoms when loaded in the $n = 1$ branch, thereby creating a trajectory where the state preparation was not adiabatic. This trajectory depended on the sign of the detuning ramp so we combined data from different initial states in order to exclude the Dirac point trajectories. Near the final location of the Dirac point the state preparation can not be adiabatic regardless of the initial state or detuning used for the ground state preparation. Figure 14a shows an example an absorption image of atoms initially prepared in the $|y\rangle$ state and with δ_y such atoms are loaded in the $n = 1$ branch. The Dirac point is initially located near the lower left edge of the cloud and when δ_i was ramped the location of the Dirac point was dragged across the whole cloud leaving lines where non-adiabatic transitions occurred as can be seen in Figure 14b. The location of the Dirac point as a function of δ_i can also be directly computed by numerically diagonalizing the SOC Hamiltonian from Equation 8.8. At the end of this stage, excluding the points of non-adiabatic transitions, the state of the system was described by the eigenstates in Equation 8.9.

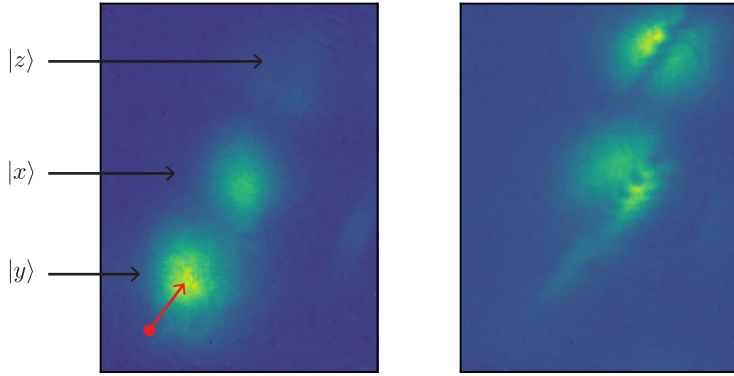


Figure 14: **a** We prepared atoms in the $|y\rangle$ state such that they are adiabatically mapped to the ground dispersion branch. **b** We ramped δ_i and dragged the Dirac point through the atoms.

Free evolution: We suddenly turned off the Raman coupling, thereby projecting the Raman dressed states back into the $|xyz\rangle$ basis. Each of the $|xyz\rangle$ state represents a different branch of the interferometer and they acquire phases that are proportional to t_{free}

$$|\Psi_n(\mathbf{q})\rangle \rightarrow \sum_{j \in xyz} \sqrt{a_{n,j}(\mathbf{q})} e^{i\phi_{n,j}(\mathbf{q})} e^{-iE_j(\mathbf{q})t_{\text{free}}/\hbar} |j, \mathbf{k} = \mathbf{q} - \mathbf{k}_j\rangle, \quad (8.14)$$

where $E_j(\mathbf{q}) = \hbar^2 \mathbf{q}^2 / 2m$ is the free particle energy. The Rashba wavefunction phases $\phi_{n,j}(\mathbf{q})$ that we were interested in measuring were imprinted during the loading procedure. The dynamical phases $E_j(\mathbf{q})t_{\text{free}}/\hbar$ acquired in the different interferometer arms does not contribute to our knowledge of the Rashba eigenstates as they describe the evolution of the system in the absence of Raman dressing.

Recombination pulse: We applied a 25 μs Raman pulse that acted as a second beam splitter in our interferometer sequence. The wave function after the

pulse is

$$|\Psi(\mathbf{q})\rangle = \sum_{j,j' \in xyz} \sqrt{a_{n,j}(\mathbf{q})} e^{i(\phi_{n,j}(\mathbf{q}) - E_j(\mathbf{q})t_{\text{free}}/\hbar)} U_{j,j'}(\mathbf{q}) |j, \mathbf{k} = \mathbf{q} - \mathbf{k}_j\rangle, \quad (8.15)$$

where $U_{j,j'}(\mathbf{q}) = |U_{j,j'}(\mathbf{q})| \exp(i\phi_{j,j'}^{\text{(pulse)}}(\mathbf{q}))$ is the matrix element of the unitary transformation $\exp(i\hat{H}_{\text{R}}(\mathbf{q})t_{\text{pulse}})$ associated to the Raman pulse. At the end of this procedure, the population in a final state $|l, \mathbf{q}\rangle$ is

$$P_l(\mathbf{q}, t) = \sum_{i \neq j} |U_{l,i}| |U_{j,l}| \sqrt{a_{n,i} a_{n,j}} \cos(\omega_{i,j}(\mathbf{q})t + \phi_{n,i}(\mathbf{q}) - \phi_{n,j}(\mathbf{q}) + \phi_{l,i,j}^{\text{(pulse)}}(\mathbf{q})), \quad (8.16)$$

which directly reads out the phase differences, independent of the output port l .

Here $\phi_{l,i,j}^{\text{(pulse)}}(\mathbf{q})$ is a smoothly varying phase imprinted by the recombination pulse and is independent of \mathbf{q} in the limit of short, strong pulses and does not affect the topological index of the system. The angular frequencies

$$\omega_{i,j}(\mathbf{q}) = \hbar \mathbf{q} \cdot \mathbf{k}_{i,j} / m + \delta_{i,j} \quad (8.17)$$

result from the known free particle kinetic energy, the recoil momenta and detuning $\delta_{i,j}$ from the tripod resonance condition. Figure 13b shows the momentum-dependent populations in each output port at fixed $t_{\text{free}} = 160 \mu\text{s}$ and Figure 13c shows the populations as a function of t_{free} for a representative quasimomentum state $(q_1, q_2) = (0.55, -0.92) k_{\text{L}}$.

We obtained the relative phases $\Delta\phi_{n,i,j,l}(\mathbf{q}) = \phi_{n,i}(\mathbf{q}) - \phi_{n,j}(\mathbf{q}) + \phi_{l,i,j}^{\text{(pulse)}}(\mathbf{q})$ from Equation 8.16 by fitting the measured populations to the sum of three cosines

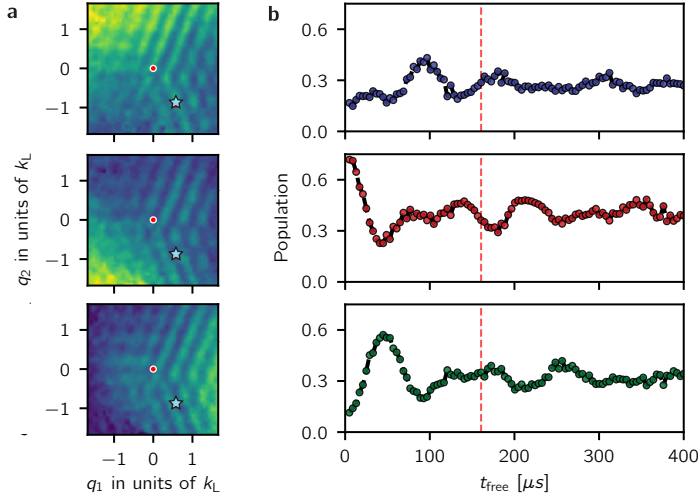


Figure 15: **a** Probabilities as a function of quasimomentum for the three output ports of the interferometer at $t_{\text{free}} = 160 \mu\text{s}$ **b** Probabilities as a function of free evolution time t_{free} for an input state with quasimomentum $(q_1, q_2) = (0.55, -0.92) k_L$ indicated by the blue star on **a** and in the topological ground branch ($n = 1$)

with the known free particle frequencies but unknown amplitudes and phases.

8.5.2 Combining phases from different measurements

We combined the phases $\Delta\phi_{n,i,j,l}(\mathbf{q})$ obtained from fits to six different states (two initial states split into 3 states). Similar to the Fourier spectroscopy measurements, we performed a weighted average of the fitted relative phases

$$\Delta\phi_{n,i,j}(\mathbf{q}) = \frac{\sum_l \Delta\phi_{n,i,j,l}(\mathbf{q}) w_{i,j,l}(\mathbf{q})}{\sum_l w_{i,j,l}(\mathbf{q})}, \quad (8.18)$$

where the weights are determined using fit uncertainties and when loading atoms in the topological branch we additionally accounted for the trajectory of the Dirac point during the loading procedure. Figure 16 shows an example of two different weight arrays used to combine the phase difference associated to the $z \rightarrow x$ transition

$i, j = z, x$ for the topological branch $n = 1$ ($\Delta_{1,z,x}$):

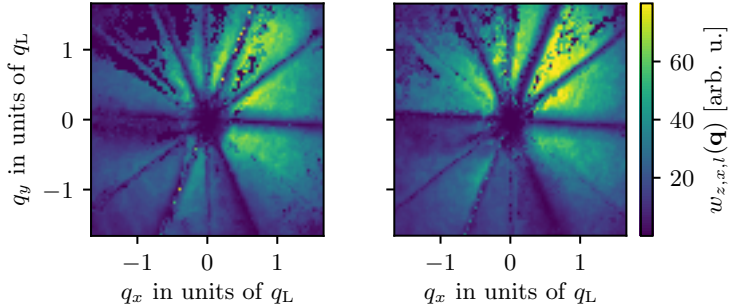


Figure 16: Two sample weight arrays $w_{i,j,l}(\mathbf{q})$ for $i, j = z, x$ and atoms prepared in the topological disperion branch. We obtained the weights using the uncertainties from the fits and the trajectory of the Dirac point during the state preparation. We combined the weights and the phase differences $\Delta\phi_{n,i,j,l}$ obtained from the time dependent fits using Equation 8.18 to obtain the phase maps displayed in Figure 17a

The ‘spokes’ in the weight arrays correspond to high uncertainty regions. This uncertainty comes of our inability to resolve the phases of low frequencies $\omega_{ij}(\mathbf{q})$ as well as when two different frequencies $\omega_{ij}(\mathbf{q})$ and $\omega_{i'j'}(\mathbf{q})$ are close to each other which is limited by the largest value of t_{free} in the experiment. I fit and combined a total of 120,000 different time traces (60,000 for each dispersion branch) to produce phase maps like those shown in Figure 17a.

8.5.3 Measuring the topological index

Figure 17a shows typical phase-maps for both the non-topological and topological branches. In the non-topological phase-maps the momentum dependence of the recombination pulse $\phi_{l,i,j}^p(\mathbf{q})$ causes a smooth variation of the phases along the Raman recoil axes that does not affect the evaluation topological index of our system. We recovered the phases $\phi_{n,j}$ of the full spinor wave function from the relative

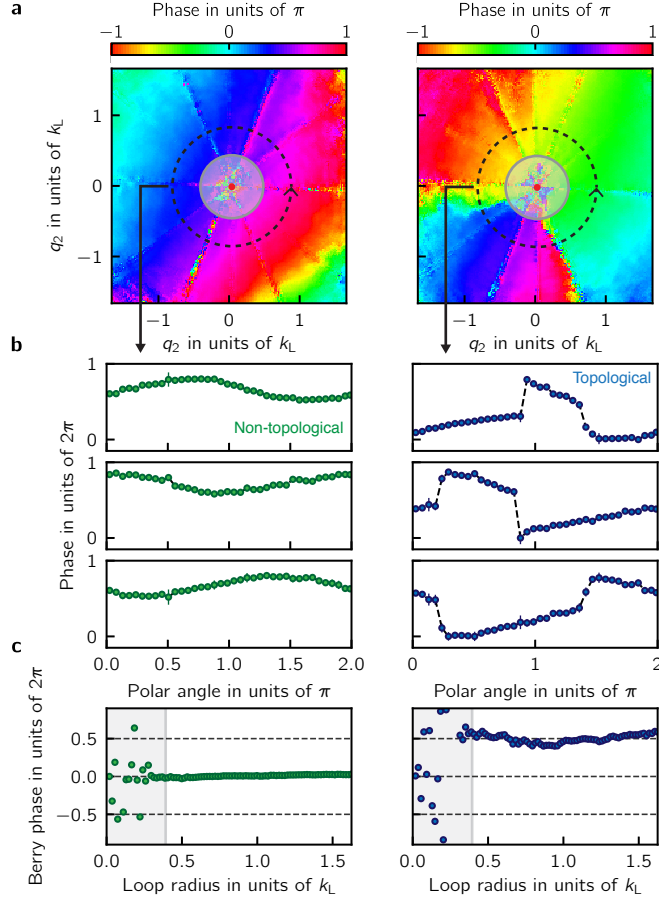


Figure 17: Topological invariants from quantum state tomography, for the non-topological branch ($n = 3$, left) and the topological branch ($n = 1$, right). **a** Phase differences as a function of quasimomentum from the the $z \rightarrow x$ transition **b** Phase differences as a function of polar angle for a loop radius $0.77 k_L$ from the $z \rightarrow x$ (top), $x \rightarrow y$ (middle) and $y \rightarrow z$ (bottom) transitions. The phases associated to the topological branch are characterized by two π valued discontinuities. Each row of phases was shifted by a constant value so that the three rows of phases share the same vertical axis. All phases shown here were binned and averaged using the fit uncertainties as weights. **c** Inferred Chern number as a function of loop radius. For loops with $q > 0.4 k_L$ we obtained an integrated Berry phase and asymptotic Chern number of $\Phi_B/2\pi = 0.01(1)$ for the non-topological branch and $\Phi_B/2\pi = 0.5(5)$ for the topological branch.

phases $\Delta\phi_{n,i,j}(\mathbf{q})$ by choosing a particular gauge such that $\phi_{n,3} = 0$. We then used the values of $a_{n,i}$ obtained from measuring the populations in the $|xyz\rangle$ states at $t_{\text{free}} = 0$ in combination with the phases of the wave function to compute the Berry

connection [127]. Figure 17b shows the three phase differences as a function of polar angle for a loop of radius $q \approx 0.77 k_L$. In addition to the smooth variations induced by the recombination which are present in both columns, the phases of the topological branch have two π valued jumps that lead to non-zero Berry phases when the Berry connection is integrated along a closed loop in momentum space. Figure 17c shows the integrated Berry phase as a function of loop radius. As mentioned earlier the largest value of t_{free} limits how well we can resolve the phases of small frequencies and this is reflected in the large variation in the Berry phase depicted in the shaded region of Figure 17c near $q = 0$. For loops with $q > 0.4 k_L$ we obtain an integrated Berry phase that suggests an asymptotic Chern number of $\Phi_B/2\pi = 0.01(1)$ for the non-topological branch and $\Phi_B/2\pi = 0.5(5)$ for the topological branch. However, Berry's phase measurements including ours includes the (potential) contribution of any Dirac strings traversing the integration area. In our system, these are possible at the Dirac point *, and each contributes $\pm 2\pi$ to Φ_B as was discussed in Section 7.6. Even with this 2π ambiguity we are able to associate a half-integer Chern number with the topological branch, which is possible only for a topological dispersion branch in the continuum.

8.6 Conclusion

In conventional lattices — for example graphene, or the topological Haldane model — it is well established that Dirac points each contribute a Berry's phase of $\Phi_B/2\pi = \pm 1/2$ [128], but crystalline materials conspire for these to appear in

pairs [129], always delivering integer Chern numbers. In contrast, our continuum system contains a single Dirac point, resulting in a non-integer Chern number. This leads to intriguing questions about edge states at interfaces with non-integer Chern numbers with non-integer Chern number differences. Initial studies in the context of electromagnetic waveguides [130] and atmospheric waves [88] have applied Chern invariants and the bulk-edge correspondence to continuous media.

While the true Rashba Hamiltonian features a ring of degenerate eigenstates, our implementation including the quadratic and cubic Dresselhaus-like SOC lifts this macroscopic degeneracy giving three nearly degenerate minima [118]. Already these three minima could allow the study of rich ground state physics in many body systems of bosons, for example the formation of fragmented BECs [115] when the system does not condense into a single-particle state. Furthermore, the use of additional spin states or larger Raman couplings can partially restore this degeneracy allowing the possible realization of fractional Hall like states [131].

Chapter 9: Conclusions and outlook

The end!

Chapter 9: Realization of a fractional period adiabatic superlattice

This was an intermediate step to engineer topological matter with a lattice.

Appendix A: RbLi: the good, the bad and the ugly

Appendix B: New apparatus

B.1 Water cooling stuff

B.2 Electrical installation

B.3 New Rb ‘oven’

Appendix C: Full derivation of the Raman coupled $|xyz\rangle$ states

In this Appendix I derive the full time-dependent Hamiltonian describing the Raman coupled $|xyz\rangle$ states. The system is based on the theoretical proposal in [57] to engineer an effective Rashba-type Hamiltonian using three Raman laser beams.

We consider an $F = 1$ system that is subject to a constant magnetic field $B_0 \mathbf{e}_z$ and an RF magnetic field $B_{RF} \cos(\omega_{RF}t) \mathbf{e}_x$. The system is described by the Hamiltonian

$$\hat{H}_{RF} = \omega_0 \hat{F}_z - \frac{\epsilon}{\hbar} (\hat{F}_z^2 - \mathbb{I}) + 2\Omega_{RF} \cos(\omega_{RF}t) \hat{F}_x, \quad (\text{C.1})$$

where $\omega_0 = g_F \mu_B B_0$ is the Larmor frequency, ϵ is a quadratic Zeeman shift that breaks the degeneracy of the $|m_F = -1\rangle \leftrightarrow |m_F = 0\rangle$ and $|m_F = 1\rangle \leftrightarrow |m_F = 0\rangle$ transitions, and $\Omega_{RF} = g_F \mu_B B_{RF}/2$ is the RF coupling strength. We then transform the Hamiltonian into a rotating frame using the unitary transformation $\hat{U}(t) =$

$\exp(-i\omega_{RF}t\hat{F}_z)$. The spin-1 operators under this transformation are transformed as

$$\begin{aligned}
 \hat{F}_x &\rightarrow \cos(\omega_{RF}t)\hat{F}_x - \sin(\omega_{RF}t)\hat{F}_y \\
 &= e^{i\omega_{RF}t}\hat{F}_+ + e^{-i\omega_{RF}t}\hat{F}_- \\
 \hat{F}_y &\rightarrow \sin(\omega_{RF}t)\hat{F}_x + \cos(\omega_{RF}t)\hat{F}_y \\
 &= \frac{1}{i}(e^{i\omega_{RF}t}\hat{F}_+ - e^{-i\omega_{RF}t}\hat{F}_-) \\
 \hat{F}_z &\rightarrow \hat{F}_z.
 \end{aligned} \tag{C.2}$$

The unitary evolution in the rotating frame is described by the transformed Hamiltonian $\hat{U}^\dagger(t)(\hat{H}_{RF} - i\hbar\partial_t)\hat{U}(t)$, which after neglecting terms that are oscillating at $2\omega_{RF}$ is

$$\hat{H}_{RWA} = \Delta\hat{F}_z - \frac{\epsilon}{\hbar}(\hat{F}_z^2 - \mathbb{I}) + \Omega_{RF}\hat{F}_x \tag{C.3}$$

The eigenstate of Equation C.3 are the $|xyz\rangle$ states described in Chapter 6. I will show later that all states can be coupled using a combination of the \hat{F}_x , \hat{F}_y , and \hat{F}_z operators in the lab frame, i.e. using different combinations of Raman laser beams with appropriately chosen polarizations.

For simplicity I will start this description in the lab frame and I will not make any initial assumptions about direction of propagation or frequency each of the beams. Consider three linearly polarized Raman beams propagating along the xy plane as shown in Fig. 1. The electric field at the atoms is

$$\mathbf{E}(x, t) = \sum_{i=1}^3 E_i \mathbf{e}_i e^{i(\mathbf{k}_i \cdot \mathbf{x} - \omega_i t)}, \quad (\text{C.4})$$

where E_i is the field amplitude, ω_i is the angular frequency, and \mathbf{e}_i is the polarization of each of the beams. In order to generate the necessary Raman couplings proportional to \hat{F}_x , \hat{F}_y and \hat{F}_z we need two horizontally polarized Raman beams and one vertically polarized beam. Without loss of generality we choose

$$\begin{aligned} \mathbf{e}_1 &= \frac{(k_{1y}, -k_{1x}, 0)}{\|\mathbf{k}_1\|^2}, \\ \mathbf{e}_2 &= (0, 0, 1), \\ \mathbf{e}_3 &= \frac{(k_{3y}, -k_{3x}, 0)}{\|\mathbf{k}_3\|^2}, \end{aligned} \quad (\text{C.5})$$

The Raman Hamiltonian is given by the vector component of the Stark shift generated by the atom-light interaction

$$\hat{H}_R = (i u_v \mathbf{E} \times \mathbf{E}^*) \cdot \hat{F}, \quad (\text{C.6})$$

where u_v is the vector polarizability. Now let's expand Eq. C.6 using the field at the atoms from Eq. C.4.

$$\begin{aligned}
\mathbf{E} \times \mathbf{E}^* &= (E_1^* \mathbf{e}_1 e^{-i(\mathbf{k}_1 \cdot \mathbf{x} - \omega_1 t)} + E_2^* \mathbf{e}_2 e^{-i(\mathbf{k}_2 \cdot \mathbf{x} - \omega_2 t)} + E_3^* \mathbf{e}_3 e^{-i(\mathbf{k}_3 \cdot \mathbf{x} - \omega_3 t)}) \times c.c \\
&= E_1^* E_2 (\mathbf{e}_1 \times \mathbf{e}_2) e^{i[(\mathbf{k}_2 - \mathbf{k}_1) \cdot \mathbf{x} - (\omega_2 - \omega_1)t]} + E_1^* E_3 (\mathbf{e}_1 \times \mathbf{e}_3) e^{i[(\mathbf{k}_3 - \mathbf{k}_1) \cdot \mathbf{x} - (\omega_3 - \omega_1)t]} \\
&\quad + E_2^* E_1 (\mathbf{e}_2 \times \mathbf{e}_1) e^{i[(\mathbf{k}_1 - \mathbf{k}_2) \cdot \mathbf{x} - (\omega_1 - \omega_2)t]} + E_2^* E_3 (\mathbf{e}_2 \times \mathbf{e}_3) e^{i[(\mathbf{k}_3 - \mathbf{k}_2) \cdot \mathbf{x} - (\omega_3 - \omega_2)t]} \\
&\quad + E_3^* E_1 (\mathbf{e}_3 \times \mathbf{e}_1) e^{i[(\mathbf{k}_1 - \mathbf{k}_3) \cdot \mathbf{x} - (\omega_1 - \omega_3)t]} + E_3^* E_2 (\mathbf{e}_3 \times \mathbf{e}_2) e^{i[(\mathbf{k}_2 - \mathbf{k}_3) \cdot \mathbf{x} - (\omega_2 - \omega_3)t]} \\
&= 2i \left[(\mathbf{e}_1 \times \mathbf{e}_2) \text{Im}\{E_1^* E_2 e^{i(\mathbf{k}_{21} \cdot \mathbf{x} - \omega_{21} t)}\} \right. \\
&\quad \left. + (\mathbf{e}_1 \times \mathbf{e}_3) \text{Im}\{E_1^* E_3 e^{i(\mathbf{k}_{32} \cdot \mathbf{x} - \omega_{32} t)}\} \right. \\
&\quad \left. + (\mathbf{e}_2 \times \mathbf{e}_3) \text{Im}\{E_2^* E_3 e^{i(\mathbf{k}_{32} \cdot \mathbf{x} - \omega_{32} t)}\} \right] \\
&\tag{C.7}
\end{aligned}$$

also from the definitions of the polarization vectors we can calculate the cross products

$$\begin{aligned}
\mathbf{e}_1 \times \mathbf{e}_2 &= \frac{(-k_{1x}, -k_{1y}, 0)}{\|\mathbf{k}_1\|^2} = -\hat{\mathbf{k}}_1 \\
\mathbf{e}_1 \times \mathbf{e}_3 &= \frac{(0, 0, -k_{1y}k_{3x} + k_{3y}k_{1x})}{\|\mathbf{k}_1\|^2 \|\mathbf{k}_3\|^2} = \mathbf{e}_z \sin \theta_{13} \\
\mathbf{e}_2 \times \mathbf{e}_3 &= \frac{(k_{3x}, k_{3y}, 0)}{\|\mathbf{k}_3\|^2} = \hat{\mathbf{k}}_3,
\end{aligned} \tag{C.8}$$

and putting everything together

$$\begin{aligned}
iu_v \mathbf{E}^* \times \mathbf{E} \cdot \hat{\mathbf{F}} &= -2u_v \left[-\hat{\mathbf{k}}_1 \text{Im}\{12\} + \mathbf{e}_z \sin \theta_{13} \text{Im}\{13\} + \hat{\mathbf{k}}_3 \text{Im}\{23\} \right] \cdot \hat{\mathbf{F}} \\
&= (\Omega_x, \Omega_y, \Omega_z) \cdot \hat{\mathbf{F}}
\end{aligned} \tag{C.9}$$

with

$$\begin{aligned}\Omega_x &= \frac{k_{1x}}{\|\mathbf{k}_1\|} \text{Im}\{\Omega_{12} e^{i(\mathbf{k}_{21} \cdot \mathbf{x} - \omega_{21} t)}\} + \frac{k_{3x}}{\|\mathbf{k}_3\|} \text{Im}\{\Omega_{23} e^{i(\mathbf{k}_{32} \cdot \mathbf{x} - \omega_{32} t)}\} \\ \Omega_y &= \frac{k_{1y}}{\|\mathbf{k}_1\|} \text{Im}\{\Omega_{12} e^{i(\mathbf{k}_{21} \cdot \mathbf{x} - \omega_{21} t)}\} + \frac{k_{3y}}{\|\mathbf{k}_3\|} \text{Im}\{\Omega_{23} e^{i(\mathbf{k}_{32} \cdot \mathbf{x} - \omega_{32} t)}\} \\ \Omega_z &= \text{Im}\{\Omega_{13} e^{i(\mathbf{k}_{31} \cdot \mathbf{x} - \omega_{31} t)}\},\end{aligned}\quad (\text{C.10})$$

and

$$\begin{aligned}\Omega_{12} &= 2u_v E_1^* E_2 \\ \Omega_{13} &= -2u_v E_1^* E_3 \sin \theta_{13} \\ \Omega_{23} &= -2u_v E_2^* E_3.\end{aligned}\quad (\text{C.11})$$

C.0.0.1 Going into rotating frame

This is where things start getting fun. We need to transform Eq. C.9 into the rotating frame. Which terms are ‘slow’ and we get to keep and which are ‘fast’ depends on the specific choice of Raman frequencies. Only the \hat{F}_x and \hat{F}_y operators are affected by the unitary transformation while \hat{F}_z remains unchanged. We therefore choose the beams that give a \hat{F}_z coupling to be close in frequency.

There are two different frequency choices which Dan calls ‘blue’ and ‘red’ detuned which are shown in Fig. 2, and they determine whether ω_{21} and ω_{31} are positive or negative. I’m not sure if we can generalize something at this point. Lets

look at the first term of the $\Omega_x \hat{F}_x$ coupling for practice.

$$\begin{aligned}
\Omega_x^{(1)} \hat{F}_x &\rightarrow \frac{1}{4i} \frac{k_{1x}}{\|\mathbf{k}_1\|} \left(\Omega_{12} e^{i(\mathbf{k}_{21} \cdot \mathbf{x} - \omega_{21})t} - \Omega_{12}^* e^{-i(\mathbf{k}_{21} \cdot \mathbf{x} - \omega_{21}t)} \right) \left(e^{i\omega_{RF}t} \hat{F}_+ + e^{-i\omega_{RF}t} \hat{F}_- \right) \\
&\approx \frac{1}{4i} \frac{k_{1x}}{\|\mathbf{k}_1\|} \left(\Omega_{12} e^{i(\mathbf{k}_{21} \cdot \mathbf{x} - (\omega_{21} \mp \omega_{RF})t)} \hat{F}_\pm - \Omega_{12}^* e^{-i(\mathbf{k}_{21} \cdot \mathbf{x} - (\omega_{21} \mp \omega_{RF})t)} \hat{F}_\mp \right) \\
&= \frac{1}{4i} \frac{k_{1x}}{\|\mathbf{k}_1\|} \left(\Omega_{12} e^{i(\mathbf{k}_{21} \cdot \mathbf{x} - (\omega_{21} \mp \omega_{RF})t)} - c.c. \right) \hat{F}_x \pm i \left(\Omega_{12} e^{i(\mathbf{k}_{21} \cdot \mathbf{x} - (\omega_{21} \mp \omega_{RF})t)} + c.c. \right) \hat{F}_y \\
&= \frac{1}{2} \frac{k_{1x}}{\|\mathbf{k}_1\|} |\Omega_{12}| \left(\sin[\mathbf{k}_{21} \cdot \mathbf{x} - (\omega_{21} \mp \omega_{RF})t + \phi_{12}] \hat{F}_x \pm \cos[\mathbf{k}_{21} \cdot \mathbf{x} - (\omega_{21} \mp \omega_{RF})t + \phi_{12}] \hat{F}_y \right)
\end{aligned} \tag{C.12}$$

Where the upper sign corresponds to the $\omega_{21} > 0$ case (blue detuned) and the lower sign to $\omega_{21} < 0$ (red detuned). Similarly, the second therm of $\Omega_x \hat{F}_x$ is

$$\begin{aligned}
\Omega_x^{(2)} \hat{F}_x &\rightarrow \frac{1}{4i} \frac{k_{3x}}{\|\mathbf{k}_3\|} \left(\Omega_{23} e^{i(\mathbf{k}_{32} \cdot \mathbf{x} - \omega_{32})t} - \Omega_{23}^* e^{-i(\mathbf{k}_{32} \cdot \mathbf{x} - \omega_{32}t)} \right) \left(e^{i\omega_{RF}t} \hat{F}_+ + e^{-i\omega_{RF}t} \hat{F}_- \right) \\
&\approx \frac{1}{2} \frac{k_{3x}}{\|\mathbf{k}_3\|} |\Omega_{23}| \left(\sin[\mathbf{k}_{32} \cdot \mathbf{x} - (\omega_{32} \mp \omega_{RF})t + \phi_{23}] \hat{F}_x \pm \cos[\mathbf{k}_{32} \cdot \mathbf{x} - (\omega_{32} \mp \omega_{RF})t + \phi_{23}] \hat{F}_y \right)
\end{aligned} \tag{C.13}$$

where I used the same sign convention as before. It is important to keep in mind though that if ω_{21} is positive then ω_{32} must be negative and vice versa. **Double**

check again that signs are correct! Let's continue with the algebra galore...

$$\begin{aligned}
\Omega_y^{(1)} \hat{F}_y &\rightarrow -\frac{1}{4} \frac{k_{1y}}{\|\mathbf{k}_1\|} \left(\Omega_{12} e^{i(\mathbf{k}_{21} \cdot \mathbf{x} - \omega_{21} t)} - \Omega_{12}^* e^{-i(\mathbf{k}_{21} \cdot \mathbf{x} - \omega_{21} t)} \right) \left(e^{i\omega_{RF} t} \hat{F}_+ - e^{-i\omega_{RF} t} \hat{F}_- \right) \\
&= \mp \frac{1}{4} \frac{k_{1y}}{\|\mathbf{k}_1\|} \left(\Omega_{12} e^{i(\mathbf{k}_{21} \cdot \mathbf{x} - (\omega_{21} \mp \omega_{RF}) t)} \hat{F}_\pm + \Omega_{12}^* e^{-i(\mathbf{k}_{21} \cdot \mathbf{x} - (\omega_{21} \mp \omega_{RF}) t)} \hat{F}_\mp \right) \\
&= \mp \frac{1}{4} \frac{k_{1y}}{\|\mathbf{k}_1\|} \left(\left(\Omega_{12} e^{i(\mathbf{k}_{21} \cdot \mathbf{x} - (\omega_{21} \mp \omega_{RF}) t)} + c.c. \right) \hat{F}_x + i \left(\Omega_{12} e^{i(\mathbf{k}_{21} \cdot \mathbf{x} - (\omega_{21} \mp \omega_{RF}) t)} - c.c. \right) \hat{F}_y \right) \\
&= \mp \frac{1}{2} \frac{k_{1y}}{\|\mathbf{k}_1\|} |\Omega_{12}| \left(\cos[\mathbf{k}_{21} \cdot \mathbf{x} - (\omega_{21} \mp \omega_{RF}) t + \phi_{12}] \hat{F}_x - \sin[\mathbf{k}_{21} \cdot \mathbf{x} - (\omega_{21} \mp \omega_{RF}) t + \phi_{12}] \hat{F}_y \right)
\end{aligned} \tag{C.14}$$

and

$$\begin{aligned}
\Omega_y^{(2)} \hat{F}_y &\rightarrow -\frac{1}{4} \frac{k_{3y}}{\|\mathbf{k}_3\|} \left(\Omega_{23} e^{i(\mathbf{k}_{32} \cdot \mathbf{x} - \omega_{32} t)} - \Omega_{23}^* e^{-i(\mathbf{k}_{32} \cdot \mathbf{x} - \omega_{32} t)} \right) \left(e^{i\omega_{RF} t} \hat{F}_+ - e^{-i\omega_{RF} t} \hat{F}_- \right) \\
&\approx \mp \frac{1}{2} \frac{k_{3y}}{\|\mathbf{k}_3\|} |\Omega_{23}| \left(\cos[\mathbf{k}_{32} \cdot \mathbf{x} - (\omega_{32} \mp \omega_{RF}) t + \phi_{23}] \hat{F}_x - \sin[\mathbf{k}_{32} \cdot \mathbf{x} - (\omega_{32} \mp \omega_{RF}) t + \phi_{23}] \hat{F}_y \right)
\end{aligned} \tag{C.15}$$

The complete Hamiltonian in the rotating frame after doing the rotating wave ap-

proximation is then

$$\begin{aligned}
\hat{H} = & \frac{1}{2} \frac{|\Omega_{12}|}{\|\mathbf{k}_1\|} \left(\left(k_{1x} \sin[\mathbf{k}_{21} \cdot \mathbf{x} - (\omega_{21} \mp \omega_{RF})t + \phi_{12}] \pm k_{1y} \cos[\mathbf{k}_{21} \cdot \mathbf{x} - (\omega_{21} \pm \omega_{RF})t + \phi_{12}] \right) \hat{F}_x \right. \\
& + \left. \left(\pm k_{1x} \cos[\mathbf{k}_{21} \cdot \mathbf{x} - (\omega_{21} \mp \omega_{RF})t + \phi_{12}] \mp k_{1y} \sin[\mathbf{k}_{21} \cdot \mathbf{x} - (\omega_{21} \pm \omega_{RF})t + \phi_{12}] \right) \hat{F}_y \right) \\
& \frac{1}{2} \frac{|\Omega_{23}|}{\|\mathbf{k}_3\|} \left(\left(k_{3x} \sin[\mathbf{k}_{32} \cdot \mathbf{x} - (\omega_{32} \mp \omega_{RF})t + \phi_{23}] \pm k_{3y} \cos[\mathbf{k}_{32} \cdot \mathbf{x} - (\omega_{32} \pm \omega_{RF})t + \phi_{23}] \right) \hat{F}_x \right. \\
& + \left. \left(\pm k_{3x} \cos[\mathbf{k}_{32} \cdot \mathbf{x} - (\omega_{32} \mp \omega_{RF})t + \phi_{23}] \mp k_{3y} \sin[\mathbf{k}_{32} \cdot \mathbf{x} - (\omega_{32} \pm \omega_{RF})t + \phi_{23}] \right) \hat{F}_y \right) \\
& + |\Omega_{13}| \sin(\mathbf{k}_{31} \cdot \mathbf{x} - \omega_{31}t + \phi_{13}) \hat{F}_z
\end{aligned} \tag{C.16}$$

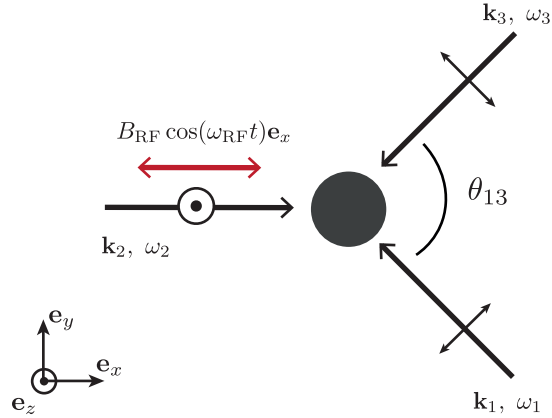


Figure 1: Laser layout: We use a strong RF field and three linearly polarized Raman beams propagating in the xy plane couple the $|xyz\rangle$ states and engineer the Rashba Hamiltonian.

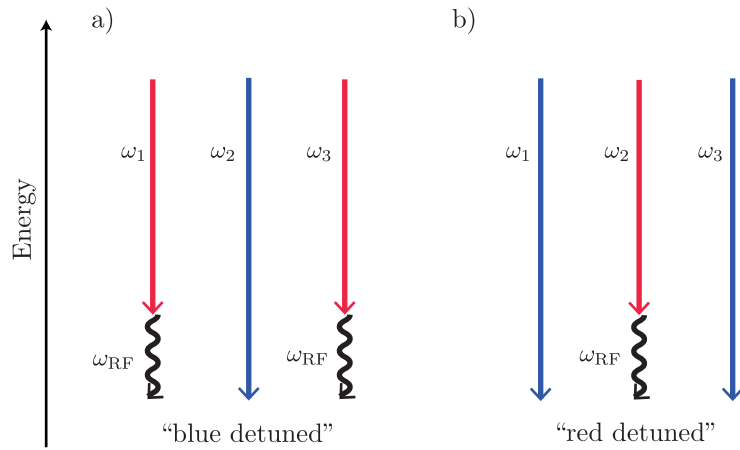


Figure 2: Laser frequencies: We have two frequency choices that allow us to address the three transitions between the $|xyz\rangle$ states. **a)** The blue detuned case. There are 2 frequencies smaller by about ω_{RF} and one larger frequency. **b)** The red detuned case. There are 2 frequencies that are larger by about ω_{RF} and one smaller frequency. Nice!

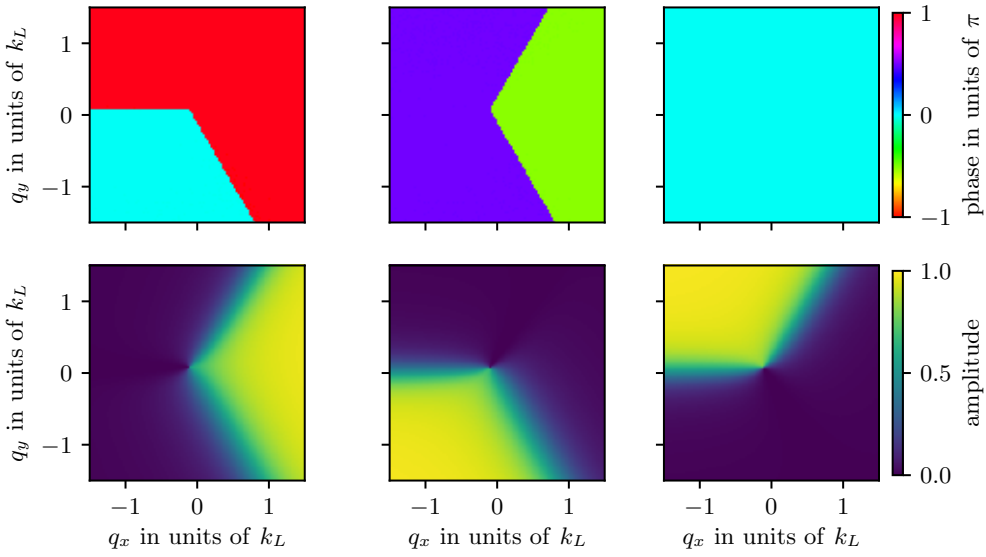


Figure 3: **a** Probabilities as a function of quasimomentum for the three output ports of the interferometer at $t_{\text{free}} = 160 \mu\text{s}$ **b** Probabilities as a function of free evolution time t_{free} for an input state with quasimomentum $(q_1, q_2) = (0.55, -0.92) k_L$ indicated by the blue star on **a** and in the topological ground branch ($n = 1$)

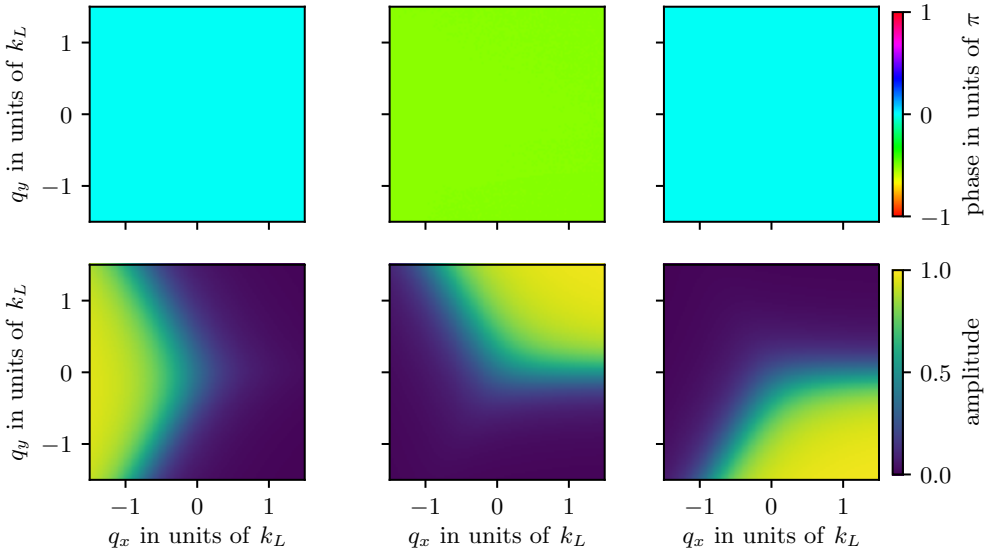


Figure 4: **a** Probabilities as a function of quasimomentum for the three output ports of the interferometer at $t_{\text{free}} = 160 \mu\text{s}$ **b** Probabilities as a function of free evolution time t_{free} for an input state with quasimomentum $(q_1, q_2) = (0.55, -0.92) k_L$ indicated by the blue star on **a** and in the topological ground branch ($n = 1$)

Bibliography

- [1] Ketterle W., Durfee D.S., and Stamper-Kurn D.M. Making, probing and understanding Bose-Einstein condensates. *Proceedings of the International School of Physics "Enrico Fermi"*, 140(Bose-Einstein Condensation in Atomic Gases):67–176, 1999.
- [2] Franco Dalfovo, Stefano Giorgini, Lev P. Pitaevskii, and Sandro Stringari. Theory of Bose-Einstein condensation in trapped gases. *Reviews of Modern Physics*, 71(3):463–512, April 1999.
- [3] C.J. Pethick and H. Smith. *Bose-Einstein Condensation of Dilute Gases*. Oxford University Press, Oxford, UK, 2005.
- [4] *Bose-Einstein Condensation*. International Series of Monographs on Physics. Oxford University Press, Oxford, New York, June 2003.
- [5] Y. Castin and R. Dum. Bose-Einstein Condensates in Time Dependent Traps. *Physical Review Letters*, 77(27):5315–5319, December 1996.
- [6] G. F. Gribakin and V. V. Flambaum. Calculation of the scattering length in atomic collisions using the semiclassical approximation. *Physical Review A*, 48(1):546–553, July 1993.
- [7] Dan M. Stamper-Kurn and Masahito Ueda. Spinor Bose gases: Symmetries, magnetism, and quantum dynamics. *Reviews of Modern Physics*, 85(3):1191–1244, July 2013.
- [8] S. De, D. L. Campbell, R. M. Price, A. Putra, Brandon M. Anderson, and I. B. Spielman. Quenched binary Bose-Einstein condensates: Spin-domain formation and coarsening. *Physical Review A*, 89(3):033631, March 2014.

- [9] Daniel Adam Steck. Rubidium 87 D line data. Available online, <http://steck.us/alkalidata>, April 2018. revision 2.1.5.
- [10] Charles Schwartz. Theory of Hyperfine Structure. *Physical Review*, 97(2):380–395, January 1955.
- [11] P. Zeeman. The effect of magnetisation on the nature of light emitted by a substance. *Nature*, 55(1424):347–347, 1897.
- [12] G. Breit and I. I. Rabi. Measurement of Nuclear Spin. *Physical Review*, 38(11):2082–2083, December 1931.
- [13] Harold J. Metcalf and Peter van der Straten. Deceleration of an Atomic Beam. In Harold J. Metcalf and Peter van der Straten, editors, *Laser Cooling and Trapping*, Graduate Texts in Contemporary Physics, pages 73–86. Springer New York, New York, NY, 1999.
- [14] William D. Phillips. Nobel Lecture: Laser cooling and trapping of neutral atoms. *Reviews of Modern Physics*, 70(3):721–741, July 1998.
- [15] Daniel L. Campbell. *Engineered potentials in ultracold Bose-Einstein condensates*. PhD thesis, University of Maryland College Park, Digital Repository at the University of Maryland, 6 2015.
- [16] Ryan Price. *Phase transitions in engineered ultracold quantum systems*. PhD thesis, University of Maryland College Park, Digital Repository at the University of Maryland, 6 2016.
- [17] J. Stark. Beobachtungen über den Effekt des elektrischen Feldes auf Spektrallinien. I. Quereffekt. *Annalen der Physik*, 348(7):965–982, 1914.
- [18] Jacques Dupont-Roc Claude Cohen-Tannoudji and Gilbert Grynberg. *Atom-Photon Interactions*. Wiley-VCH, Weinheim, 2006.
- [19] Daniel Adam Steck. Quantum and atom optics. Available online at <http://steck.us/teaching>, January 2015. revision 0.12.2.
- [20] Ivan H. Deutsch and Poul S. Jessen. Quantum control and measurement of atomic spins in polarization spectroscopy. *Optics Communications*, 283(5):681–694, March 2010.
- [21] J. J. Sakurai. *Modern Quantum Mechanics*. Addison Wesley Publishing Company, Menlo Park, California, 1994.
- [22] Rudolf Grimm, Matthias Weidemüller, and Yurii B. Ovchinnikov. Optical Dipole Traps for Neutral Atoms. In Benjamin Bederson and Herbert Walther, editors, *Advances In Atomic, Molecular, and Optical Physics*, volume 42, pages 95–170. Academic Press, January 2000.

- [23] N. Goldman, G. Juzeliūnas, P. Öhberg, and I. B. Spielman. Light-induced gauge fields for ultracold atoms. *Reports on Progress in Physics*, 77(12):126401, November 2014.
- [24] Rui Han, Hui Khoon Ng, and Berthold-Georg Englert. Raman transitions without adiabatic elimination: a simple and accurate treatment. *Journal of Modern Optics*, 60(4):255–265, February 2013.
- [25] Bindya Arora, M. S. Safranova, and Charles W. Clark. Tune-out wavelengths of alkali-metal atoms and their applications. *Physical Review A*, 84(4):043401, October 2011.
- [26] Y.-J. Lin, K. Jiménez-García, and I. B. Spielman. Spin-orbit-coupled Bose-Einstein condensates. *Nature*, 471(7336):83–86, March 2011.
- [27] Yu A. Bychkov and E. I. Rashba. Oscillatory effects and the magnetic susceptibility of carriers in inversion layers. *Journal of Physics C: Solid State Physics*, 17(33):6039, 1984.
- [28] G. Dresselhaus. Spin-Orbit Coupling Effects in Zinc Blende Structures. *Physical Review*, 100(2):580–586, October 1955.
- [29] Victor Galitski and Ian B. Spielman. Spin-orbit coupling in quantum gases. *Nature*, 494(7435):49–54, February 2013.
- [30] I. I. Rabi. Space Quantization in a Gyrating Magnetic Field. *Physical Review*, 51(8):652–654, April 1937.
- [31] Norman F. Ramsey. A Molecular Beam Resonance Method with Separated Oscillating Fields. *Physical Review*, 78(6):695–699, June 1950.
- [32] D. L. Campbell, R. M. Price, A. Putra, A. Valdes-Curiel, D. Trypogeorgos, and I. B. Spielman. Magnetic phases of spin-1 spin-orbit-coupled Bose gases. *Nature Communications*, 7:10897, March 2016.
- [33] Christopher J. Foot. *Atomic Physics*. Oxford University Press, Cambridge, UK, 2006.
- [34] G. Reinaudi, T. Lahaye, Z. Wang, and D. Guéry-Odelin. Strong saturation absorption imaging of dense clouds of ultracold atoms. *Optics Letters*, 32(21):3143–3145, November 2007.
- [35] D. Genkina, L. M. Aycock, B. K. Stuhl, H.-I. Lu, R. A. Williams, and I. B. Spielman. Feshbach enhanceds-wave scattering of fermions: direct observation with optimized absorption imaging. *New Journal of Physics*, 18(1):013001, December 2015.
- [36] C. Silber, S. Günther, C. Marzok, B. Deh, Ph. W. Courteille, and C. Zimmermann. Quantum-Degenerate Mixture of Fermionic Lithium and Bosonic Rubidium Gases. *Physical Review Letters*, 95(17):170408, October 2005.

- [37] B. Deh, C. Marzok, C. Zimmermann, and Ph. W. Courteille. Feshbach resonances in mixtures of ultracold ^6Li and ^{87}Rb gases. *Physical Review A*, 77(1):010701, January 2008.
- [38] William D. Phillips and Harold Metcalf. Laser Deceleration of an Atomic Beam. *Physical Review Letters*, 48(9):596–599, March 1982.
- [39] Paul D. Lett, Richard N. Watts, Christoph I. Westbrook, William D. Phillips, Phillip L. Gould, and Harold J. Metcalf. Observation of Atoms Laser Cooled below the Doppler Limit. *Physical Review Letters*, 61(2):169–172, July 1988.
- [40] Clarence Zener and Ralph Howard Fowler. Non-adiabatic crossing of energy levels. *Proceedings of the Royal Society of London. Series A, Containing Papers of a Mathematical and Physical Character*, 137(833):696–702, September 1932.
- [41] Erin Marshall Seroka, Ana Valdés Curiel, Dimitrios Trypogeorgos, Nathan Lundblad, and Ian B. Spielman. Repeated Measurements with Minimally Destructive Partial-Transfer Absorption Imaging. *arXiv:1907.05372 [physics]*, July 2019. arXiv: 1907.05372.
- [42] Christoph Becker. *Multi component Bose-Einstein condensates From mean field physics to strong correlations*. PhD thesis, Universität Hamburg, <http://citeseerx.ist.psu.edu>, 6 2008.
- [43] P. T. Starkey, C. J. Billington, S. P. Johnstone, M. Jasperse, K. Helmerson, L. D. Turner, and R. P. Anderson. A scripted control system for autonomous hardware-timed experiments. *Review of Scientific Instruments*, 84(8):085111, August 2013.
- [44] K. Jiménez-García, L. J. LeBlanc, R. A. Williams, M. C. Beeler, C. Qu, M. Gong, C. Zhang, and I. B. Spielman. Tunable spin-orbit coupling via strong driving in ultracold-atom systems. *Phys. Rev. Lett.*, 114:125301, Mar 2015.
- [45] Doppler-Limited Absorption and Fluorescence Spectroscopy with Lasers. In Wolfgang Demtröder, editor, *Laser Spectroscopy: Vol. 2 Experimental Techniques*, pages 1–75. Springer Berlin Heidelberg, Berlin, Heidelberg, 2008.
- [46] Lawrence W. Cheuk, Ariel T. Sommer, Zoran Hadzibabic, Tarik Yefsah, Waseem S. Bakr, and Martin W. Zwierlein. Spin-Injection Spectroscopy of a Spin-Orbit Coupled Fermi Gas. *Physical Review Letters*, 109(9):095302, 2012.
- [47] David M. Jonas. Two-Dimensional Femtosecond Spectroscopy. *Annual Review of Physical Chemistry*, 54(1):425–463, 2003.

- [48] Bryce Yoshimura, W. C. Campbell, and J. K. Freericks. Diabatic-ramping spectroscopy of many-body excited states. *Physical Review A*, 90(6):062334, 2014.
- [49] Limei Wang, Hao Zhang, Linjie Zhang, Georg Raithel, Jianming Zhao, and Suotang Jia. Atom-interferometric measurement of Stark level splittings. *Physical Review A*, 92(3):033619, September 2015.
- [50] R. P. Anderson, D. Trypogeorgos, A. Valdés-Curiel, Q.-Y. Liang, J. Tao, M. Zhao, T. Andrijauskas, G. Juzeliūnas, and I. B. Spielman. Realization of a fractional period adiabatic superlattice. *arXiv:1907.08910 [cond-mat, physics:physics, physics:quant-ph]*, July 2019. arXiv: 1907.08910.
- [51] A. Valdés-Curiel, D. Trypogeorgos, E. E. Marshall, and I. B. Spielman. Fourier transform spectroscopy of a spin-orbit coupled Bose gas. *New Journal of Physics*, 19(3):033025, 2017.
- [52] Anders Sørensen and Klaus Mølmer. Entanglement and quantum computation with ions in thermal motion. *Physical Review A*, 62(2):022311, July 2000.
- [53] G. Floquet. Sur les équations différentielles linéaires à coefficients périodiques. *Annales scientifiques de l'École Normale Supérieure*, 12:47–88, 1883.
- [54] Y.-J. Lin, R. L. Compton, K. Jiménez-García, W. D. Phillips, J. V. Porto, and I. B. Spielman. A synthetic electric force acting on neutral atoms. *Nature Physics*, 7(7):531–534, July 2011.
- [55] Chunqing Deng, Jean-Luc Orgiazzi, Feiruo Shen, Sahel Ashhab, and Adrian Lupascu. Observation of Floquet States in a Strongly Driven Artificial Atom. *Physical Review Letters*, 115(13):133601, September 2015.
- [56] J. Eisert, M. Friesdorf, and C. Gogolin. Quantum many-body systems out of equilibrium. *Nature Physics*, 11(2):124–130, February 2015.
- [57] D. L. Campbell and I. B. Spielman. Rashba realization: Raman with RF. *New J. Phys.*, 18(3):033035, 2016.
- [58] Douglas R. Hofstadter. Energy levels and wave functions of Bloch electrons in rational and irrational magnetic fields. *Physical Review B*, 14(6):2239–2249, September 1976.
- [59] D. Trypogeorgos, A. Valdés-Curiel, I. B. Spielman, and C. Emery. Perpetual emulation threshold of PT^\perp -symmetric Hamiltonians. *Journal of Physics A: Mathematical and Theoretical*, 51(32):325302, June 2018.

- [60] D. Trypogeorgos, A. Valdés-Curiel, N. Lundblad, and I. B. Spielman. Synthetic clock transitions via continuous dynamical decoupling. *Physical Review A*, 97(1):013407, January 2018.
- [61] R. P. Anderson, M. J. Kewming, and L. D. Turner. Continuously observing a dynamically decoupled spin-1 quantum gas. *Physical Review A*, 97(1):013408, January 2018.
- [62] E. L. Hahn. Spin Echoes. *Physical Review*, 80(4):580–594, November 1950.
- [63] Lorenza Viola and Seth Lloyd. Dynamical suppression of decoherence in two-state quantum systems. *Phys. Rev. A*, 58(4):2733–2744, October 1998.
- [64] I. Cohen, N. Aharon, and A. Retzker. Continuous dynamical decoupling utilizing time-dependent detuning. *Fortschr. Phys.*, 65(6-8):n/a–n/a, June 2017.
- [65] F. F. Fanchini, J. E. M. Hornos, and R. d J. Napolitano. Continuously decoupling single-qubit operations from a perturbing thermal bath of scalar bosons. *Physical Review A*, 75(2), February 2007. arXiv: quant-ph/0611188.
- [66] N. Aharon, I. Cohen, F. Jelezko, and A. Retzker. Fully robust qubit in atomic and molecular three-level systems. *New J. Phys.*, 18(12):123012, 2016.
- [67] Michael J. Biercuk, Hermann Uys, Aaron P. VanDevender, Nobuyasu Shiga, Wayne M. Itano, and John J. Bollinger. Optimized dynamical decoupling in a model quantum memory. *Nature*, 458(7241):996–1000, April 2009.
- [68] J.-M. Cai, B. Naydenov, R. Pfeiffer, L. P. McGuinness, K. D. Jahnke, F. Jelezko, M. B. Plenio, and A. Retzker. Robust dynamical decoupling with concatenated continuous driving. *New Journal of Physics*, 14(11):113023, November 2012. arXiv: 1111.0930.
- [69] A. Bermudez, P. O. Schmidt, M. B. Plenio, and A. Retzker. Robust trapped-ion quantum logic gates by continuous dynamical decoupling. *Phys. Rev. A*, 85(4):040302, April 2012.
- [70] I. Baumgart, J.-M. Cai, A. Retzker, M. B. Plenio, and Ch. Wunderlich. Ultrasensitive magnetometer using a single atom. *Phys. Rev. Lett.*, 116:240801, Jun 2016.
- [71] G. A. Kazakov and T. Schumm. Magic radio-frequency dressing for trapped atomic microwave clocks. *Phys. Rev. A*, 91(2):023404, February 2015.
- [72] L. Sárkány, P. Weiss, H. Hattermann, and J. Fortágh. Controlling the magnetic-field sensitivity of atomic-clock states by microwave dressing. *Phys. Rev. A*, 90(5):053416, November 2014.

- [73] Arne Laucht, Rachpon Kalra, Stephanie Simmons, Juan P. Dehollain, Juha T. Muhonen, Fahd A. Mohiyaddin, Solomon Freer, Fay E. Hudson, Kohei M. Itoh, David N. Jamieson, Jeffrey C. McCallum, Andrew S. Dzurak, and A. Morello. A dressed spin qubit in silicon. *Nat Nano*, 12(1):61–66, January 2017.
- [74] D. Farfurnik, N. Aharon, I. Cohen, Y. Hovav, A. Retzker, and N. Bar-Gill. Experimental realization of time-dependent phase-modulated continuous dynamical decoupling. *arXiv:1704.07582 [quant-ph]*, April 2017. arXiv: 1704.07582.
- [75] Atsushi Noguchi, Shinsuke Haze, Kenji Toyoda, and Shinji Urabe. Generation of a Decoherence-Free Entangled State Using a Radio-Frequency Dressed State. *Phys. Rev. Lett.*, 108(6):060503, February 2012.
- [76] D. Andrew Golter, Thomas K. Baldwin, and Hailin Wang. Protecting a Solid-State Spin from Decoherence Using Dressed Spin States. *Phys. Rev. Lett.*, 113(23):237601, December 2014.
- [77] N. Timoney, I. Baumgart, M. Johanning, A. F. Varón, M. B. Plenio, A. Retzker, and Ch Wunderlich. Quantum gates and memory using microwave-dressed states. *Nature*, 476(7359):185–188, August 2011.
- [78] S. C. Webster, S. Weidt, K. Lake, J. J. McLoughlin, and W. K. Hensinger. Simple Manipulation of a Microwave Dressed-State Ion Qubit. *Phys. Rev. Lett.*, 111(14):140501, October 2013.
- [79] A. Barfuss, J. Teissier, E. Neu, A. Nunnenkamp, and P. Maletinsky. Strong mechanical driving of a single electron spin. *Nat Phys*, 11(10):820–824, October 2015.
- [80] S. Rohr, E. Dupont-Ferrier, B. Pigeau, P. Verlot, V. Jacques, and O. Arcizet. Synchronizing the Dynamics of a Single Nitrogen Vacancy Spin Qubit on a Parametrically Coupled Radio-Frequency Field through Microwave Dressing. *Phys. Rev. Lett.*, 112(1):010502, January 2014.
- [81] Nigel R. Cooper and Jean Dalibard. Reaching Fractional Quantum Hall States with Optical Flux Lattices. *Physical Review Letters*, 110(18):185301, April 2013.
- [82] Gediminas Juzeliūnas, Julius Ruseckas, and Jean Dalibard. Generalized Rashba-Dresselhaus spin-orbit coupling for cold atoms. *Phys. Rev. A*, 81(5):053403, May 2010.
- [83] D. Bacon, J. Kempe, D. A. Lidar, and K. B. Whaley. Universal Fault-Tolerant Quantum Computation on Decoherence-Free Subspaces. *Phys. Rev. Lett.*, 85(8):1758–1761, August 2000.
- [84] Pablo Solano, Jeffrey A. Grover, Jonathan E. Hoffman, Sylvain Ravets, Fredrik K. Fatemi, Luis A. Orozco, and Steven L. Rolston. Chapter Seven

- Optical Nanofibers: A New Platform for Quantum Optics. In Chun C. Lin and Susanne F. Yelin Ennio Arimondo, editor, *Advances In Atomic, Molecular, and Optical Physics*, volume 66, pages 439–505. Academic Press, 2017. DOI: 10.1016/bs.aamop.2017.02.003.
- [85] Ze-Liang Xiang, Sahel Ashhab, J. Q. You, and Franco Nori. Hybrid quantum circuits: Superconducting circuits interacting with other quantum systems. *Rev. Mod. Phys.*, 85(2):623–653, April 2013.
 - [86] M. Z. Hasan and C. L. Kane. Colloquium: Topological insulators. *Reviews of Modern Physics*, 82(4):3045–3067, November 2010.
 - [87] Tomoki Ozawa, Hannah M. Price, Alberto Amo, Nathan Goldman, Mohammad Hafezi, Ling Lu, Mikael C. Rechtsman, David Schuster, Jonathan Simon, Oded Zilberberg, and Iacopo Carusotto. Topological photonics. *Reviews of Modern Physics*, 91(1):015006, March 2019.
 - [88] Pierre Delplace, J. B. Marston, and Antoine Venaille. Topological origin of equatorial waves. *Science*, 358(6366):1075–1077, November 2017.
 - [89] V. Peano, C. Brendel, M. Schmidt, and F. Marquardt. Topological Phases of Sound and Light. *Physical Review X*, 5(3):031011, July 2015.
 - [90] Zhaoju Yang, Fei Gao, Xihang Shi, Xiao Lin, Zhen Gao, Yidong Chong, and Baile Zhang. Topological Acoustics. *Physical Review Letters*, 114(11):114301, March 2015.
 - [91] N. R. Cooper, J. Dalibard, and I. B. Spielman. Topological bands for ultracold atoms. *Rev. Mod. Phys.*, 91:015005, Mar 2019.
 - [92] D. J. Thouless, M. Kohmoto, M. P. Nightingale, and M. den Nijs. Quantized Hall Conductance in a Two-Dimensional Periodic Potential. *Physical Review Letters*, 49(6):405–408, August 1982.
 - [93] F. D. M. Haldane. Model for a Quantum Hall Effect without Landau Levels: Condensed-Matter Realization of the "Parity Anomaly". *Physical Review Letters*, 61(18):2015–2018, October 1988.
 - [94] C. L. Kane and E. J. Mele. $\{Z\}_2$ Topological Order and the Quantum Spin Hall Effect. *Physical Review Letters*, 95(14):146802, September 2005.
 - [95] D. B. Newell, F. Cabiati, J. Fischer, K. Fujii, S. G. Karshenboim, H. S. Margolis, E. de Mirandés, P. J. Mohr, F. Nez, K. Pachucki, T. J. Quinn, B. N. Taylor, M. Wang, B. M. Wood, and Z. Zhang. The CODATA 2017 values of h, e, k, and N A for the revision of the SI. *Metrologia*, 55(1):L13–L16, January 2018.

- [96] Chetan Nayak, Steven H. Simon, Ady Stern, Michael Freedman, and Sankar Das Sarma. Non-Abelian anyons and topological quantum computation. *Reviews of Modern Physics*, 80(3):1083–1159, September 2008.
- [97] Eduardo Nahmud-Achar. *Differential Topology and Geometry with Applications to Physics*. 2053–2563. IOP Publishing, 2018.
- [98] L. Landau. The Theory of Phase Transitions. *Nature*, 138(3498):840–841, November 1936.
- [99] K. v. Klitzing, G. Dorda, and M. Pepper. New Method for High-Accuracy Determination of the Fine-Structure Constant Based on Quantized Hall Resistance. *Physical Review Letters*, 45(6):494–497, August 1980.
- [100] David Tong. Lectures on the Quantum Hall Effect. *arXiv:1606.06687 [cond-mat, physics:hep-th]*, June 2016. arXiv: 1606.06687.
- [101] Barry Simon. Holonomy, the Quantum Adiabatic Theorem, and Berry’s Phase. *Physical Review Letters*, 51(24):2167–2170, December 1983.
- [102] Mikio Nakahara. CRC Press, New York, NY, 2003.
- [103] Berry Michael Victor. Quantal phase factors accompanying adiabatic changes. *Proceedings of the Royal Society of London. A. Mathematical and Physical Sciences*, 392(1802):45–57, March 1984.
- [104] Y. Aharonov and D. Bohm. Significance of Electromagnetic Potentials in the Quantum Theory. *Physical Review*, 115(3):485–491, August 1959.
- [105] Dirac Paul Adrien Maurice. Quantised singularities in the electromagnetic field., *Proceedings of the Royal Society of London. Series A, Containing Papers of a Mathematical and Physical Character*, 133(821):60–72, September 1931.
- [106] Ralph M. Kaufmann, Dan Li, and Birgit Wehefritz-Kaufmann. Notes on topological insulators. *Reviews in Mathematical Physics*, 28(10):1630003, November 2016. arXiv: 1501.02874.
- [107] Hirokazu Miyake, Georgios A. Siviloglou, Colin J. Kennedy, William Cody Burton, and Wolfgang Ketterle. Realizing the Harper Hamiltonian with Laser-Assisted Tunneling in Optical Lattices. *Physical Review Letters*, 111(18):185302, October 2013.
- [108] M. Aidelsburger, M. Atala, M. Lohse, J. T. Barreiro, B. Paredes, and I. Bloch. Realization of the Hofstadter Hamiltonian with Ultracold Atoms in Optical Lattices. *Physical Review Letters*, 111(18):185301, October 2013.
- [109] Gregor Jotzu, Michael Messer, Rémi Desbuquois, Martin Lebrat, Thomas Uehlinger, Daniel Greif, and Tilman Esslinger. Experimental realization of the topological Haldane model with ultracold fermions. *Nature*, 515(7526):237–240, November 2014.

- [110] H.-I Lu, M. Schemmer, L. M. Aycock, D. Genkina, S. Sugawa, and I. B. Spielman. Geometrical pumping with a bose-einstein condensate. *Phys. Rev. Lett.*, 116:200402, May 2016.
- [111] M. Lohse, C. Schweizer, O. Zilberberg, M. Aidelsburger, and I. Bloch. A Thouless quantum pump with ultracold bosonic atoms in an optical superlattice. *Nature Physics*, 12(4):350–354, April 2016.
- [112] Zhan Wu, Long Zhang, Wei Sun, Xiao-Tian Xu, Bao-Zong Wang, Si-Cong Ji, Youjin Deng, Shuai Chen, Xiong-Jun Liu, and Jian-Wei Pan. Realization of two-dimensional spin-orbit coupling for Bose-Einstein condensates. *Science*, 354(6308):83–88, October 2016.
- [113] Wei Sun, Bao-Zong Wang, Xiao-Tian Xu, Chang-Rui Yi, Long Zhang, Zhan Wu, Youjin Deng, Xiong-Jun Liu, Shuai Chen, and Jian-Wei Pan. Highly Controllable and Robust 2d Spin-Orbit Coupling for Quantum Gases. *Physical Review Letters*, 121(15):150401, October 2018.
- [114] Frank Wilczek and A. Zee. Appearance of Gauge Structure in Simple Dynamical Systems. *Physical Review Letters*, 52(24):2111–2114, June 1984.
- [115] Tudor D. Stanescu, Brandon Anderson, and Victor Galitski. Spin-orbit coupled Bose-Einstein condensates. *Physical Review A*, 78(2):023616, August 2008.
- [116] Tigran A. Sedrakyan, Alex Kamenev, and Leonid I. Glazman. Composite fermion state of spin-orbit-coupled bosons. *Physical Review A*, 86(6):063639, December 2012.
- [117] Hui Hu, Lei Jiang, Xia-Ji Liu, and Han Pu. Probing Anisotropic Superfluidity in Atomic Fermi Gases with Rashba Spin-Orbit Coupling. *Physical Review Letters*, 107(19):195304, November 2011.
- [118] D. L. Campbell, G. Juzeliūnas, and I. B. Spielman. Realistic Rashba and Dresselhaus spin-orbit coupling for neutral atoms. *Physical Review A*, 84(2):025602, August 2011.
- [119] Tudor D. Stanescu and Victor Galitski. Spin relaxation in a generic two-dimensional spin-orbit coupled system. *Physical Review B*, 75(12):125307, March 2007.
- [120] Y.-J. Lin, A. R. Perry, R. L. Compton, I. B. Spielman, and J. V. Porto. Rapid production of $\text{\^87}\text{R}\text{b}$ Bose-Einstein condensates in a combined magnetic and optical potential. *Physical Review A*, 79(6):063631, June 2009.
- [121] Lianghui Huang, Zengming Meng, Pengjun Wang, Peng Peng, Shao-Liang Zhang, Liangchao Chen, Donghao Li, Qi Zhou, and Jing Zhang. Experimental

- realization of two-dimensional synthetic spin-orbit coupling in ultracold Fermi gases. *Nature Physics*, 12(6):540–544, June 2016.
- [122] Zengming Meng, Lianghui Huang, Peng Peng, Donghao Li, Liangchao Chen, Yong Xu, Chuanwei Zhang, Pengjun Wang, and Jing Zhang. Experimental Observation of a Topological Band Gap Opening in Ultracold Fermi Gases with Two-Dimensional Spin-Orbit Coupling. *Physical Review Letters*, 117(23):235304, December 2016.
 - [123] Satoshi Tojo, Taro Hayashi, Tatsuyoshi Tanabe, Takuya Hirano, Yuki Kawaguchi, Hiroki Saito, and Masahito Ueda. Spin-dependent inelastic collisions in spin-2 Bose-Einstein condensates. *Physical Review A*, 80(4):042704, October 2009.
 - [124] N. Goldman and J. Dalibard. Periodically Driven Quantum Systems: Effective Hamiltonians and Engineered Gauge Fields. *Physical Review X*, 4(3):031027, 2014.
 - [125] N. Fläschner, B. S. Rem, M. Tarnowski, D. Vogel, D.-S. Lühmann, K. Sengstock, and C. Weitenberg. Experimental reconstruction of the Berry curvature in a Floquet Bloch band. *Science*, 352(6289):1091–1094, May 2016.
 - [126] Clément Godfrin, Rafik Ballou, Edgar Bonet, Mario Ruben, Svetlana Klyatskaya, Wolfgang Wernsdorfer, and Franck Balestro. Generalized Ramsey interferometry explored with a single nuclear spin qudit. *npj Quantum Information*, 4(1):53, October 2018.
 - [127] Takahiro Fukui, Yasuhiro Hatsugai, and Hiroshi Suzuki. Chern Numbers in Discretized Brillouin Zone: Efficient Method of Computing (Spin) Hall Conductances. *Journal of the Physical Society of Japan*, 74(6):1674–1677, June 2005.
 - [128] L. Duca, T. Li, M. Reitter, I. Bloch, M. Schleier-Smith, and U. Schneider. An Aharonov-Bohm interferometer for determining Bloch band topology. *Science*, 347(6219):288–292, January 2015.
 - [129] H. B. Nielsen and Masao Ninomiya. The Adler-Bell-Jackiw anomaly and Weyl fermions in a crystal. *Physics Letters B*, 130(6):389–396, November 1983.
 - [130] Mário G. Silveirinha. Chern invariants for continuous media. *Physical Review B*, 92(12):125153, September 2015.
 - [131] Tigran A. Sedrakyan, Victor M. Galitski, and Alex Kamenev. Statistical Transmutation in Floquet Driven Optical Lattices. *Physical Review Letters*, 115(19):195301, November 2015.